STUDY OF SPEED AND FORCE IN BIOMANIPULATION

ZHOU SHENGFENG

A THESIS SUBMITTED

FOR THE DEGREE OF DOCTOR OF
PHILOSOPHY

DEPARTMENT OF MECHANICAL
ENGINEERING

NATIONAL UNIVERSITY OF SINGAPORE

2013

DECLARATION

I hereby declare that this thesis is my original work and it has been written by me in its entirety.
I have duly acknowledged all the sources of information which have been used in this thesis.

This thesis has also not been submitted for any degree in any university previously.

ZHOU Shengfeng

10 August 2013

Acknowledgments

I would like to express my heartfelt gratitude to Assoc. Prof. Peter, C.Y. Chen and Assoc. Prof. Chong-Jin Ong, from Department of Mechanical Engineering, National University of Singapore, for their invaluable guidance, enthusiasm and patience throughout my PhD study. This thesis would not be possible without their knowledge and support.

I would like to express my appreciation to Dr. Nam Joo Hoo for generously sharing his experience and knowledge. I have learned a lot from him pertaining the microinjection experiments. Special thanks also go to Dr. Masood Dehghan, for his insightful discussions and suggestions regarding the switching systems.

I wish to thank all my fellow colleagues, especially group members, Dr. Guofeng Guan, Mr. Sahan Christie Bandara Herath, Ms. Yue Du, Ms. See Hian Hian and Dr. Jie Wan for their friendship and all the enjoyable moments together. I would also like to thank all the staffs from Control and Mechatronics lab for their kindness and assistance. In particular, Mrs. Ooi-Toh Chew Hoey and Mdm. Hamidah Bte Jasman provide me plenty of support and help.

I gratefully acknowledge National University of Singapore for providing me the opportunity to study in Singapore and the research scholarship to fulfill the PhD study.

Finally, my deepest gratitude goes to my wife and my parents, for their understanding, emotional support and endless love, through the duration of my studies. I would also like to thank my beloved niece for all the stories she told and all the songs she sang to me. I wish her a wonderful life filled with love and happiness.

Contents

Summary

Enhancing the capability of biomanipulation systems has become a pressing need for advancing the fields of biology and biomedicine. This is particularly motivated by the recent rapid development in the area of mechanobiology, which studies the comprehensive effect of mechanical stimuli on cellular behavior. One important aspect of biomanipulation is the ability to apply mechanical forces accurately on biological organisms. Substantial efforts from a wide range of disciplines have been devoted to developing versatile automated biomanipulation systems. These research efforts have led to various applications of such systems, yet the issue of how to improve the dexterity of fully automated biomanipulation systems equipped with sophisticated force control capability (in order to fully realize the potential of such systems) remains a challenging problem in engineering research. It is in the context of this problem that this thesis explores the specific issues of speed optimization and force control in biomanipulation systems.

The first part of this thesis addresses the design of speed trajectories in a microinjection process, which is a common biomanipulation task, in order to minimize adverse physical effects on the biological organism induced by the injection force. An optimization problem in the design of a speed trajectory for the motion of the micropipette during automated microinjection of zebrafish embryos is formulated. The objective of this optimization problem is to minimize the deformation sustained by the zebrafish embryo. A solution to this optimization problem is proposed by first constructing a viscoelastic model of the zebrafish embryo, and then synthesizing an optimal speed trajectory based on a class of polynomials. Furthermore, results from numerical simulation and experiments that demonstrate the effectiveness of the proposed solution are presented. The statistically meaningful experimental data (generated using a large

sample of zebrafish embryos) provide direct evidence on the advantage of such speed optimization in microinjection.

The second part of this study is devoted to force control of biomanipulation systems. Mechanical force is known to influence the behavior of biological cells. To study how external mechanical forces may affect cellular response and cellular function necessitates the development of sophisticated force-control techniques for accurate application of dynamical forces on biological organisms. A six-strut cellular tensegrity model constructed based on the structural approach is used for the development of advanced force control techniques, since it provides a more comprehensive description of the nonlinearity and dynamic coupling of internal structural elements. The force control task is specified in the context of the six-strut cellular tensegrity model being assigned different properties. To this end, a homogenous tensegrity model with constant mechanical properties is first introduced and a robust force control algorithm is proposed to deal with model uncertainties and partial measurability. A heterogenous tensegrity model with time-varying mechanical properties is subsequently developed and a robust adaptive control algorithm is proposed to handle the time-varying feature. Lastly, based on the tensegrity model, a novel neural-network-based force tracking control for biomanipulation is proposed. The proposed force controller is readily applicable for the control problem concerning manipulator interacting with soft compliant materials. Numerical simulations are conducted to demonstrate the effectiveness of the proposed force control techniques. The work reported in this thesis represents an initial step in analytical investigation of localized force-bearing interactions between a cellular tensegrity model and an external mechanical manipulator.

List of Tables

List of Figures

xi

List of Symbols

Symbols in Chapter 3

$A:$ Maximum acceleration

$b_{2,3}:$ Damping ratio in Maxwell-Weichert Model

$c_{0,...,n}:$ The coefficients of the velocity of nth-order polynomial

$D:$ Maximum deceleration

$F^*:$ The force at τ^*(maximum force)

$f(t):$ Identation force acting on the membrane

$k_{1,2,3}:$ Stiffness in Maxwell-Weichert Model

$t:$ Time

$t':$ The time constant when the micropipette stops indenting motion

$x(t):$ Displacement of micropipette

$V:$ Maximum velocity

$v(t):$ Velocity of micropipette

$\epsilon:$ An infinitesimal positive value

$\tau^*:$ The instant when the embryo is just to be pierced

$\Omega_v:$ The set of all speed trajectories implementable on a given system

Symbols in Chapter 4, 5 and 6

$A(q):$	Equilibrium matrix
$A_f(q_f):$	Modified equilibrium matrix
a_i	The center of the receptive field
b_i	The width of the Gaussian function
$c:$	The constant damping coefficient
$c(t):$	The time-varying damping coefficient
$C(q):$	Damping matrix
$C_f(q_f):$	Modified damping matrix
$C_r:$	The Centripetal-Coiolis effects matrix
$f:$	The contact force
f_d	The desired force
$\dot{f}_d$	The time deravative of the desired force
$f_{ti}:$	The force sustained by the ith tendon
$g_r:$	The conservative forces
$H(q):$	Disturbance matrix
$H_f(q_f):$	Modified disturbance matrix
$H_r:$	The inertial matrix of the manipulator
$k:$	The constant stiffness
$k_i(t):$	The time-varying stiffness of ith tendon
$l_i:$	The length of the tendon
$l_{i0}:$	The length of the initial length of the tendon
$\dot{l}_i:$	The time derivative of l_i

$q_f:$ The modified vector of generalized coordinates

$q_1:$ The Cartesian coorodinates of the contact point G

$q_2:$ The elments of the modified generalized coordiates exluding those in q_1

$S:$ The basis function in raddial basis function neural newok

$T(q):$ Tensions in the working tendons

$T_f(q_f):$ Modified tensions in the working tendons

W^* The ideal weights of raddial basis function neural newok

$u:$ The control input of the manipulator

$\epsilon:$ The corresponind error of neural network estimation

$\lambda_{max}(A):$ The largest eigenvalue of a square matrix A

$\lambda_{min}(A):$ The smallest eigenvalue of a square matrix A

$\|A\|:$ The Frobenius norm of any matrix A

$\|A\|_I:$ The induced norm of any matrix A

$\|B\|:$ The standard Euclidean norm of any vector B

Chapter 1

Introduction

1.1 Background

Biomanipulation refers to the manipulation (e.g.,positioning and grasping) of biological materials/structures (e.g. cells and embryos). It is a common process in biology, biomedicine related practise and areas involving handling of biological materials. Over the last two decades, it has attracted considerable research interests from a wide range of disciplines and various engineering approaches have been developed. The key approaches developed involve mechanical techniques, magnetic and electrical field based methodologies, optics based means and microelectromechanical systems (MEMS) based approaches. Despite these research efforts and advancements, developing novel means to further expand the biomanipulation capability is still an active research area. The direction of recent research focuses on developing sophisticated engineering platforms featuring the integration of force sensing techniques, which enables quantitative investigation of the force the biological material/structure sustains during biomanipulation.

Cell manipulation is one of the most common biomanipulation techniques. It is the crucial step in performing some molecular biology tasks such as DNA microinjection and intracytoplasmic sperm injection (ICSI). The conventional method of single cell manipulation is manual and its success mainly depends on the experience of the operator. Therefore, operator-related factors, such as contamination and poor reproducibility, are inextricable and result in a relatively low success rate. To address these shortcomings, considerable research efforts have been made to automate cell manipulation processes. Most of these efforts concentrate on developing automation systems for the microinjection of zebrafish embryo, due to its wide application in biology study.

These substantial progresses in automating the microinjection process notwithstanding, some factors which play an important role in the injection process have not been fully explored, especially in the aspect of improving the capability of microinjection systems. The speed design in microinjection is such a factor which has not been explicitly studied. Besides microinjection speed, the role of force feedback and force control in microinjection is well recognized in the context of performance improvement. Moreover, the advancement in mechanobiology, the study of how mechanical forces affect cells, further emphasizes the profound role of force and force control in biomanipulation. As a result, novel and efficient tools and means of force sensing at cellular and subcellular levels have been developed for cell mechanobiology study. However, most of research efforts concentrate on developing hardware platforms while less work has been done on exploring sophisticated control algorithms to achieve accurate control of dynamic forces applied on living cells.

The force control problem necessitates the modelling of cell behavior under external force. Approaches based on continuum and structural mechanics have been shown to be useful in constructing mechanical models of living cells. Cellular tensegrity model from the structural approach offers a potentially more

2

effective alternative to those models derived from continuum approach. It is capable of simulating many aspects of cell mechanical behavior and providing biologically plausible explanations for such behaviors. However, its potential for force control application in biomanipulation has not been explored.

The remainder of this chapter provides a brief overview of biomanipulation and microinjection whilst a more detailed review of the automated biomanipulation systems is presented in Chapter 2. An introduction of mechanobiology is then presented with the engineering perspective highlighted. Subsequently, cellular tensegrity model is introduced while a more detailed review will be discussed in Chapter 2. Finally, the objectives and potential contributions of this thesis are presented.

1.2   Biomanipulation and Microinjection

In the field of biology and biomedicine, transportation, orientation and injection of cell and similar micro biological structures are often required. Such manipulations of biological materials/structures are referred to as biomanipulation[12]. The key component of a biomanipulation setup is the micromanipulator which scales down the magnitude of motions from the operator to the end-effector. The movement of the end-effector is usually observed through high-magnification microscopes. The modern biomanipulation systems are equipped with high-resolution actuators (e.g. high-resolution motors and piezoelectric actuators) which are capable of precise control. However, the capabilities of these biomanipulation devices are not fully realized when the tasks are performed manually since competence of the operator is required and highly dependent. Moreover, even for an operator with experience, it is not possible to guarantee the success of the manipulation due to human-related factors, such as fatigue and contamination.

To address the limitations of manual operation in biomanipulation, a number of researchers with multidisciplinary backgrounds are motivated to develop automated biomanipulation systems. Most of these research works focus on automating the microinjection system for zebrafish embryos[5, 13]. The motivation for zebrafish embryo microinjection arises from many factors. First of all, microinjection is a prevalent process in many applications involving *in vitro* fertilization, intracytoplasmic sperm injection, gene therapy and drug development[14]. Since zebrafish embryos is widely used as experimental subjects in biology on account of a number of its characteristics (e.g., transparent, genetically manipulatable, fast development), the injection of zebrafish embryo is one of the most common encountered biomanipulation tasks[15]. Secondly, the developed automated microinjection system for zebrafish embryo is representative of microinjection systems since it consists of all the crucial components, such as micromanipulator, microinjector and positioning stage. Moreover, the control techniques (e.g., vision control and force control) developed in microinjection system are readily applicable for other biomanipulation systems.

1.2.1   Speed in Automated Microinjection System

Microinjection of zebrafish embryo is a common practice in studying the early developmental processes of biological organisms. Conventional manual microinjection usually involves an operator moving the micropipette towards the embryo until its tip slightly touches the chorion, then driving the micropipette to pierce the chorion and maneuvering the tip of the micropipette to a desired location inside the embryo to delivery the DNA material. Such manual operation relies on visual information from optical devices to guide the operator, and is prone to errors (due to various human factors such as fatigue). Approaches

4

reported in the literature for improving the process mainly concentrate on providing haptic feedback to the operator (e.g., [16, 17]) and automating the overall process (e.g., [18, 19]). Considering the requirements of high reproducibility and capability of mass processing (batch biomanipulation), automation of the microinjection process is apparently the more promising approach.

Great advancements have been made in automation of microinjection process. A large portion of them aim at developing devices/systems and control techniques to facilitate the automated process. Some microinjection system towards automatic batch microinjection are developed[6]. These systems consist of a inverted microscope, a micromanipulator, a micropipette and an injector. They are able to precisely deliver genetic material to the desired region or specific target within the zebrafish embryo. However, the microinjection speed and its effects on the embryo is not explicitly studied within the context of further improving the performance of the microinjection system.

The performance of a microinjection process can be evaluated in various context. From a pure biological perspective, the survival rate of the injected embryos is one key performance indicator. From a bio-mechanical perspective, the deformation sustained by the embryo is an important factor to consider, since a large deformation can damage the embryo to the extent of adversely affecting its survivability. Since speed of the micropipette is directly related to the deformation of embryo, the study of injection speed may benefit the microinjection process in terms of minimizing the deformation during the indentation.

The investigation of the microinjection speed is motivated by the fact that embryos exhibit viscoelastic behavior that can be described by analytical models. In particular, when the micropipette indents an embryo at different speeds, the peak contact force and the embryo deformation vary accordingly. Leveraging on viscoelastic models which describe a complex relationship among the applied

force, the speed of indentation, and the deformation of the embryo, it is worthy to study how the microinjection speed affects the reaction force and deformation of zebrafish embryo under indentation during the microinjection process.

1.2.2   Force in Automated Microinjection System

Vision sensing has been the primary modality for early developed automated microinjection systems since it enables precise delivery of genetic material to desired region within the embryo. However, a successful delivery of genetic material does not guarantee a successful microinjection task considering that the damage to embryo induced by injection process may cause the demise of the embryo and thus the failure of the injection task. It has been realized that the force during the penetration procedure is an important factor defining the mechanical injury resulted by injection process. For instance, the embryo after injection has a lower survival rate when the applied force during penetration process exceeds some threshold.

Importance of the role that force plays in microinjection has prompted the integration of force sensing and control into the microinjection system for performance improvement. The objective of these works is to regulate the force during indentation to follow a reasonable desired force trajectory, such as the force trajectory extracted from a proficient technician. The main contribution of these works is the development of various types of force sensing techniques and their integration with the microinjection system. It is noted that the control techniques developed are direct application of conventional robot force control strategies (e.g., PID control and impedance force control). Moreover, these developed force control techniques are based on relatively simple mechanical models constructed from the continuum approach. Although adequate for simple mechanical environment usually encountered in conventional robotic manip-

ulation tasks, these models fall short of capturing the rich dynamics exhibited by living biological cells. For instance, there are only a few works considering the viscoelasticity of the biological materials for force control in microinjection/biomanipulation.

From above discussions, it can be concluded that the existing force control approaches developed for microinjection/biomanipulaiton is preliminary. Suitable modeling of mechanical response of biological materials/structures is vital to realize precise control of applied force on them. Among various mechanical models of living cells, tensegrity model has gained its acceptance in the scientific community since it has been proved to be capable of simulating many aspects of cell mechanical behavior and providing plausible biological explanations for such behavior. A detailed discussion of cellular tensegrity model is presented in section 1.3.

1.3 Needs of Force Control in Cell Mechanobiology

Living cells are constantly subjected to diverse mechanical stimuli from a wide array of sources, including forces generated internally and applied externally. The external mechanical forces exerted on the living cells are known to affect cellular behaviors and functions. Evidences of that mechanical force contributes to the regulation of cell activities, such as gene induction, protein synthesis and a variety of other cellular activities which are essential to cells to maintain appropriate biological functions, are well recognized[1]. An representative example is that abnormal mechanical loading will cause cells dysfunction[20]. The study of how mechanical forces affect cell is referred to as cell mechanobiology. Enormous research devoted to cell mechanobiology notwithstanding, the

Table 1.1: Mechanobiological response of Human tendon fibroblasts. Adapted from [1].

Response	Type of load/force/duration	Significance
Increase in cell proliferation, collagen I gene expression, and Collagen I protein	Uniaxial stretch, 0.5Hz, 4h with 4 and 8%	Stretch magnitude -dependent response
Increase in cell proliferation	Cyclic biaxial stretch, 5%, 1 Hz, 6, 12, and 24 h	Stretch time-depend-ent response
Decrease in cell proliferation	Cyclic biaxial stretch, 5%, 1 Hz, 48h	

mechanism of how cells respond to the external mechanical forces is largely insufficiently studied. Table 1.1 lists some of the mechanobiological response of a type of cell, human tendon fibroblast, to different mechanical loads (e.g., type of force and duration of force). From Table 1.1, it is clearly indicated that different mechanical stimuli result in different cell behavior.

A crucial challenging issue facing cell mechanobiology is the precise control of the mechanical stimuli applied on living cells. This has raised plenty of research interests in engineering community. Various engineering approaches including mechanical, magnetic, optical and microelectromechanical systems (MEMS) techniques, have been developed for quantitative investigation of mechanical loads that the cells are subjected to and the biomechanical responses (e.g., cellular deformation)[14]. Moreover, novel micro-engineered platforms integrated with these key methodologies have been developed with the objective of simulating the *vivo*-like environment that the living cell experience in an *in vitro* settings[21]. These approaches and platforms not only significantly facilitate the study of cell mechanobiology, but also contribute to the area of biomanipulation where quantitative information about force applied on living cells is concerned.

Although substantial progress has been achieved in developing novel and ef-

ficient tools for force sensing at cellular and subcellular levels, most of these research efforts focused on the hardware platforms while rare research works focused on exploring sophisticated control algorithms to achieve accurate control of dynamic forces applied on living cells. The force control problem proposed by mechanobiology study can be deemed as a specific case of biomanipulation with the objective of explicit force control. Therefore, besides the requirement from conventional biomanipulation (e.g., microinjection), cell mechanobiology further underscores the importance of force control in biomanipulation.

In addition, living cells and biological structures will tune their mechanical properties (significantly in certain contexts) in response to the exogenous forces. This is a key feature that distinguishes living cells from passive materials. Therefore, this time-varying mechanical property should be considered in the force control development for cell mechanobiology.

1.4 Cellular Tensegrity Structure

Tensegrity, an acronym standing for *tensional integrity*, is coined by R.Buckminster Fuller as a structural principle in architecture. Interestingly, in conjunction with its many applications in architecture and smart engineering structures (e.g., [22–24]), it has been drawn on to model and explain cell behavior by Don E. Ingber, according to whom, "A tensegrity system is defined as an architectural construction that is comprised of an array of compression-resistant struts that do not physically touch one another but are interconnected by a continuous series of tension elements". Such tensegrity models proposed for living cells are referred to as cellular tensegrity structure or cellular tensegrity model. They serve as an important alternative model paradigm for depicting cell mechanical behavior, in addition to the ad hoc mechanical models. They are widely studied for understanding mechanobiology, mechanosensing and mechanotransduction.
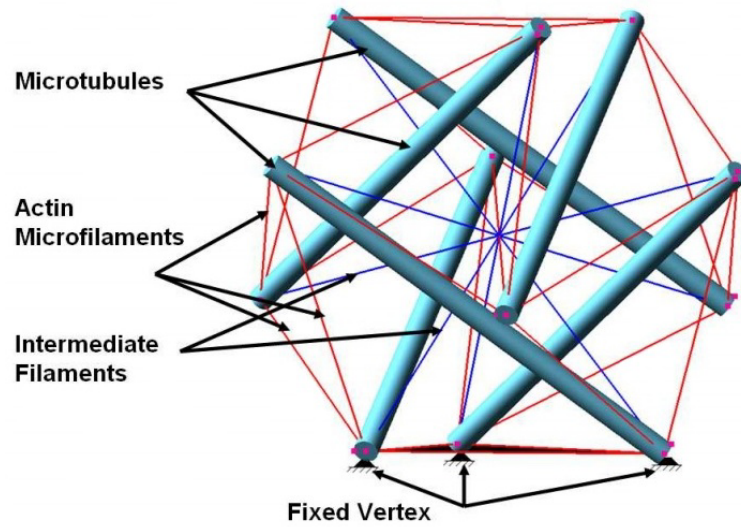
Figure 1.1: Tensegrity model of the cell. Adapted from [2].

Cellular tensegrity models are the most recognized and promising among the models for living cells constructed from structural approaches. The cellular tensegrity model underlies that CSK is mechanically active, which is supported by experimental observations at both cell level and population level. The central assumption of the cellular tensegrity model is that the cytoskeleton (CSK) as a internal structural component of a cell is the main contributor to the stabilization of cell shape. This assumption distinguishes the cellular tensegrity model from continuum models which normally deem the cell as a viscous fluid comprised by a membrane. As such, compared with continuum models, the cellular tensegrity model is able to provide a biomechanics perspective for the understanding of intracellular and extracellular biological/mechanical processes. Therefore, the study of tensegrity model will advance the understanding of cell behavior at the molecular level built upon a cellular biophysical basis.

CSK consists of three classes of filaments: microtubule, actin filaments and intermediate filaments. Among these filaments, microtubules have the highest average stiffness and intermediate filaments have the lowest. In the cellular

tensegrity structure, microtubles are treated as the elements bear compression while actin filaments and intermediate filaments are treated as the elements bear tension (as shown in Figure 1.4). With this general rule, different theoretical studies have been undertaken to examine the mechanical property/behavior of a number of cellular tensegrity models. These studies have indicated that a six-strut minimal tensegrity structure is capable of simulating many aspects of cell mechanical behavior and providing plausible explanations for such behaviors from biological perspective. One representative example is that tensegrity structure displays a nonlinear stiffening response to external loading which resembles living cells. It should be noted that the introduction of tensegrity to modeling cell behavior has many deep biological implications while this thesis concentrate more on the mechanical property the cellular tensegrity structure exhibits, which concerns the externally applied stimuli (e.g., force) and how cells deform under this stimuli.

Despite the well acceptance of cellular tensegrity model, to the best of our knowledge, it has not been used for force control in biomanipulation. Most of the models for cells or other biological materials are constructed by the continuum approach due to its clear advantage that its constitutive equations can be derived from experimental observations. However, the more comprehensive description of the nonlinearity and dynamic coupling of internal structural elements provided by cellular tensegrity model should be leveraged on. Moreover, to employ cellular tensegrity model for force control well suits the requirements of force control in cell mechanobiology since it provides not only the comprehensive mechanical description of mechanical behavior of cells under external force but also many biological insights and implications.

Besides the model shown in Figure 1.1, there exist a number of tensegrity models. This work focuses on the six-strut tensegrity model because of its popularity and representativeness. However, it should be highlighted that the type of

11

tensegrity model should be chosen to best fit the particular biological structure under investigation.

1.5   Objectives and Significance

From above review, it is noted that a growing number of research efforts from the engineering community have been made to develop high-performance automated biomanipulation systems with the objective of fulfilling novel and demanding requirements for applications in biological research. In particular, it is noted that the study on speed design in automated microinjection system has not been explored. Another important issue is that sophisticated force control techniques are necessary to fully realize the potential of existing biomanipulation systems. Moreover, the study of cell mechanobiology has further motivated the study of force control in biomanipulation. Furthermore, the more comprehensive and competent cellular tensegrity models should be explored for force control in biomanipulation.

Following the overall objective to enhance the capability of biomanipulation system, this study firstly aimed at investigating the injection speed and its effects in automated microinjection system for zebrafish embryos. The first contribution is to facilitate understanding the effects of different speeds in automated microinjection. Another major contribution is to provide a systematic way of designing an optimal injection speed to achieve better outcome in the context of improving survival rate. An potential contribution is to benefit the general problem of optimizing the localized force-bearing interaction between a manipulator and a viscoelastic environment in micro/macro-manipulation.

The second objective of this study was to develop force control techniques for biomanipulation based on cellular tensegrity model. This represents an initial

12

step in analytical investigation of localized force-bearing interactions between a cellular tensegrity model and an external mechanical manipulator. This is also the pioneering study of developing force control technique based on the models from structure approach, which explicitly considers the dynamics of the cytoskeleton. Moreover, the developed force control approach directly contributes to the advancement of biomanipulation tools and techniques for mechanobiology. Another potential area where the developed force control techniques can be applied is microinjection since at the operational level, the key objective in a microinjection process is to apply a dynamical force on the surface of a cell in order to pierce the cell membrane.

1.6 Outline

This chapter presents the research background, objectives and significance. The remainder of this thesis is organized as follows:

Chapter 2 firstly reviews the advancements in automated biomanipulation systems with the role of speed and force highlighted. Subsequently, the dynamics of the well accepted cellular tensegrity model from structure approach is reviewed. Lastly, a number of the control results of neural network based control techniques for multi-input multi-output systems are reviewed considering their potential in developing force control techniques.

Chapter 3 formulates a speed optimization problem in microinjection process for zebrafish embryos and provides simulation and experimental results.

Chapter 4 presents the development of force control technique based on a cellular tensegrity model with model uncertainties and partial state measurability.

Chapter 5 presents the development of force control technique based on the

cellular tensegrity model with time-varying mechanical properties.

Chapter 6 presents the force tracking control in biomanipulation using neural networks.

Chapter 7 summarises the work done in this thesis and discusses the future research directions.

Chapter 2

Literature Review

This Chapter presents a review of the existing literature on automated biomanipulation system. Firstly, the advancements in automation of microinjection system for zebrafish embryo are summarized. Secondly, the existing force sensing techniques and force control strategies for biomanipulation are reviewed. As force control requires modeling of the dynamic behavior of cells, the studies of mechanical behavior of cellular tensegrity models are subsequently introduced. Lastly, a number of neural network based control techniques for multi-input multi-output systems are reviewed in the context of their potential for automated biomanipulation. In particular, results for tracking control of nonlinear systems with input saturations are discussed.

2.1   Automation in Microinjection System

Over the last decade, automation of microinjection processes has attracted extensive research attention in the engineering community. A number of automatic microinjection systems have been reported for an array of cell types. The cells involved in microinjection can be classified into two general groups: ad-

15

herent cells (e.g., neurons, heart cells and liver cells) and suspended cells (e.g., oocytes) [3]. Adherent cells are of irregular-shape and attached to a surface while suspended cells are of rounded shape and can move freely. Furthermore, adherent cells (usually with a diameter between $10\mu m$ to $20\mu m$) are normally much smaller than suspended cells. For instance, zebrafish embryo, as a type of suspended cell, has a diameter of $800\mu m$. Due to these significant differences between adherent cells and suspended cells, microinjection systems are designed accordingly to address their respective challenges.

The common operation of microinjection system for adherent cells involves moving a fine microcapillary (since the adherent cell is small) to penetrate the cell membrane with its tip and subsequently apply a pressure pulse to inject the material in the capillary into the cell. The main challenge is to position the microcapillary properly such that its tip can penetrate the cell membrane while inducing minimal damage on the cell. This requires a highly accuracy mechanical system and high performance positioning control. Another main issue is the detection of the contact between cell and microcapillary since the tip of fine microcapillary only about $1\mu m$. To address this contact detection problem during injection process, an injection guidance system integrated with the automatic micromanipulator MANiPEN (as shown in Figure 2.1) is developed [25] through an impedance measurement device.

Owing to the prevalence of oocytes in microinjection process, many research efforts have been focused on developing automatic microinjection systems for suspended cells. These efforts mainly aim at solving a wide range of problems in both hardware design (e.g., microrobotics, cell-holding device and vision system) and software design (e.g., visual servoing control and injection force control). In [4], a prototype of microinjection system using autonomous micro-robotics is developed (as shown in Figure 2.2(a)). The automation is achieved based on a visual servoing control strategy which is capable of precisely po-
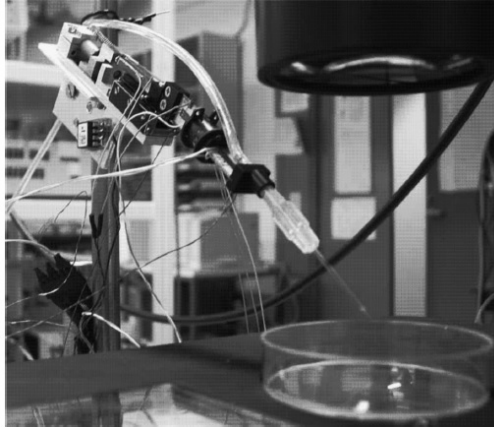
Figure 2.1: MANiPEN micromanipulator. Adapted from [3].

sitioning the tip of the micropipette to the desired location within the mouse embryo (as shown in Figure 2.2(b)).
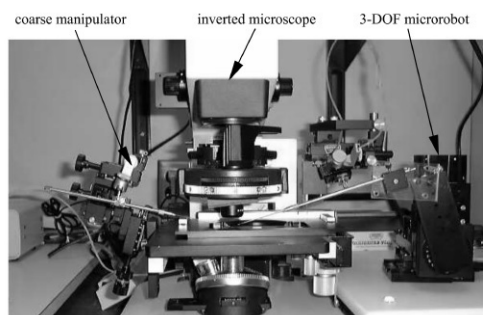
(a)
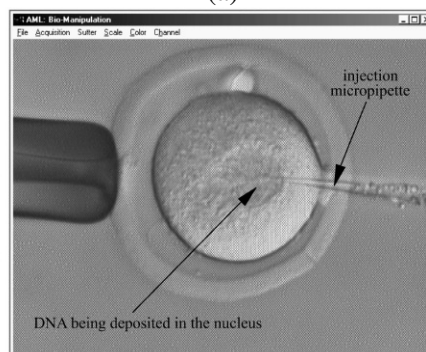
(b)

Figure 2.2: (a) Autonomous embryo injection system. (b) Teleoperated embryo injection. Adapted from [4].

Several promising prototypes of autonomous microinjection system attempting

to solve efficient batch injection are reported in the literature. In [5], a specially designed holder featuring an array of V-grooves immobilizing zebrafish embryos is proposed (as shown in Figure 2.3(a)). A machine vision algorithm is developed to identify the center line of each zebrafish embryo within field of view as the trajectory for the micropipette to follow (as shown in Figure 2.3(b)). When the micropipette is aligned with the center line and moves towards the center of the embryo, the contact force between the tip of micropipette and the embryo membrane is recorded. The contact force will drop sharply when the membrane ruptures and this is used as part of the force profile for position control of the micropipette.
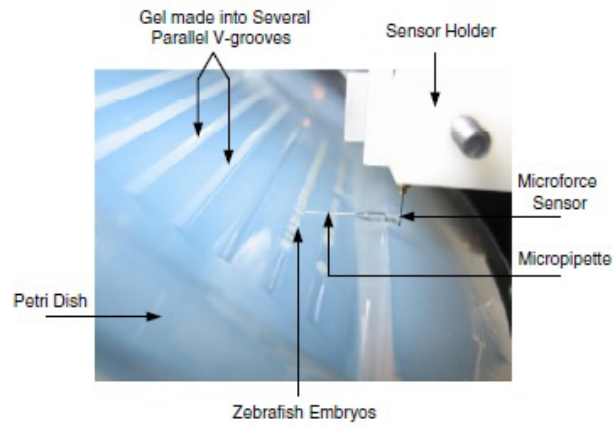
(a)
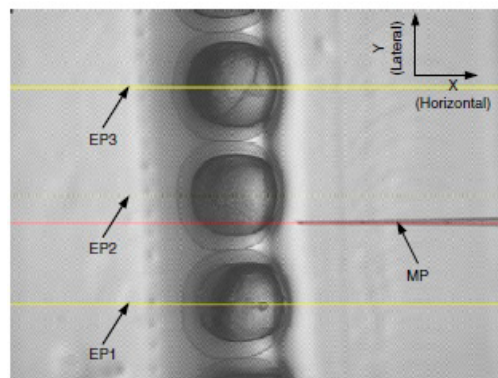
(b)

Figure 2.3: (a) Close view of injection area. (b) Centerlines of the zebrafish embryos and micropipette. Adapted from [5].

In [6], motivated by the need for efficiently positioning the zebrafish embryos

18

for injection, which is the bottleneck of automatic process, a vacuum-based embryo holding device with an array of through holes is developed (as shown in Figure 2.4). These through-holes trap zebrafish embryos when vacuum is applied. Image processing algorithm is developed to recognize the internal structure of zebrafish embryo to identify the deposition destination. In [7], another cell-holding device for streamlining the laborious pick-and-place process is presented (as shown in Figure 2.5). This device can swiftly transport zebrafish embryos into the field of view for injection and immobilize them.
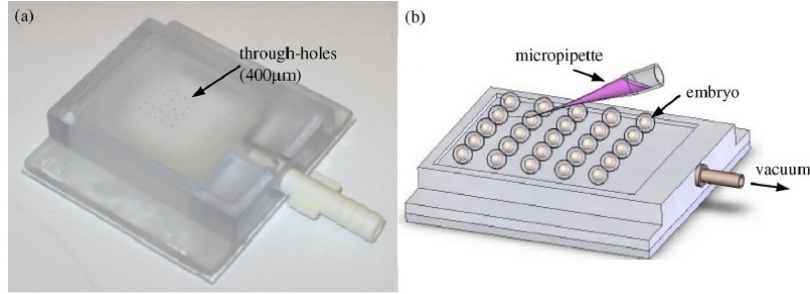
Figure 2.4: Vacuum-based zebrafish embryo holding device: (a) Device picture; (b) Device schematic with embryos immobilized for injection. Adapted from [6].

2.2 Force Sensing and Control in Biomanipulation

Various bioengineered platforms have been developed to permit quantitative investigation of the force cell sustains. These platforms are capable of applying and measuring controlled mechanical forces to the order of nano/pico Newton. Furthermore, they are often equipped with vision systems to provide the displacement information of how cells are deformed, extended, or depressed by the applied force. With these platforms, characterization of the mechanical property of cells and modelling of the dynamics of cells are enabled. Moreover, based on these platforms, some control schemes are proposed to realize the control of force applied on cells so as to enhance the biomanipulation process. This section reviews some of the key force sensing techniques in biomanipulation and
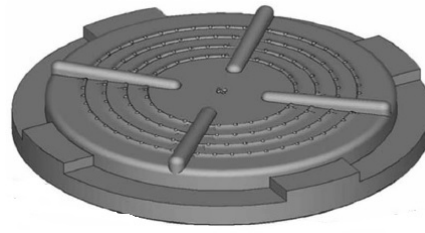
(a)
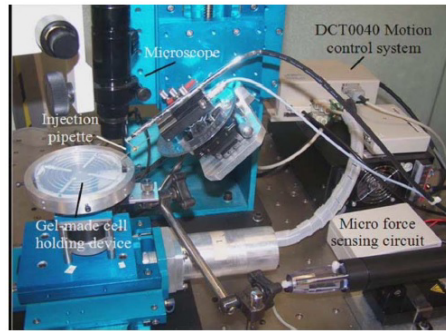
(b)

Figure 2.5: (a) CAD prototype of mold for cell-holding device.   (b) Laboratory test bed suspended cell-injection system. Adapted from [7].

the force control in biomanipulation.

2.2.1   Force Sensing Techniques in Biomanipulation

In biomanipulation, owing to the fact that biological cells are highly delicate and deformable, quantification of interaction force between the end-effector and cell is challenging. To address this issue, various innovative force sensing techniques are proposed[14][21]. Among these techniques, the most representative and practical micro/nano force sensing techniques are MEMS-based, Polyvinylidene fluoride (PVDF) film based, piezoresistive material based and vision based.

MEMS-based force sensing is one of the promising micro/nano force sensing techniques on account of the match between the micrometer scale size of most oocytes and the feature sizes of MEMS. Another merit of MEMS-based sensors
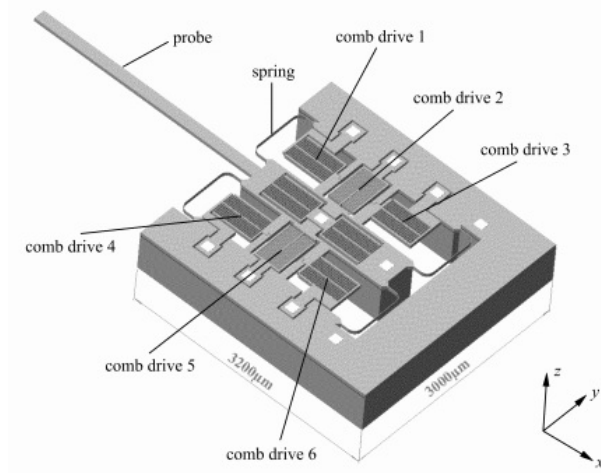
Figure 2.6: Solid model of the multiaxis cellular force sensor. Adapted from [8].

rendering them popular in biomanipulation is that they are able to be used in aqueous environment In [8], a MEMS-based two-axis capacitive cellular force sensor is presented. This device is able to provide real-time force feedback during cell manipulation. As illustrated in Figure 2.6, the device has a movable inner structure, which moves when a force is exerted on the probe and subsequently results in capacitance change. The device is capable of resolving a maximum force of $490\mu N$ with a resolution as low as $0.01\mu N$ in x direction, and a maximum force of $900\mu N$ with a resolution of $0.24\mu N$ in y direction. Based on this MEMS-based capacitive force sensor, a similar monolithic micro-gripper for the application of picking-and-placing cells is reported in [26]. This micro-gripper is integrated with force sensing capability to feedback the gripping force information.

PVDF film, as a piezoelectric material, has been explored to fabricate the potential force sensors in Micromanipulation on account of its high mechanical strength and high sensitivity [27]. PVDF micro-force sensors for microinjection systems are often used to hold the micropipette (as shown in Figure 2.7) so as to measure the contact force between micropipette and the cells [9]. In [28], an two-axis *in situ* PVDF micro-force sensor with resolution of sub-micro Newton
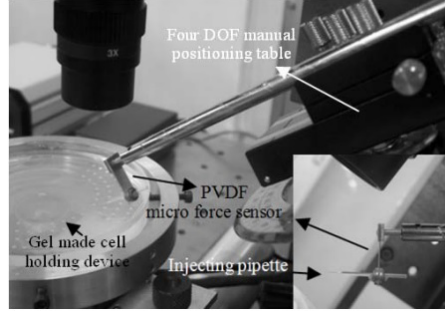
Figure 2.7: PVDF force sensor used for zebrafish embryo injection. Adapted from [9].

is developed to identify the force profile of microinjection of living Drosophila embryos. In [10], a novel force sensing approach based on the beam structure which supports the zebrafish embryo during injection is proposed. The PVDF film is adhered to the supporting beam and therefore deforms with the beam (as shown in Figure 2.8). The advantage of this sensing scheme is that it minimize the interference to the injection system since the force sensing and injection are independent, which differs from the majority of sensing techniques using integration of force sensing and end-effector (e.g., micropipette).

Piezoresistive micro force sensor provides force information through measuring

(a)

(b)
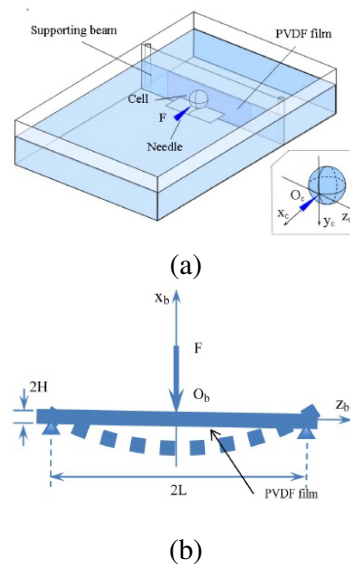
Figure 2.8: (a) Force-sensing structure of the PVDF force sensor. (b) PVDF film with beam structure. Adapted from [10].

its resistance variance, which is a function of the external mechanical loading exerted on it. The main merit of stable force signal is its capability of providing stable force signal within a relatively large measurement range[29]. In [5], a commercial cantilever-based piezoresistive force sensor (SensorOne Technologies Corporation, model AE801) is modified by gluing a shortened micropipette to the free end of the cantilever (as shown in Figure 2.9) to measure the contact force between micropipette and zebrafish embryo.
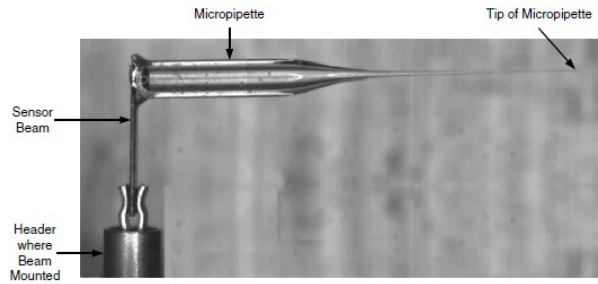
Figure 2.9: Side view of the modified piezoresistive micro-force sensor with the micropipette. Adapted from [5].

Vision-based techniques have also been developed to measure the micro/nano level force. In these techniques, polydimethylsiloxane (PDMS), which is an type of extremely compliant material, is often used to sense the force. The force sensing is realized through image tracking of the deformation of PDMS to provide the displacement information and subsequently convert to force information. In [30], a two-dimensional PDMS micro-force sensor is fabricated for microrobotics is presented. For the purpose of biomanipulation [11], the nano-force measurement in microinjection is achieved by measuring the deformation of the post (made of PDMS) supporting cell under injection in the cell holding device. This sensing scheme is motivated to circumvent the end-effector exchange problem, which is due to the fact that the end-effector (e.g., micropipette) and force sensor (e.g., piezoresistive beam) are glued together. The sub-pixel visual tracking algorithm is developed to track the deflection of the post during injection and provides a resolving force down to $3.7nN$.
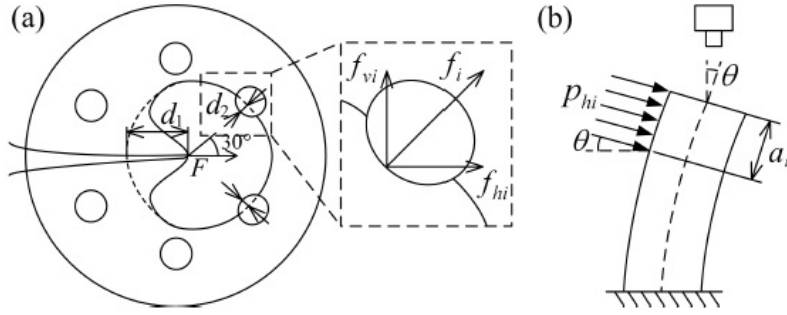
Figure 2.10: (a) Force balance on the cell under indentation. (b) Post deflection model. Adapted from [11].

2.2.2 Force Control in Biomanipulation

Compared to the extensive research attentions on development of micro/nano force sensing techniques, few have been dedicated to explicitly controlling force in biomanipulation. In this section, an overall review of force control is presented first. Subsequently, some works on regulating the force for the purpose of enhancing microinjection process are reviewed.

Force control in general has been an important research area in robotics since many applications of robot require manipulator interact with its environment. During the development of robot force control, several control algorithms have been explored and refined to provide robotic systems with enhanced capability in managing the interaction between end-effector and environment[31][32]. In literature, force control can be classified as direct force control and indirect force control. The key difference between these two categories is that the former has an explicit force feedback loop to realize force control whilst the latter realizes force control through motion control. The most recognized indirect force control strategy is impedance control, which which achieves compliant motion control through explicitly controlling end-effector position in the unconstrained subspace and interaction force in the constrained subspace [33].

Impedance control is the most studied indirect force control since it achieves designed force control performance through introducing a prescribed dynamic relationship between contact force and position error[34]. Based on these fundamental interaction control strategies, many advanced force control algorithms integrating robust control and adaptive control are developed [35].

Force control usually requires the modeling of the environment which the end-effector is interacting with. The linear spring model of environment with constant stiffness is the mostly used model. This widely adopted model is representative of many situations where stiffness is the dominant factor of the interaction dynamics[36]. Besides, stiffness is the most important characteristic for stability analysis[37]. The Kelvin-Voigt spring-damper mode is another popular model since it considers the dissipation of energy by combining the damping term which introduce a damping force.

With the various developed force sensing techniques as reviewed in previous section, a number of force control techniques have been reported with the purpose of controlling the penetration force in automated microinjection system. In [11] and [38], proportional-integral-derivative (PID) is employed on account of its robustness. In [7][13] and [39], impedance control is employed to render the penetration force track a reference trajectory, which is obtained via learning the manual injection by a human expert. The impedance is designed such that severe oscillation and large overshoot are avoided to reduce the damage induced by injection. The contact force is modelled simply as a polynomial function of the deformation of the cell. Hence, the desired interaction dynamics are given by[39]

$$
\begin{cases}
m\ddot{x} + b\dot{x} + kx = f_r - f_e \\
f_e = \sum_{i=0}^{n} C_i x^i
\end{cases}
\tag{2.1}
$$

where m, b and k are positive constants, representing prescribed mass, damp-

ing and stiffness respectively; x is the deformation of cell; f_r is the reference force and f_e is the contact force; C_i is the parameter of the polynomial function. A control law based on feedback linearization is designed to achieve the desired dynamics 2.1 and asymptotical convergence of force tracking error is ensured.

2.3 Review of Cellular Tensegrity Model

Approaches based on continuum and structural mechanics have been shown to be useful in constructing mechanical models of living cells [40][41]. The tensegrity model of cell deformability offers a potentially more effective alternative, because it is capable of simulating many aspects of cell mechanical behavior and providing biologically plausible explanations for such behavior [42–45]. The recognition that the cellular tensegrity mode leads to new insights about cellular behavior further prompts the proposition of many cellular tensegrity structures. These proposed tensegrity structures are analyzed through their distinct physical response characteristics, which are compared with the experimental observations to gain understanding on how a cell physically responds to external mechanical stimuli. Among the different tensegrity structures developed for cell mechanics, the numbers of elements in compression and in tension vary significantly. Sometimes the hierarchy of the tensegrity structure is also designed differently depending on the types of cells and assumptions.

There is increasing evidence supporting the validity of cellular tensegrity model. In [45], a number of sophisticated experiments are carried out to demonstrate that the microtubule which bears compression is the main contributor to cellular mechanics, and that prestress exists within CSK and plays a critical role in guaranteeing the shape stability of the cell. These two observations are consistent with the key features of the cellular tensegrity model. Moreover, quantitative

26

measurements had been conducted to indicate that the tensegrity model is able to predict many complex cellular mechanical behaviors [41].

2.3.1 Equations of Motion of a Well-Accepted Six-Strut Cellular Tensegrity Model

The effectiveness of the six-strut cellular tensegrity structure in predicting the dynamic behavior in cells is also explored [46][47]. A number of researcher have been investigating the dynamics of tensegrity structure notwithstanding, introducing Lagrangean formulation to derive the dynamics of the cellular tensegrity model is initially proposed in [47]. In this section, a detailed review of using Lagrangean formulations to analyze the dynamics of the well-accepted six-strut cellular tensegrity model is presented. The tensegrity structure employed in [47] ((as shown in Figure. 2.11(a)) is consist of 6 struts and 36 tendons. The bottom three struts $A_i C_i (i = 1, 2, 3)$ are freely rotatable about A_i while the upper three struts $B_i D_i$ are only connected by tendons. Since A_i are fixed, only 33 tendons out of the 36 tendons contribute to the deformation of structure under external load and they are referred as working tendons. A slight modification of this tensegrity model with respect to previous six-strut tensegrity structure in [48] is that the intermediate filaments are incorporated and represented by 12 tendons connecting to a massless point at the geometrical center of the spherical structure.

The struts are considered as rigid bars of identical length L and of negligible inertial property under compression, whereas the tendons as identical viscoelastic Voigt elements. The constitutive equation of a tendon is

$$f_t = k \cdot (l/l_0 - 1) + c \cdot \dot{l}$$
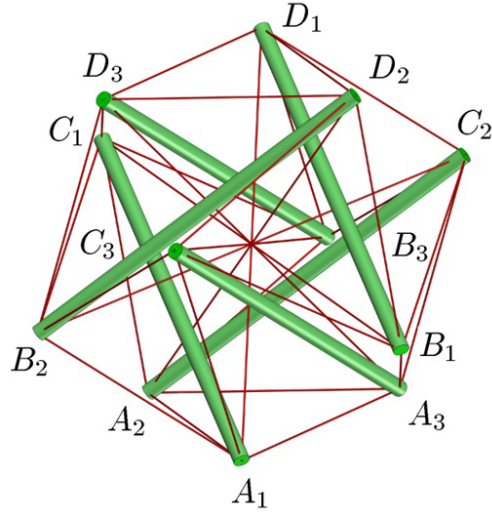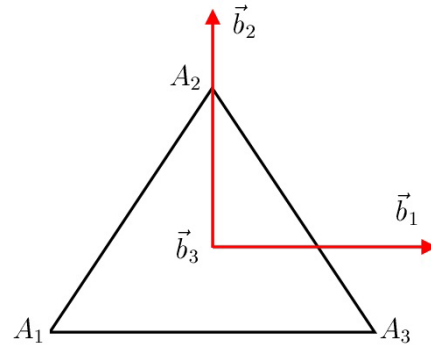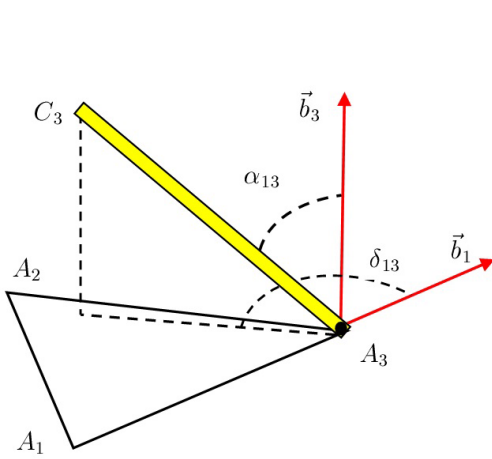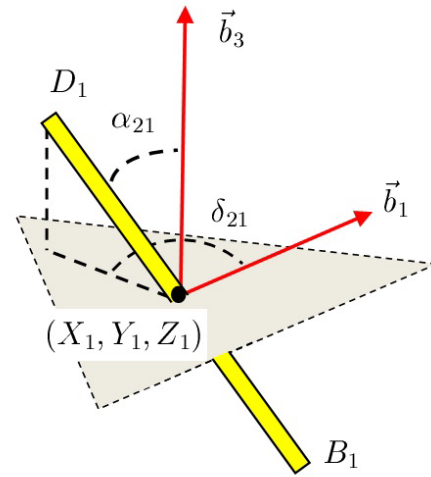
Figure 2.11: (a) A six-strut cellular tensegrity structure. (b) Orthonormal base vectors $(\vec{b}_1, \vec{b}_2, \vec{b}_3)$. (c) Configuration of A_3C_3. (d) Configuration of B_1D_1.

where f_t is the force sustained by the tendon, k is the stiffness, $c > 0$ is the damping coefficient, l and l_0 are the length and the initial length of the tendon, respectively, and $\dot{l}$ is the time derivative of l.

A right handed system of orthonormal base vector $(\vec{b}_1, \vec{b}_2, \vec{b}_3)$ (as shown in Figure 2.11(b)) is introduced to facilitate the mathematical description of the model. The configuration of the tensegrity structure is described by the positions of all the struts (A_iC_i and $B_iD_i (i = 1, 2, 3)$), which are defined by a set of generalized coordinates. The bottom struts A_iC_i are specified by two angles: azimuth α_{1i} (i.e., the angle between the orthogonal projection of the strut on plane $A_1A_2A_3$ and the vector $\vec{b}_1$) and declination δ_{1i} (i.e., the angle between the strut and vector $\vec{b}_3$). For the upper struts B_iD_i, in addition to azimuth α_{2i} and δ_{2i}, the Cartesian coordinates of the geometric center of strut, (X_i, Y_i, Z_i) is introduced to collectively describe the position. Figure. 2.11(c) and Figure. 2.11(d) illustrate the definitions of the generalized coordinates for A_iC_i and B_iD_i, respectively. Lastly, the Cartesian coordinates of the massless point is required and defined as (X, Y, Z). With above defined general coordinates, the vector of generalized coordinates q can be obtained as:

$$
\begin{aligned}
q \ = \ & [\, \delta_{11} \quad \alpha_{11} \quad \delta_{21} \quad \alpha_{21} \quad \delta_{31} \quad \alpha_{31} \quad X_1 \quad Y_1 \quad Z_1 \quad \delta_{12} \quad \alpha_{12} \\
& X_2 \ Y_2 \ Z_2 \ \delta_{22} \ \alpha_{22} \ X_3 \ Y_3 \ Z_3 \ \delta_{32} \ \alpha_{32} \ X \ Y \ Z \,]^T \quad (2.2)
\end{aligned}
$$

The equations of motion can be subsequently derived using Lagrangean formulation

$$
\frac{\partial V}{\partial q_j} = \sum_{n=1}^{7} (F_n^T \frac{\partial \dot{r}_n}{\partial \dot{q}_j} + M_n^T \frac{\partial \Omega_n}{\partial \dot{q}_j}), \qquad j = 1, \ldots, 24 \qquad (2.3)
$$

where, V represent the potential energy; q_j is the jth element of q; F_n and M_n are the resultant force and moment, respectively; n represents the nth rigid body (including both struts and the center massless point); $\dot{r}_n$ is the velocity of the

center of the strut and the point; Ω_n is the angular velocity of the nth rigid body. Let $\mathbb{R}$ and $\mathbb{I}$ denote the set of real numbers and integers, respectively. The equations of motion of the tensegrity structure are:

$$A(q)T(q) + C(q)\dot{q} = H(q)f \qquad (2.4)$$

where
$q \in \mathbb{R}^{24 \times 1}$	:	vector of generalized coordinates,
$A(q) \in \mathbb{R}^{24 \times 33}$	:	equilibrium matrix,
$T(q) \in \mathbb{R}^{33 \times 1}$	:	tensions in the working tendons,
$C(q) \in \mathbb{R}^{24 \times 24}$	:	damping matrix,
$N \in \mathbb{I}$	:	number of external forces and torques,
$H(q) \in \mathbb{R}^{24 \times N}$	:	disturbance matrix,
$f \in \mathbb{R}^{N \times 1}$	:	vector of external forces and torques.

The elements of $A(q)$, $T(q)$, $C(q)$ and $H(q)$ are given in Appendix A.

2.3.2 Prestressability and Reference Solution

One of the most important and unique feature of tensegrity model is their *prestressability* [49], which indicate to the extent of stretching the tendons sustain. Prestressability directly associate the capability of the structure to maintain the equilibrium configuration when no external loads are applied. The equilibrium configuration is considered as the reference solution for Equation (2.4). The reference solution depends on prestressability, which is described by two parameters: prestress P and basis tensions T_0. P is a positive constant while T_0 is the vector of the basis tensions at equilibrium configuration. At equilibrium configuration (i.e., reference solution), the tension matrix can be expressed as

$$T(q_0) = PT_0 \qquad (2.5)$$

q_0 is the reference solution. Provided P and T_0, the corresponding generalized coordinates can be obtained. The basis tensions T_0 at reference solution are set

30

according to the classes of the tendon, which are defined as follows[47]: the intermediate filaments (I) class which consist of the tendons connected to the center of structure; the saddle (S) tendons class which consists of the tendons connecting B_1, B_2, B_3, C_1, C_2 and C_3; the top (T) tendons class which consist of the tendons connecting D_1, D_2 and D_3; the diagonal (D) tendons class which consists of A_1B_2, A_2B_3, A_3B_1, D_1C_2, D_2C_3 and D_3C_1; the vertical (V) tendons class which consists of A_1C_3, A_2C_1, A_3C_2, D_1B_3, D_2B_1 and D_3B_2. The values of the basis tensions at tension are assumed to be : $T_0^S = 0.210$, $T_0^V = 0.219$, $T_0^D = 0.226$, $T_0^T = 0.213$ and $T_0^I = 0.022$.

2.3.3 Three-Dimensional Finite-Element Cellular Tensegrity Models

In addition to analyzing the dynamics of cellular tensegrity models, finite element method (FEM) has been applied to simulate how cellular tensegrity models deform under various external loads. By employing the six-strut tensegrity structure as shown in Figure 2.11(a) as the central component, a computational three-dimensional finite-element model of an adherent eukaryotic cell is developed to simulate structural response of the cell under the usual mechanical stimuli (e.g. fluid flow) [50]. An important advantage of using FEM for simulating the deformation of tensegrity structure is that complex tensegrity structure is able to be considered. For instance, in [51], a tensegrity structure of 30 struts and 30 cables is analyzed to simulate the transmission of mechanical load applied on the surface. Moreover, it possesses both external structure and internal structure and the interconnecting elements between the external structure and the internal structure. In both [50] and [51], besides cytoskeleton, the finite element model incorporates some other structurally significant cellular components (i.e., nucleus, cytoplasm and membrane) that influence the mechanical behavior

31

of the cell.

A three-dimensional finite-element model similar to [47] is proposed in [2] for use as a virtual training environment for microinjection operations; it represents the first attempt to simulate the reaction force from a deformed tensegrity structure. In all these important research works on cell dynamics modeling, the external force considered to be experienced by the cell is often in the form of a static load. The interaction between the viscoelastic behavior of the cell and an dynamically applied external force has yet to be fully explored.

2.4 Neural Network Control of Multi-Input Multi-Output Nonlinear systems

A brief review of control of multi-input multi-output (MIMO) system is provided in this section since the force control for manipulator with multiple degree of freedom is essentially a control problem of MIMO nonlinear systems. As an effective control strategy for control of MIMO systems, a special interest is given to radial basis function neural network (RBFNN) based controller. In particular, NN-based control techniques for MIMO systems with input saturations is reviewed.

The control of MIMO nonlinear systems is a practical yet challenging problem since most of engineering systems are multivariable and nonlinear. The control challenge is mainly due to the couplings of both inputs and outputs. Moreover, the uncertainties and nonlinearities in the input coupling matrix lead to further complication[52]. It is therefore important to develop effective control techniques for uncertain MIMO systems. Among the available control techniques for control of uncertain MIMO nonlinear systems (e.g.,[53–58]), neural network (NN) based adaptive controller has attracted considerable interests. Various con-

32

trol strategies have been developed, with most of them focusing on integrating the neural networks to the robust adaptive control techniques under the scheme of the popular backstepping approach[52, 59–63]. In [52], the singularity problem of the control input matrix has been overcome by leveraging on the properties of the MIMO systems in block-triangle form. In [60], the developed NN based robust control design relaxes the requirement for off-line training. These results have demonstrated that NN based controllers are effective for control of highly nonlinear systems with uncertainties.

2.4.1 Radial Basis Function Neural Network Based Control of MIMO systems

For the purpose of nonlinear control, the most widely applied NNs are radial basis function neural networks (RBFNNs), high-order neural networks (HONNs) and multilayer neural networks (MNNs)[64]. RBFNNs have been extensively studied to approximate the unknown dynamics of the MIMO system on account of their outstanding capability in modeling highly nonlinear functions[65]. They have been widely applied to tackle various control problems for MIMO systems [52, 66–70]. In the aforementioned works, RBFNNs are used to approximate a continuous function $h(Z) : \mathbb{R}^q \to \mathbb{R}$ over a compact set $\Omega_Z \subset \mathbb{R}^q$ in the following way:

$$h(Z) = W^{*T}S(Z) + \epsilon \tag{2.6}$$

where $Z \in \mathbb{R}^q$; W^* is ideal NN weights vector; ϵ is the approximation error corresponding to the ideal NN weights; $S(Z)$ is the basis function vector. As proven in [65], (2.6) is able to approximate $h(Z)$ to arbitrarily any accuracy.

2.4.2 Control of Nonlinear Systems with Input Saturations

Physical dynamical systems are inevitably suffer from input constraint due to actuator limitations in magnitude and rate. This may severely degrade system performance if handled inappropriately. Various attempts have been made to address this issue(e.g., [68, 69, 71–79]). In [76], a modified tracking error system is developed as a novel strategy to deal with the adaptation process for on-line approximation when input saturation occurs. The main advantage of the proposed control system is to protect the learning capabilities in presence of input saturation. In [78], an adaptive backstepping control scheme using command filters to emulate actuator physical constraints on both the control law and the virtual control laws is presented. The issue of input constraints is more complicated for uncertain nonlinear MIMO systems. In [68], the auxiliary system design in [76] is extended to guarantee the H^{∞} performance for a general class of nonlinear MIMO systems with uncertainties in the presence of both disturbances and control input constraints. A model-based adaptive control is developed in [79] to handle the non-symmetric input saturation and a NN-based robust controller is developed in [69] to resolve a general input nonlinearity concerning both input saturation and deadzone. In both works, a new type of auxiliary system design is proposed with its signal utilized in the designed control law. The semi-global uniformly ultimate boundedness of all the signals in the closed-loop system is achieved in presence of input saturations by virtue of the special design of the auxiliary system.

Chapter 3

Speed Optimization in Automated Microinjection of Zebrafish Embryos

3.1 Introduction

Microinjection of zebrafish embryo is a common practice in studying the early developmental processes of biological organisms. Zebrafish embryo serves as a widely used experimental subject in biology on account of its some unique characteristics. These characteristics includes that the embryos are transparent and genetically manipulatable. Besides, the fast development of its embryo is another attractive feature. The development of zebrafish embryos and the embryo structure are shown in Figure 3.1 and Figure 3.2, respectively.

Conventional manual microinjection usually involves an operator moving the micropipette towards the embryo until its tip slightly touches the chorion, then driving the micropipette to pierce the chorion and maneuvering the tip of the
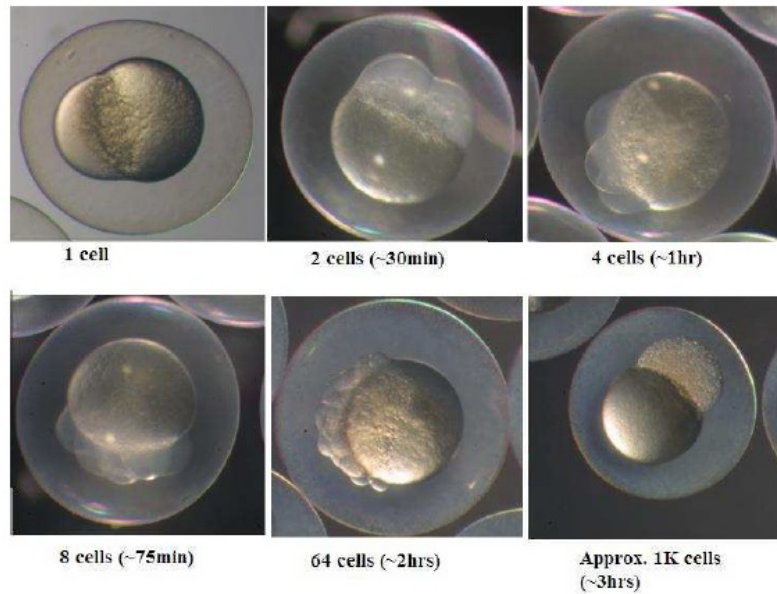
Figure 3.1: The development cycle of zebrafish embryo

micropipette to a desired location inside the embryo to delivery the DNA mate-
rial. Such manual operation relies on visual information from optical devices to
guide the operator, and is prone to errors (due to various human factors such as
fatigue). Approaches reported in the literature for improving the process mainly
concentrate on providing haptic feedback to the operator (e.g., [16]).
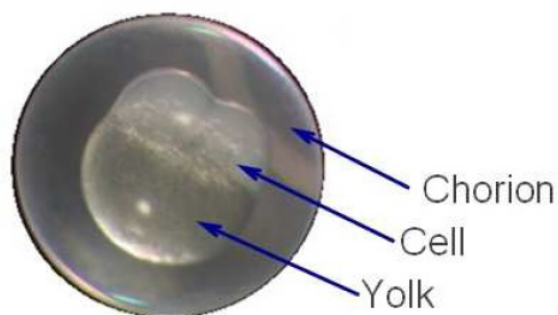
Figure 3.2: Structure of a zebrafish embryo

36

3.2   Motivation

In automated microinjection involving zebrafish embryos, the motion of the micropipette (which induces deformation in the embryo) may cause damage to the embryo, thus rendering the injected embryo useless. The work reported in this chapter was motivated by the need to avoid such damage while improving the efficiency of the process. The performance of a microinjection process can be evaluated in various context. From a pure biological perspective, the survival rate of the injected embryos is one key performance indicator. From a bio-mechanical perspective, the deformation sustained by the embryo is an important factor to consider, since a large deformation can damage the embryo to the extent of adversely affecting its survivability. For this reason, developing engineering tools for microinjection with the main objective of reducing embryo deformation remains an active research area.

3.3   Dynamics Model of Zebrafish Embryo

Under indentation zebrafish embryos exhibit viscoelastic behavior that can be described by analytical models [80][40]. In particular, when the micropipette indents an embryo at different speeds, the peak contact force and the embryo deformation vary accordingly. The applied force, the speed of indentation, and the deformation of the embryo form a complex dynamical relationship.

Figure 3.3(a) shows a typical (side view) image illustrating the indentation of a zebrafish embryo. A micropipette exerts on the membrane an indentation force, which compresses the embryo to create a dimple around the point of contact. The left half of the embryo is characterized by the dimple due to the indentation, while the right half is characterized by the planar circular contact surface formed on the rigid supporting wall.
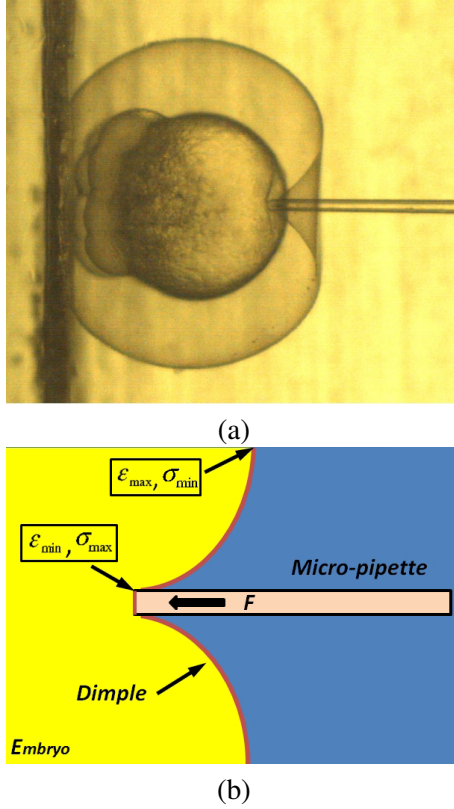
Figure 3.3: (a) Indentation of the zebrafish embryo membrane by a micropipette. (b) The distribution of stress and stain in the deformed membrane, where the symbols ξ and σ denote stress and strain, respectively (max stand for maximum and min stand for minimum). F denotes the contact force between the micropipette and the membrane of the embryo.

Figure 3.3(b) illustrates the force and strain information during zebrafish microinjection process([80]). The microinjection process is assumed to start from the moment the micropipette first makes contact with the chorion. The tip of the micropipette creates a small planar circle contact with the membrane. This is referred to as the dimple top. The stress sustained by different part of the membrane varies. Maximum stress in the membrane occurs at the perimeter of the dimple top because the edge of the tip of the micropipette is pressed against the membrane. The dimple top is considered the fixed end of the overall (deformed) membrane. Thus the strain on the membrane at the dimple top is zero. For the deformed portion of the embryo, starting from the dimple top the stress (strain) of the membrane gradually decreases (increases) along the curved perimeter, reaching its minimum (maximum) at the dimple base.

In the remainder of this section, a dynamics model of the zebrafish chorion under indentation is constructed, and its parameter values are determined experimentally.

3.3.1 Dynamics Model

A Maxwell-Wiechert model with two Maxwell elements [81], as shown in Figure 3.4, is adopted and the values of its parameters through a set of experiments are estimated.

The following assumptions facilitate the application of this Maxwell-Wiechert model in the context of microinjection:

Assumption 3.1: The micropipette is kept in contact with the membrane of the embryo such that the deformation of membrane is considered to be exclusively caused by the movement of the micropipette.

Assumption 3.2: The deformation of embryo is adequately described by the

depth of indentation on the membrane. This is consistent with the fact that the depth of indentation is a dominant variable in describing such deformation[80].

Assumption 3.3: The reaction force, generated by the membrane under indentation, directly correlates with the stress sustained by the membrane so that whether a membrane has been ruptured due to the indentation can be directly deduced from the magnitude of the reaction force.
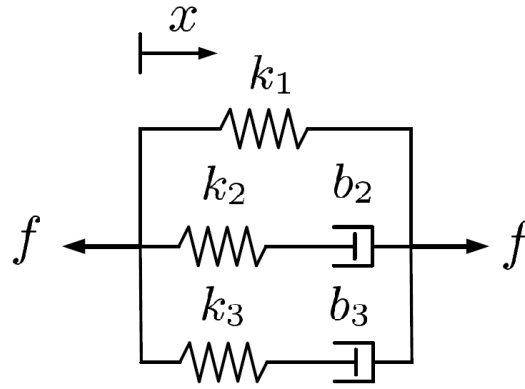
Figure 3.4: Maxwell-Weichert model having two Maxwell elements.

The total force in the Maxwell-Weichert model (as shown in Figure 3.4) can be expressed in the Laplace domain as:

$$F(s) = \left(k_1 + \frac{k_2 s}{s + k_2/b_2} + \frac{k_3 s}{s + k_3/b_3} \right) X(s) \tag{3.1}$$

where $X(s)$ is the deformation and $F(s)$ is the indentation force acting on the membrane. For a single indention step, it is obtained that (in the time domain)

$$x(t) = \begin{cases} \displaystyle\int_0^t v(\tau)\, d\tau & \text{for } 0 \leq t \leq t' \\ x(t') & \text{for } t > t' \end{cases} \tag{3.2}$$

where v is the speed of the micropipette and t' is the time when the micropipette stops its indenting motion. Combining Equations (3.1) and (3.2) yields the rela-

tionship (in the time domain) among f, x, and v:

$$f(t) = k_1 x(t) + \sum_{i=2}^{3} k_i \int_0^t v(\tau) e^{-\alpha_i(t-\tau)} d\tau \qquad (3.3)$$

where $\alpha_i = k_i/b_i$, with $i = 2, 3$. The values for the parameters k_1, k_2, k_3, b_2, and b_3 were estimated by experiment, as described below.

3.3.2 Estimation of Parameter Values

A prototype general-purpose micromanipulation system was utilized to attain empirical data for estimation of parameters in Equation (3.3). Figure 3.5 illustrates the components of this system.
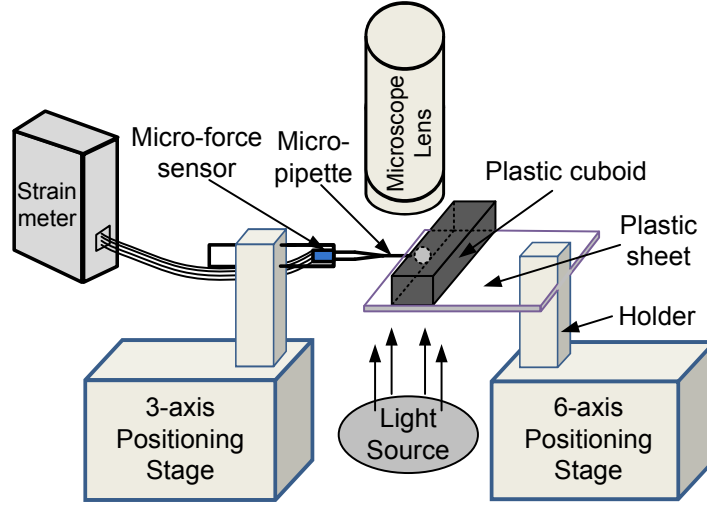
Figure 3.5: A plastic cuboid, with its bottom glued to a transparent plastic sheet, contains the zebrafish embryo. It has a vertical wall to keep the embryo stationary when being indented by the micropipette (which is actuated by a 3-axis positioning stage). The holder that supports this sheet is mounted on a 6-dof motion stage that can be manoeuvred to algin the wall of the cuboid to be perpendicular to the direction of motion of the micropipette. A force sensor, incorporated in the micropipette, measures the indentation force, while a digital camera, positioned directly above the cuboid, captures the view of the microscope.

The embryo holder device is made of a plastic cuboid with its bottom glued

to a transparent sheet. The height of the cuboid is marginally greater than the embryo. The reason of this design is to guarantee that the vision system is able to fittingly focus on the edge of the rectangular cube and the perimeter of the embryo. The cuboid serves as a stopper to immobilize the embryo under indentation by the micropipette. As illustrated in Figure 3.6, a small water pool was formed by adding some water into the surroundings of the embryo.
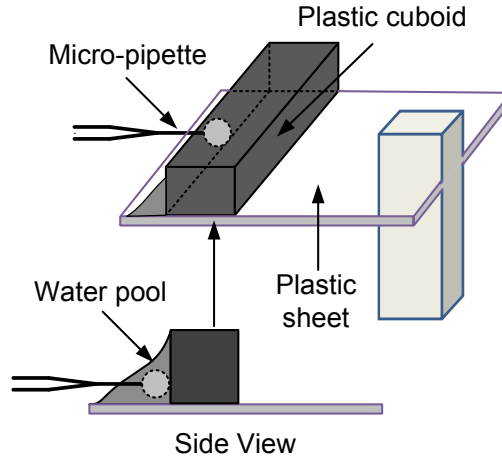
Figure 3.6: Schematic illustration of (a) the overall micromanipulation system; (b) the small pool area.

The holder was mounted on a high-precision six-axe motion stage. Another three-axe positioning stage was used to move the micropipette. A micro-force sensor (mounted onto the micropipette) measured the indentation force, as shown in Figure 3.7. The micro-force sensor was originally developed in [29]. The sensitivity of the force sensor was $128e_m$ N, where e_m is the measured strain and of a resolution of 10^{-8}. The force signal is obtained through a strain meter (National Instrument, model NI 9327). The images of the embryo under injection is captured by the digital camera positioned above the cuboid (as shown in Figure 3.7).

During the experiment, the micropipette tip was firstly positioned to slightly contacts the chorion of the embryo. After the establishment of the contact, the micro-force sensor is turned on to start measure the contact force. Subsequently,
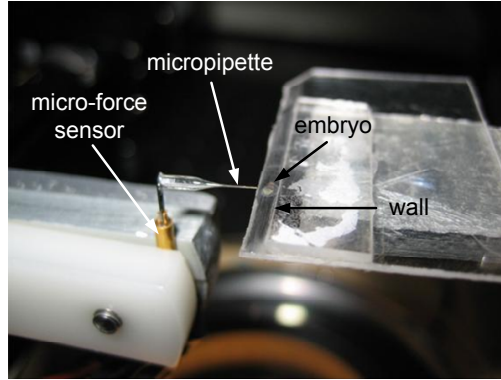
Figure 3.7: Close-up view of the contact between the micropipette and the embryo.

the micropipette was driven by the positioning stage to move at a preset constant speed until it travels a designed distance, which is considered as a single indentation step. After the indentation, the micropipette was maintained its position until the force measured stabilized. The sampling rate of the force sensor is 1 kHz, namely, for every 0.1 second, 100 force readings were recorded. The preparation of the zebrafish embryos tested was as per the standard procedures as elaborated in [15] (zebrafish embryos collected were at the state between four to six hours after fertilization).
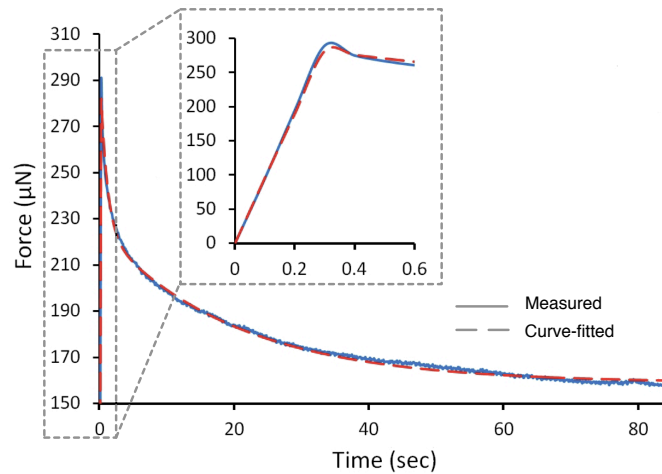
Figure 3.8: Curve fitting of data from experiment using a Maxwell-Wiechert model with two Maxwell elements.

The solid curve in Figure 3.8 shows the measured force (the solid curve) during

43

the indentation of a zebrafish embryo. (The dash curve, almost coinciding with the solid curve, represents result from the curve-fitting of the the experiment data, as discussed below.) At $t = 0$, the tip of the micropipette was in contact with the chorion and the force reading was around 0μN. A step indentation of 300μm was then applied on the embryo at a speed of 1mm/s. At $t = 0.3$s, the contact force reached a peak value of 289.53μN and then started to drop gradually. At $t = 75$s, the contact force stabilized at a magnitude of 159μN. Since the speed of the micropipette is constant during the indentation, the dynamics of the Maxwell-Wiechert model takes the specific form:

$$
f(t) \quad = \quad
\begin{cases}
k_1 v_0 t + \displaystyle\sum_{i=2}^{3} b_i (1 - e^{-\alpha_i t}) v_0, \ \text{for } t \in [0, t_0] \\
k_1 x_0 + \displaystyle\sum_{i=2}^{3} b_i (e^{\alpha_i t_0} - 1) v_0 e^{-\alpha_i t}, \ \text{for } t > t_0
\end{cases}
\tag{3.4}
$$

where $v_0 = 1$mm/s, $t_0 = 0.3$s, and $x_0 = 300\mu$m.

Fitting the measurements obtained from the experiment into Equation (3.4) using MATLAB yields the corresponding force trajectory represented by the dash curve in Figure 3.8. The average R-Square value is 0.99, indicating a high confidence level on the goodness-of-fit for this Maxwell-Weichert model.

Figure 3.9 shows the results of curve-fitting data from experiments on five embryos with different values for the maximum indentation force, while Table 3.1 lists the values of the parameters in Equation (3.4), obtained from these five experiments. It can be seen that the five sets of parameter values are comparable. The variation in some of the values across the trials are mainly due to inherent errors in the experiments and the physical characteristics of the zebrafish embryos at their individual states of development.
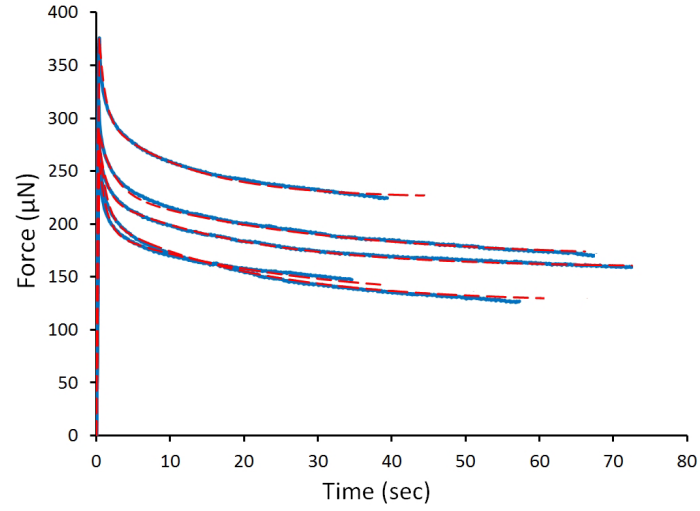
Figure 3.9: Force responses of zebrafish embryos predicted by the analytical model and measured from experiments. The smooth solid curves are generated from the model using the paramater values listed in Table 3.1. The jagged curves are obtained from experimental data.

Table 3.1: Parameter values of five indentation trials

Parameter	Trial					Avg.
	1	2	3	4	5	
k_1 (N/m)	0.43	0.53	0.42	0.56	0.75	0.538
k_2 (N/m)	0.22	0.22	0.25	0.20	0.23	0.224
k_3 (N/m)	0.21	0.22	0.26	0.21	0.25	0.230
b_1 (Ns/m)	0.22	0.22	0.25	0.40	0.20	0.258
b_2 (Ns/m)	5.2	4.4	5.2	5.9	3.0	4.74
F^* (N)	256.88	289.53	291.71	316.38	375.75	

45

Incidentally, the parameter estimation using a Maxwell-Wiechert model with *only one Maxwell element* have been tried. The result (shown in Figure 3.10) reveals the inadequacy of this model.
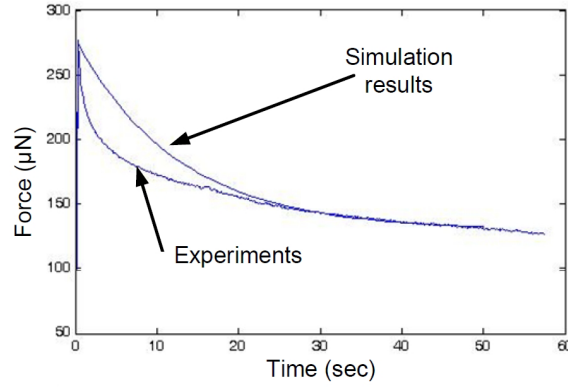
Figure 3.10: Curve-fitting of force trajectory using a Maxwell-Wiechert model with only one Maxwell element.

3.4   Speed Optimization

The objective in optimizing the speed of an automated microinjection process is to minimize the deformation of the embryo. One approach to achieve this is to design a suitable speed trajectory $v(t)$ for the motion of the micropipette. In the viscoelastic model represented by Equation (3.3), the depth of the indentation $x(t)$ is the only variable that describes the deformation of the embryo. In this context, the objective of the optimization problem is to minimize x while permitting the force sustained by the embryo to reach the required magnitude for piercing the embryo.

3.4.1 Problem Formulation

The selection of such an optimal speed is necessarily constrained in practice by the limitation of the actuation system. Such limitations typically include the maximum acceleration (denoted by A), the maximum deceleration (D), and the maximum velocity (V) of the micropipette. Consequently, there is a limit on the type of speed trajectory that can be implemented on a given actuation system.

One way to represent a general speed trajectory is to use an nth-order polynomial, i.e., $v(t) = \sum_{i=0}^{n} c_i t^i$, where the set of constants $\{c_i\}$, with $i = 1, \ldots, n$, are the coefficients that can be chosen to satisfy the constraints imposed by A, D, and V. Let Ω_v denote the set of all such trajectories implementable on a given system, i.e.,

$$
\begin{aligned}
\Omega_v \;=\; & \big\{ v(t) \,\big|\, \|v(t)\|_\infty \leq V, \\
& |dv/dt| \leq A \ \text{if} \ dv/dt > 0, \ \text{and} \\
& |dv/dt| \leq D \ \text{if} \ dv/dt < 0 \big\}
\end{aligned}
$$

where $\|v(t)\|_\infty = \max[\,|v(t)|\,]$ is the L_∞-norm of $v(t)$. For a trajectory $v(t) \in \Omega_v$, there is an instant (measured from $t = 0$ and denoted by τ^*) when the embryo is just about to be pierced. The force at τ^* is denoted by F^*.

The speed optimization problem can now be formulated as, for a given n,

$$\textit{Find:} \quad \{c_i\},\, i = 1, 2, \ldots, n$$

$$\textit{Minimizing:} \quad x(\tau^*) = \int_0^{\tau^*} v(\tau)\, d\tau, \text{ with } v(t) = \sum_{i=0}^{n} c_i t^i$$

$$\textit{Subject to:} \quad \text{1)}\ f(\tau^*) = F^*$$

$$\text{2)}\ f(t) < F^* \text{ for } t \in [0, \tau^* - \varepsilon]$$

$$\text{3)}\ v(t) \in \Omega_v \text{ for } t \in [0, \tau^*]$$

where $f(t)$ is as given in Equation (3.3), and ε is an infinitesimal positive value.

3.4.2   Numerical Solution Approach

Given τ^* and n, the optimization problem becomes linear and semi-infinite. For for a set of values of τ^* and a set of values of n, solving the corresponding linear semi-infinite optimization problems results in a set of speed trajectories and the associated minimum deformation $x(\tau^*)$. The trajectory associated with the smallest $x(\tau^*)$ is considered to be an optimal speed trajectory for the given sets of values for τ^* and n.

Limits on the values of τ^* and n can be established based on practical considerations. For τ^*, the practicality of a microinjection process requires it to have a finite upper bound, while the capability of the actuation system dictates a lower bound. Hence, τ^* can be considered to vary within a practically meaningful range. For n, the possible values can be limited to 3 or 4, since a speed trajectory in the form of such a polynomial can represent sufficiently rich dynamics for this type of manipulation tasks.

To illustrate this solution process, the results for the case where $n = 3$ and $\tau \in [0.2, 2]$ is firstly presented, with (i) the parameter values of the dynamics model being that obtained from Trial 2 as listed in Table 3.1 (since they are close

to the average), and (ii) the parameter values that characterize the performance of the actuation system as given in Table 3.2. The latter set of parameter values reflect the hardware limitation of the prototype micromanipulation system shown earlier in Figure 3.5.

Table 3.2: Parameters of the hardware

Parameter	Symbol	Value
Maximum acceleration	A	0.01 m/s²
Maximum deceleration	D	0.01 m/s²
Maximum velocity	V	0.002 m/s
Maximum force	F^*	250 μN

The optimization problem was solved using MATLAB's `linprog`. The sampling time for the semi-infinite constraints was set at $\tau^*/30$ and the increment of τ^* at 0.01 second. Figure 3.11(a) shows the minimum deformation of the embryo over the given range of values for τ^*, while Table 3.3 lists the values of the coefficients of the optimized speed trajectory $v(t)$ for a set of sample τ^* values.

Table 3.3: Coefficients of optimal speed trajectories.

τ^*	c_0	c_1	c_2	c_3
0.2	0.0004	0.0078	0.0323	-0.1590
0.4	0.0001	-0.0037	0.0335	-0.0312
0.7	0.0000	0.0003	-0.0038	0.0102
1.1	0.0000	0.0005	-0.0023	0.0027
1.4	0.0000	0.0003	-0.0011	0.0010
1.7	0.0000	0.00020	-0.00062	0.00048

Figure 3.11(a) indicates that, for the interval of τ^* between 0.2 and 2, the minimum deformation (among all the minimum in that interval) occurs when $\tau^* = 0.2$. Figure 3.11(b) and 3.11(c) show the corresponding trajectories of $v(t)$, $x(t)$ and $f(t)$, respectively.

Results from numerical simulations for the cases where $v(t)$ takes the form of
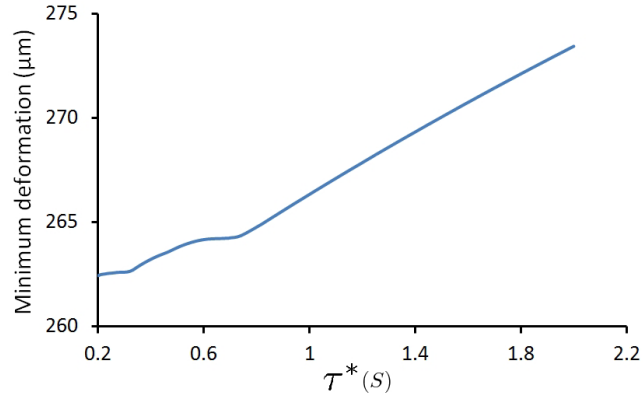
(a)
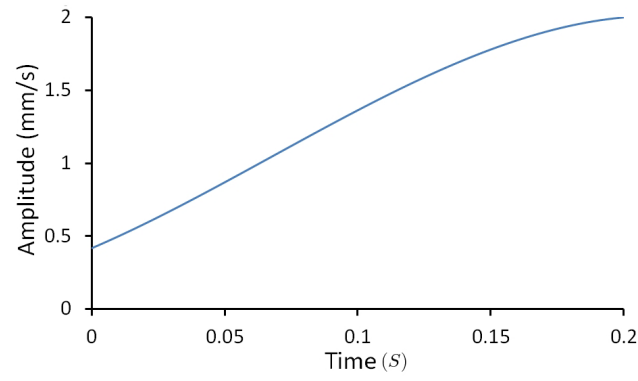
(b)
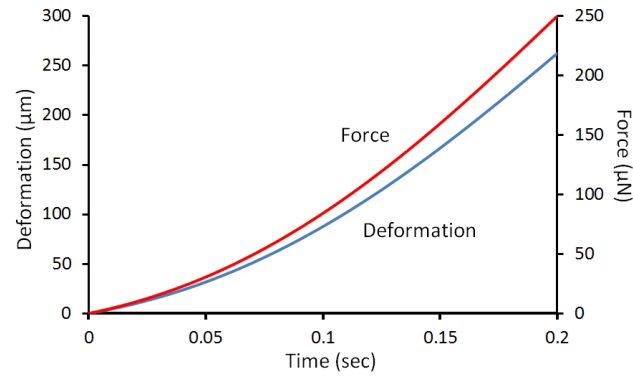
(c)

Figure 3.11: (a) Minimum deformation at different Time τ^*. (b) Trajectory of $v(t)$ for $\tau^* = 0.2s$. (c) Deformation and force for $\tau^* = 0.2$ sec.

a polynomial of 0th-, 3rd- and 4th-order are presented in Figure 3.12. The 0th-order polynomial (constant speed) corresponds to the case where the indentation is carried out at a constant speed for the same interval of τ^*. In this case the optimization problem degenerates into a simple relationship between x and τ^*, since from Equation (3.3) and with $\bar{v}$ being the constant speed, it is obtained that

$$x(\tau^*) = \bar{v}\tau^* = \frac{F^*}{k_1 + (\delta_2(\tau^*) + \delta_3(\tau^*))/\tau^*} \tag{3.5}$$

where $\delta_j(t) = b_j \left(1 - e^{-k_j\, t/b_j}\right)$, with $j = 2, 3$. Since $\dot{x} > 0$, $x(\tau^*)$ here is a monotonically increasing function of τ^*, as illustrated by the top curve in Figure 3.12.
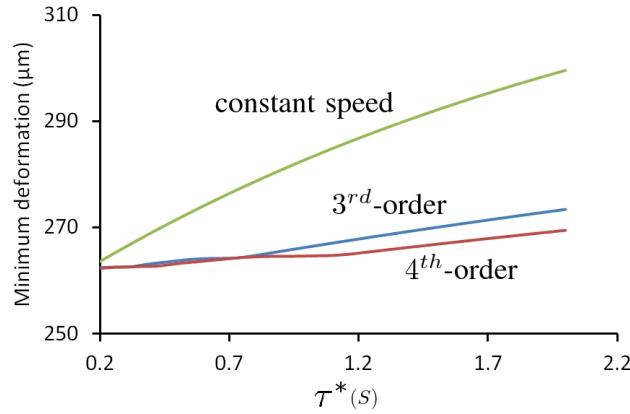
Figure 3.12: Minimum deformation with $v(t)$ of 0th, 3rd, and 4th order polynomials over an interval of τ.

The simulation results, as summarized in Figure 3.12, indicate that optimization of the sped trajectory of the micropipette leads to significantly reduction in the deformation of the embryo. Moreover, the extent of such a reduction is proportional to the time-to-piercing τ^* and also to the order of the polynomial used. However, it can be seen that the difference in $x(\tau^*)$ between the cases of 3rd and 4th-order polynomial is small (relative to that between the cases of constant speed and 3rd-order polynomial). This gives support to the consideration that a 3rd-order polynomial would be acceptable in practice.

51

3.5   Experiments

Two sets of experiments were performed. The first was to investigate the deformation of zebrafish embryo during microinjection when the indentation speed was constant. The second set was to verify and demonstrate the effectiveness of the proposed speed optimization approach for microinjection.

3.5.1   Indentation at Constant Speed

Ten embryos were indented for each of the seven constant speeds ranging from 0.05 mm/s to 1.5 mm/s. This amounts to a total of 70 measurements taken in this set of experiments. For each (constant) speed, an averaged deformation of the ten embryos was calculated.

The experimental results are shown in Figure 3.13. A comparison between the results from the simulation and the experiments is shown in Figure 3.14. These results agree with the analysis presented in the previous section, and thus confirm that a higher (constant) speed, which implies shorter time-to-piecing, results in a smaller deformation of the zebrafish embryo.
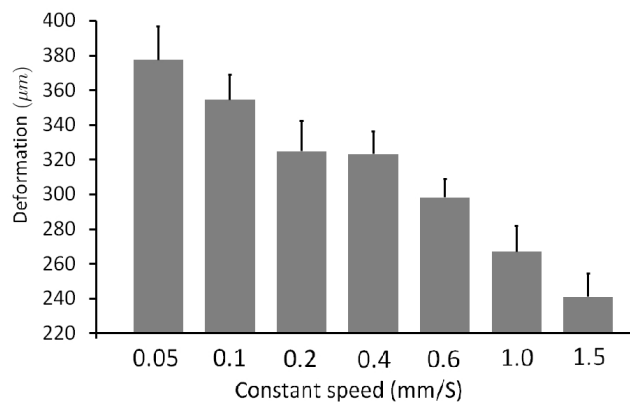
Figure 3.13: Deformation (with one standard deviation) of zebrafish embryo under indentation at constant speed.
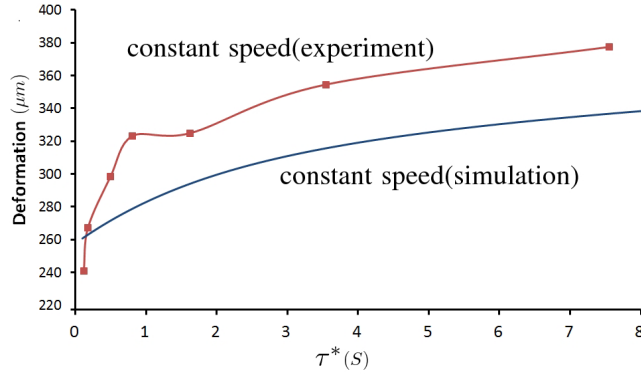
Figure 3.14: Comparison between experiment and simulation for constant speed

The difference between the experiment data and the simulation data is around 20 to 40 micro, which is around 10 percent of the overall deformation and is thus acceptable. A number of factors may contribute to the difference. The main factor is that there are errors in the parameters of the Max-well model used for simulation. These parameter errors may be due to the individual difference among different embryos and different batches of embryos (the embryos used for parameter identification and those used for experiments using constant speed are from different batches). Another key factor is that the micropipette might have slid against the membrane during the indentation process. Nonetheless, the main conclusion that can be drawn from the comparison between the experiment and simulation results is that the data trends are consistent.

3.5.2 Indentation at Optimized Speed

The numerical solution presented in Section III assumes (i) the existence of an accurate model of embryo deformation, and (ii) precise implementation of the desired speed trajectory. In practice, a microinjection system is unlikely to be able to satisfy these assumptions. This leads to the problem of how to verify (in an actual microinjection process) the effectiveness of the optimal speed trajec-

tory that has been analytically designed to minimize embryo deformation. This section describes our approach, and presents experimental results, for demonstrating the effectiveness of speed optimization under the inherent constraints in a practical microinjection system.

An immediate consequence of having modeling errors and imprecise speed control in a practical microinjection system is that the force applied on the embryo may not reach the prescribed peak F^* at exactly the prescribed instant τ^* (as required by the analysis). Since reaching F^* is the essential goal of microinjection, the optimized speed trajectory $v(t)$ is altered to obtain the *modified* optimal speed trajectory $v_e(t)$, by relaxing the requirement on the time for the force to reaches F^* as follows:

$$
v_e(t) = \left\{ \begin{array}{ll} v(t) & \text{for } 0 \leq t \leq \tau^* \\ v(\tau^*) & \text{otherwise} \end{array} \right.
\tag{3.6}
$$

Under this modification, the indentation process may stop prior to, or beyond, τ^*. The actual stopping time (denoted by τ_e) is the instant when the applied force reaches F^*.
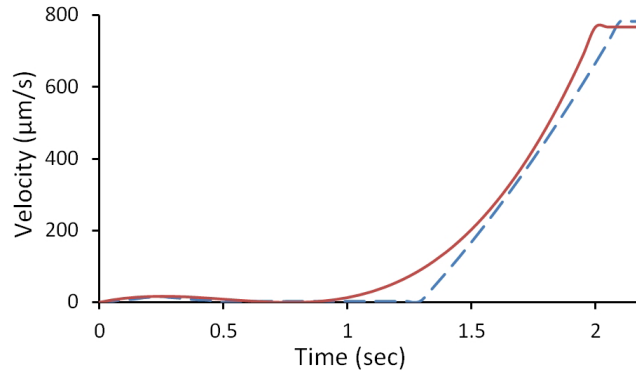
Figure 3.15: Optimized speed trajectory and its approximate implementation.

A set of modified optimal speed trajectories associated with $\tau^* \in \{0.3, 0.5, 1, 2, 3, 4\}$, were generated based on a 3th-order polynomial and using the parameter values

54

of the dynamics model obtained from Trial 2 (as listed in Table 3.1) and the parameter values listed in Table 3.2. Due to the limitation of the current micro-manipulation platform, which only permits the specification of point-to-point motion in terms of a trapezoidal speed profile (defined by the desired position, the acceleration and deceleration, and the maximum velocity), this set of speed trajectories were implemented by constructing a sequence of such speed profiles to approximate the analytical forms. Figure 3.15 illustrates an example of such approximate implementation. It shows the (theoretical) optimized speed trajectory and the actual speed trajectory obtained from the approximate implementation for the case of $\tau^* = 2$. The approximated implementation was done using three consecutive trapezoidal speed profiles of point-to-point motion. The intervals for these three profiles are: $[0, 0.5]$, $[0.5, 1.2]$, and $[1.2, 2]$, with the corresponding values for the desired position, the acceleration (which is also the deceleration), and the maximum velocity being set as $\{0.0043, 0.068, 0.017\}$, $\{0.002, 0.1, 0.003\}$, and $\{0.7, 0.9581, 0.7665\}$, respectively.
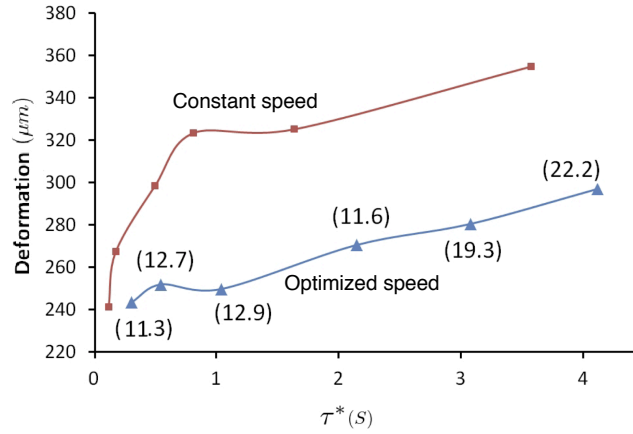
Figure 3.16: Deformation of zebrafish embryos obtained from experiments. The top curve is the same as that shown earlier in Figure 3.14 for the period of $[0, 4]$ seconds. In the bottom curve, each triangle represents the average value from 10 trials, with the number in brackets being the standard deviation.

A group of ten trials for each of the six optimized speed trajectories (i.e., one group for each value of τ^*) were carried out. This amounts to a total of 60

measurements taken in this set of experiments. For each group, an averaged deformation of the ten embryos was calculated. Figure 3.16 shows the results, with the results from the constant-speed experiments shown earlier in Figure 3.13 included for comparison. This set of experimental results clearly demonstrate that a suitably designed dynamical (as opposed to constant) speed trajectory can significantly improve the performance of microinjection of zebrafish embryos in terms of minimizing the deformation sustained by the embryos.

3.6 Conclusions

The problem of optimizing the microinjection of zebrafish embryos in terms of minimizing the deformation sustained by the embryo during the indentation process, has been investigated. This problem is formulated as one of optimizing the speed trajectory of the micropipette, and proposed a systematic approach for solving this problem by synthesizing an optimal speed trajectory, based on a dynamics model of the zebrafish embryo and a class of polynomials. Numerical simulations and extensive experiments have been conducted to demonstrate the effectiveness of the proposed approach. In particular, the statistically meaningful experimental data (generated using a large sample of zebrafish embryos) provide direct evidence on the advantage of speed optimization in a microinjection process.

Chapter 4

Force Control of a Cellular Tensegrity Structure with Model Uncertainties and Partial State Measurability

4.1 Introduction

Studies on how cells respond to mechanical forces have generated strong evidence in support of the view that such forces play an important role in the regulation of cellular functions [1]. Novel approaches and technologies for mechanobiology have been developed to enable quantitative investigation of mechanical forces sustained by cells at cellular and subcellular levels [21]. These studies mainly focused on exploring hardware platforms that integrate application and measurement of mechanical loads on cells. Such micro-engineering platforms provide a necessary means to support further development of approaches and algorithms for precisely applying external mechanical forces on

57

living cells, with the aim of revealing the relationship between external mechanical stimulus and cellular response.

To realize the full potential of such platforms for mechanobiology requires the integration therein of sophisticated force control techniques in order to achieve accurate control of dynamical forces at micro/nano-scale in the manipulation of biological systems. This necessitates the modeling of the mechanical behavior of cells under external force. Approaches based on continuum and structural mechanics have been shown to be useful in constructing mechanical models of living cells. The tensegrity model of cell deformability offers a potentially more effective alternative, because it is capable of simulating many aspects of cell mechanical behavior and providing biologically plausible explanations for such behavior [42].

In the context of force-control tasks involving a robotic manipulator, the cell (on which a force is applied) represents the environment in the execution of such a task [11][13]. The linear-spring model with constant spring stiffness and the Kelvin-Voigt spring-damper model are often used for constructing a dynamics model of such an environment [32]. Although adequate for simple mechanical environment usually encountered in conventional robotic manipulation tasks, these models fall short of being able to capture the rich dynamics exhibited by living biological cells. Consequently, force control techniques for cell manipulation developed based on such models are usually constrained by the limitation of these models.

This chapter presents the development of a robust force control algorithm that enables accurate application of an external force on a dynamics model of biological cells. Such force control is achieved by utilizing a six-strut cellular tensegrity model constructed based on the structural approach. Leveraging on the more comprehensive description of the nonlinearity and dynamic coupling
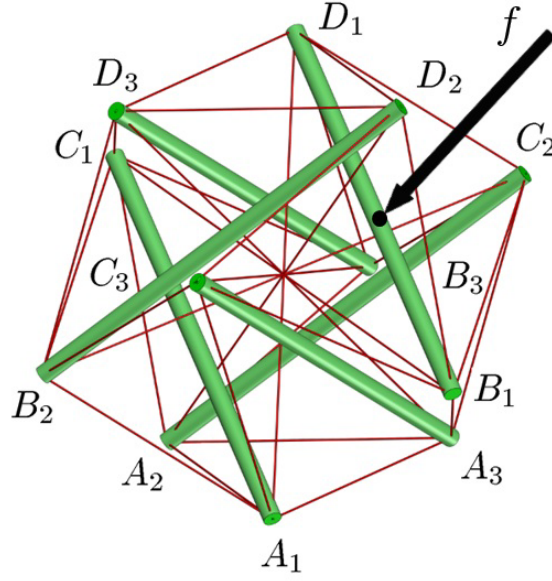
Figure 4.1: A spherical tensegrity structure with intermediate filaments used to generate the computational tensegrity model.

of internal structural elements provided by this tensegrity model, this chapter presents the synthesization of a novel robust control law that can effectively deal with model uncertainties and partial state measurability.

4.2 Cellular Tensegrity Model and Task Setting

This section briefly introduces a well accepted six-strut cellular tensegrity model (as shown in Figure 4.1) which is explained in detail in Section 2.3. The equations of motion of cellular tensegrity model for the case of being applied a force on one of its struts is derived based on the results in [47], which is reviewed in Section 2.3.1.

4.2.1 Equations of Motion Under External force

Figure 4.1 illustrates the structure of a spherical tensegrity structure with intermediate filaments, where the points A_1, A_2, and A_3 define the plane on which they are fixed, with C_iA_i freely rotatable about A_i. The struts are considered as rigid bars of identical length L under compression, whereas the tendons as identical viscoelastic Voigt elements.

For the homogeneous tensegrity model, the constitutive equation of a tendon is

$$f_{ti} = k\left(l_i/l_{i0} - 1\right) + c\,\dot{l}_i \tag{4.1}$$

where f_{ti} is the force sustained by the ith tendon, k is the constant stiffness, $c > 0$ is the constant damping coefficient, l_i and l_{i0} are the length and the initial length of the tendon, respectively, and $\dot{l}_i$ is the time derivative of l_i.

The equations of motion of the tensegrity structure are:

$$A(q)T(q) + C(q)\dot{q} + H(q)f = 0 \tag{4.2}$$

Since the inertial effect of the tensegrity structure is negligible relative to the overall system dynamics, they are neglected in this model [46].

Equation (4.2) will take on specific forms depending on the location on the structure where external forces and moments are applied. Since A_i ($i = 1, 2, 3$) are fixed, only the struts B_iD_i exhibit full degree-of-freedom in their motion. Applying f on one of these struts will excite the dynamics of the tensegrity structure more extensively. Let $f = [f_x \ f_y \ f_z]^T \in \mathbb{R}^{3\times1}$ be applied on B_1D_1 at a point G as shown in Figure 4.1 and Figure 4.2. The strut B_1D_1 is specified here simply for clarity of expression in the subsequent analysis, which is readily applicable to other cases where f is applied on any one of the other struts.

60
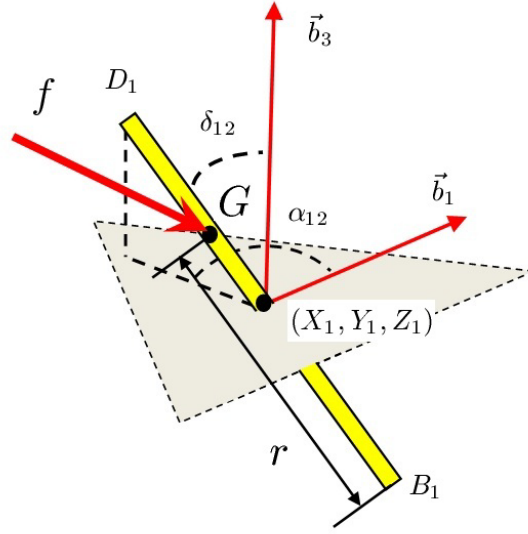
Figure 4.2: Characterization of $B_1 D_1$ with external force applied on point G, where $0 \leq r \leq L$, with L being the length of $B_1 D_1$. $\alpha_{12}, \delta_{12}, X_1, Y_1, Z_1$ are of the same definitions as in Section 2.3.1.

The generalized coordinates q is redefined to facilitate subsequent development. As is shown in Figure 4.2, $B_1 D_1$ is described by α_{12}, δ_{12} and q_1, where α_{12} and δ_{12} are of the same definition as in Section 2.3.1, while q_1 is the Cartesian coordinates of point G. This differs from the original definition in Section 2.3.1, since the Cartesian coordinates of G, instead of the center of mass of strut $B_1 D_1$, are employed. For struts $B_i D_i$ $(i = 2, 3)$ and $A_j C_j$ $(j = 1, 2, 3)$, the massless point at the center of the structure are described by the same independent coordinates as in Section 2.3.1.

Vector q is partitioned into q_1 and q_2 in the form (which is referred to as q_f):

$$q_f = \begin{bmatrix} q_1 \\ q_2 \end{bmatrix} \tag{4.3}$$

where, $q_1 \in \mathbb{R}^{3 \times 1}$ is the Cartesian coordinates of G; $q_2 \in \mathbb{R}^{21 \times 1}$, which denotes

the rest of the elements of q which are not redefined, is given as:

$$
\begin{aligned}
q_2 &= [\delta_{11}\ \alpha_{11}\ \delta_{21}\ \alpha_{21}\ \delta_{31}\ \alpha_{31}\ \delta_{12}\ \alpha_{12}\ X_2\ Y_2 \\
&\quad Z_2\ \delta_{22}\ \alpha_{22}\ X_3\ Y_3\ Z_3\ \delta_{32}\ \alpha_{32}\ X\ Y\ Z]^T
\end{aligned}
$$

The equations of motion are derived in a similar way as described in [47] to yield

$$
A_f(q_f)T_f(q_f) + C_f(q_f)\dot{q}_f = \begin{bmatrix} f \\ 0 \end{bmatrix} \tag{4.4}
$$

where, A_f, T_f, C_f are the corresponding matrix function or vector function of A, T and C in Equation (4.2) in terms of q_f, respectively. The resultant matrix functions A_f, T_f and C_f share similar forms (shown in Appendix B) as discussed in [47]. Moreover, $T_f(q_f)$ and $C_f(q_f)$ are linearly proportional to the tendon stiffness k and the tendon damping coefficient c, respectively.

Let

$$
C_f = \begin{bmatrix} c \cdot C_{11} & c \cdot C_{12} \\ c \cdot C_{21} & c \cdot C_{22} \end{bmatrix}, \quad A_f T_f = \begin{bmatrix} k \cdot K_1 \\ k \cdot K_2 \end{bmatrix}
$$

with $C_{11} \in \mathbb{R}^{3\times3}$, $C_{12} \in \mathbb{R}^{3\times21}$, $M_{21} \in \mathbb{R}^{21\times3}$, $M_{22} \in \mathbb{R}^{21\times21}$, $K_1 \in \mathbb{R}^{3\times1}$, and $K_2 \in \mathbb{R}^{21\times1}$ are known function matrixes or function vectors, which are independent of c and k. Then Equation (4.4) can be rewritten as

$$
k \cdot K_1(q_1, q_2) + c \cdot C_{11}(q_1, q_2)\dot{q}_1 + c \cdot C_{12}(q_1, q_2)\dot{q}_2 = f \tag{4.5}
$$

$$
k \cdot K_2(q_1, q_2) + c \cdot C_{21}(q_1, q_2)\dot{q}_1 + c \cdot C_{22}(q_1, q_2)\dot{q}_2 = 0 \tag{4.6}
$$

The reference solution presented in [47] is adopted as the initial states of $q_f = [q_1^T,\ q_2^T]^T$, which are denoted as $q_{fr} = [q_{1r}^T,\ q_{2r}^T]^T$. The form of q_{fr} is presented in Appendix C.

The rewritten equations of motion represent a relatively general case of biomanipulation tasks involving applying and controlling force on living cells or other similar biological materials. For instance, cell microinjection, as a prevalent biomanipulation operation, can be considered as a specific case of the discussed situation by assuming that all of the upper three struts ($B_i D_i$ ($i = 1, 2, 3$)) are applied equivalent vertical force while A_1, A_2 and A_3 are fixed. In this case, the equations of motion are of the similar form as (4.5) and (4.6) but with reduced degree-of-freedoms.

4.2.2 Force-bearing Interaction, Parameter Uncertainties, and State Measurability

The external force f is considered being applied on the tensegrity structure by a manipulator whose dynamics is known and described (in the Cartesian space) by

$$H_r(x)\,\ddot{x} + C_r(x, \dot{x})\,\dot{x} + g_r(x) = u - f \tag{4.7}$$

where, $x, \dot{x}, \ddot{x} \in \mathbb{R}^3$ are the position, velocity, and acceleration of the links of the manipulator, respectively, $H_r(x) \in \mathbb{R}^{3\times3}$ is the inertia matrix, $C_r(x, \dot{x}) \in \mathbb{R}^{3\times3}$ represents the Centripetal-Coriolis effects, $g_r(x) \in \mathbb{R}^3$ represents conservative forces (e.g., gravity), and $u \in \mathbb{R}^3$ is the control input. Under the condition that the end-effector of the manipulator remains in contact with the tensegrity structure at the point G (thus taking $x = q_1$), Equation (4.7) becomes

$$H_r(q_1)\,\ddot{q}_1 + C_r(q_1, \dot{q}_1)\,\dot{q}_1 + g_r(q_1) = u - f \tag{4.8}$$

The uncertainty in the parameters that characterize the mechanical properties of the tensegrity model is considered. These parameters are the stiffness k and the damping coefficient c of the struts. The estimates of these two parameters

63

are denoted by $\hat{k}$ and $\hat{c}$ respectively. Another issue need to be addressed is state measurability. Since the external force is considered to be applied on the tensegrity structure by point contact (i.e., at the point G as illustrated in Figure 4.2), it is reasonable to expect that, for the state of the overall system, only q_1 and $\dot{q}_1$ are measurable with suitable instrumentation of the manipulation system. However, q_2 and $\dot{q}_2$ can be estimated from Equation (4.6) as

$$\dot{q}_2 = C_{22}^{-1}(q_1, q_2)\left[-k \cdot K_2(q_1, q_2)/c - C_{21}(q_1, q_2)\dot{q}_1\right] \tag{4.9}$$

$$q_2 = q_{2r} + \int_0^t \dot{q}_2 \, d\tau \tag{4.10}$$

under the condition that C_{22} is nonsingular during the process when the tensegrity structure sustains the applied external force.

Now from Equations (4.5) and (4.6), it is obtained

$$f = \Psi(q_1, q_2, c)\, \dot{q}_1 + \Phi(q_1, q_2, k) \tag{4.11}$$

where $\Psi(q_1, q_2, c) \triangleq c \cdot (C_{11} - C_{12}C_{22}^{-1}C_{21})$ and $\Phi(q_1, q_2, k) \triangleq k \cdot (K_1 - C_{12}C_{22}^{-1}K_2)$. Further, the derivative of contact force is obtained as:

$$\dot{f} = \Psi(q_1, q_2, c)\ddot{q}_1 + \varpi(\dot{q}_1, q_1, q_2, c, k) \tag{4.12}$$

where $\varpi(\dot{q}_1, q_1, q_2, c, k) \triangleq \dot{\Psi}(q_1, q_2, \dot{q}_1, \dot{q}_2, c)\dot{q}_1 + \dot{\Phi}(q_1, q_2, \dot{q}_1, \dot{q}_2, c, k)$.

Since the expression $\Psi(\cdot)$ defined above is a function of c, it can be further expressed (to account for the uncertainty in c) as

$$\Psi(q_1, q_2, c) \;=\; (I + \varepsilon_\Psi)\Psi(q_1, \hat{q}_2, \hat{c})$$

where $\varepsilon_\Psi \in \mathbb{R}^{3\times 3}$ is the parametric uncertainty matrixes. The entries for matrix ε_Ψ are denoted as $\varepsilon_{\Psi ij}$. Similarly, the error in ϖ (due to the uncertainties) can

be expressed as

$$\mu \triangleq \varpi(\dot{q}_1, q_1, q_2, c, k) - \varpi(\dot{q}_1, q_1, \hat{q}_2, \hat{c}, \hat{k}).$$

4.2.3   Control Objective

The control objective is to design control law u for the three degree-of-freedom manipulator as described in (4.8) so that interaction force (between the end-effector and cellular tensegrity structure) as described in (4.11) follows the desired force trajectory f_d (generated from $\dot{f}_d$) in presence of uncertainties due to unknown mechanical properties and partial state measurability. The uncertainties and estimations of the contact dynamics considered satisfy the following assumptions:

Assumption 4.1: The matrix $\Psi(q_1, \hat{q}_2, \hat{c})$ is invertible.

Assumption 4.2: There exists a positive constant $0 \leq \zeta < 1$ such that

$$\max_i \sum_{j=1}^{3} |\varepsilon_{\Psi ij}| \leq \zeta, \ \ i = 1, 2, 3.$$

Assumption 4.3: There exists a function $\overline{\mu}(q_1, \dot{q}_1, \hat{q}_2, \hat{c}, \hat{k}) \geq 0$ such that

$$\overline{\mu}(q_1, \dot{q}_1, \hat{q}_2, \hat{c}, \hat{k}) \geq \left| \mu(q_1, \dot{q}_1, q_2, \hat{q}_2, c, k, \hat{c}, \hat{k}) \right|$$

The above assumptions are common in the literature of robust control of multi-input-multi-output control systems[54]. As indicated by (4.11), the contact force model is nonlinear and coupled and thus more convoluted compared to the spring or spring-damper model discussed in the literature. The model uncertainties and partial state measurability further complicates the control problem. To address these difficulties, a robust control law is proposed while consider-

65

ing accommodating the uncertainties due to unknown mechanical property (as estimated by $\hat{c}$ and $\hat{k}$) and partial measurability (as estimated by $\hat{q}_2$).

4.3 Notations

In the sequel, $\lambda_{\max}(A)$ and $\lambda_{\min}(A)$ denote the maximum and minimum eigenvalues of a square matrix A, respectively. $\|A\|_I$ refers to the induced norm of any matrix A. $\|B\|$ refers to the Euclidean norm of any vector B.

4.4 Force Control Development

In this section, a robust force controller is developed via the backstepping method.

4.4.1 Synthesis of Control Law

A vector $r_f \in \mathbb{R}^3$ incorporated with an integral force feedback term is introduced [82]

$$r_f = e_f + K_1 I_f \tag{4.13}$$

where $e_f \triangleq f - f_d \in \mathbb{R}^3$ is the force tracking error, K_1 is a semi-positive definite matrix, and I_f is defined as

$$I_f = -K_1^{-1} e_f(0) + \int_0^t e_f(\tau) d\tau$$

Obviously, $r_f(0) = 0$. Note that

$$\dot{r}_f = \dot{f} - \epsilon \tag{4.14}$$

66

with $\epsilon \triangleq \dot{f}_d - K_1 e_f$.

The control law is proposed as:

$$u(q_1, \dot{q}_1, \hat{q}_2, f, \epsilon, r_f) = H_r(q_1)\hat{\Psi}^{-1}(q_1, \hat{q}_2)(u_a + u_r) + f + C_r\dot{q}_1 + g_r \quad (4.15)$$

where

$$u_a(q_1, \dot{q}_1, \hat{q}_2, f, \epsilon, r_f) = -K_f r_f - \hat{\varpi}(\dot{q}_1, q_1, \hat{q}_2) + \epsilon \quad (4.16)$$

with K_f being a positive definite matrix, and $u_r \in \mathbb{R}^3$ a robust control term designed as follows:

$$u_r = \begin{cases} -K_r r_f & \text{if } \|r_f\| \leq \sigma_h & (4.17\text{a}) \\ -(1-\beta) \cdot K_r r_f - \beta \cdot \dfrac{h}{1-\zeta} \cdot \dfrac{r_f}{\|r_f\|} & \\ & \text{if } \sigma_h \leq \|r_f\| \leq (1+\alpha_2)\sigma_h & (4.17\text{b}) \\ -\dfrac{h}{1-\zeta}\dfrac{r_f}{\|r_f\|} & \text{if } \|r_f\| \geq (1+\alpha_2)\sigma_h & (4.17\text{c}) \end{cases}$$

where, K_r is any s.p.d. matrix; $\sigma_h \triangleq \sigma(t)/(h+\alpha_1)$ with $\sigma(t)$ any bounded time-varying positive scalar (i.e., $0 \leq \sigma(t) \leq \sigma_{max}$) and α_1 any positive constant; $\beta \triangleq (\|r_f\| - \sigma_h)/\alpha_2\sigma_h$ with α_2 any positive constant; h is any bounded function satisfying:

$$h \geq \max \begin{cases} \|\varepsilon_\Psi u_a + \mu(q_1, \dot{q}_1, \hat{q}_2) - \varepsilon_\Psi K_r r_f\|, \\ \|\varepsilon_\Psi u_a + \mu(q_1, \dot{q}_1, \hat{q}_2) - (1-c)\varepsilon_\Psi K_r r_f\|, \\ \|\varepsilon_\Psi u_a + \mu(q_1, \dot{q}_1, \hat{q}_2)\| \end{cases} \quad (4.18)$$

With Assumption 4.2 and 4.3, a natural candidate of h is:

$$h = \sqrt{3}\zeta\|u_a\| + \overline{\mu} + \sqrt{3}\zeta\gamma_0\|r_f\| \quad (4.19)$$

67

where $\gamma_0 = \lambda_{max}(K_r)$.

Remark 4.1: The robust control law (4.17) has similar form as the Smoothing Method II proposed in [83] while the condition of function h, which characterizes the bounds of the uncertainties of the system, is modified accordingly to cope with the presence of the uncertainties in the control coefficient matrix (defined by ε_Ψ). Compared to the robust control term proposed in [54] using the sgn($\cdot$) function, the control law (4.17) is smooth and has the virtue of reducing control chattering when the system is around the sliding mode (i.e., $\|r_f\| = 0$).

4.4.2 Stability Analysis

Theorem 4.1: Consider the manipulator described by (4.8) interacts with the cellular tensegrity model described by (4.5) and (4.6). Provided that Assumptions 4.1-4.3 are satisfied, the proposed control law (4.15) ensures that the force tracking error $e_f(t)$ is uniformly ultimately bounded in the sense that

$$\|e_f(t)\| \leq \varepsilon_0 \exp(-\varepsilon_1 t) + \varepsilon_2 \tag{4.20}$$

where ε_0, ε_1, and ε_2 are positive constants.

Proof: From Equation (4.13), it yields

$$\|e_f\| = \|r_f - K_1 I_f\| \leq \|r_f\| + \|K_1\|_I \cdot \|I_f\| \tag{4.21}$$

The establishment of the upper bounds for $\|r_f\|$ and $\|I_f\|$ is then presented.

Choose the Lyapunov function: $V = \frac{1}{2} r_f^T r_f \in \mathbb{R}$. Utilizing Equations (4.14), (4.12), (4.8), (4.15), (4.16), and (4.17) in that order, it can be derived that the

time derivative of V as follows:

$$
\begin{aligned}
\dot{V} &= r_f^T \dot{r}_f = r_f^T \left(\dot{f} - \epsilon \right) \quad \text{(using Eq. (4.14))} \\
&= r_f^T \left[\Psi(q_1, q_2) \ddot{q}_1 + \varpi(\dot{q}_1, q_1, q_2) - \epsilon \right] \\
&= r_f^T [\Psi(q_1, q_2) H_r^{-1}(q_1)(u - f - C_r(q_1, \dot{q}_1)\dot{q}_1 - g_r(q_1)) + \varpi(\dot{q}_1, q_1, q_2) - \epsilon] \\
&= r_f^T [\Psi \hat{\Psi}^{-1}(u_a + u_r) + \varpi - \epsilon] \\
&= r_f^T [u_a + \varpi - \epsilon + (I + \varepsilon_\Psi)u_r + \varepsilon_\Psi u_a] \\
&= -r_f^T K_f r_f + r_f^T [(I + \varepsilon_\Psi)u_r + \varepsilon_\Psi u_a + \mu] \\
&= -r_f^T K_f r_f + M \quad\quad\quad\quad\quad\quad\quad\quad\quad\quad (4.22)
\end{aligned}
$$

where $M \triangleq r_f^T[(I + \varepsilon_\Psi)u_r + \varepsilon_\Psi u_a + \mu]$. The following shows that the control law (4.17) ensures that

$$
M \leq \varepsilon(t), \quad \text{with} \quad \varepsilon(t) \triangleq (1 + \alpha_2)\sigma(t) \quad\quad\quad (4.23)
$$

for all $\|r_f\|$.

Case 1: $\|r_f\| \leq \sigma_h$.

Noting (4.17a) (4.18), it is obtained that

$$
\begin{aligned}
M &= -r_f^T K_r r_f + r_f^T(-\varepsilon_\Psi K_r r_f + \varepsilon_\Psi u_a + \mu) \\
&\leq r_f^T(-\varepsilon_\Psi K_r r_f + \varepsilon_\Psi u_a + \mu) \\
&\leq \|r_f\| \| - \varepsilon_\Psi K_r r_f + \varepsilon_\Psi u_a + \mu \| \\
&\leq h\|r_f\| \leq h \cdot \sigma_h = h \cdot \frac{\sigma(t)}{h + \alpha_1} \\
&\leq \sigma(t) \leq \varepsilon(t) \quad\quad\quad\quad\quad\quad\quad\quad (4.24)
\end{aligned}
$$

Case 2: $\|r_f\| \geq (1 + \alpha_2)\sigma_h$.

69

With Assumption 4.2, it is notice that

$$\left| r^T \varepsilon_\Psi \frac{r_f}{\|r_f\|} \right| \leq |r^T \varepsilon_\Psi sgn(r_f)| \leq \zeta \|r_f\| \qquad (4.25)$$

Hence, with (4.17c) (4.18), it yields

$$
\begin{aligned}
M &= r_f^T u_r + r_f^T \varepsilon_\Psi u_r + r_f^T (\varepsilon_\Psi u_a + \mu) \\
&= -\frac{h}{1-\zeta}(r_f^T \frac{r_f}{\|r_f\|} + r^T \varepsilon_\Psi \frac{r_f}{\|r_f\|}) + r_f^T(\varepsilon_\Psi u_a + \mu) \quad \text{(using Eq. (4.17c))} \\
&\leq -\frac{h}{1-\zeta}(\|r_f\| - \zeta\|r_f\|) + r_f^T(\varepsilon_\Psi u_a + \mu) \quad \text{(using Eq. (4.25))} \\
&= -h\|r_f\| + r_f^T(\varepsilon_\Psi u_a + \mu) \\
&\leq -h\|r_f\| + \|r_f\|\|\varepsilon_\Psi u_a + \mu\| \\
&\leq 0 \quad \text{(using Eq. (4.18))} \\
&\leq \varepsilon(t) \qquad\qquad\qquad\qquad\qquad\qquad\qquad\qquad (4.26)
\end{aligned}
$$

Case 3: $\sigma_h \leq \|r_f\| \leq (1 + \alpha_2)\sigma_h$.

With the proof in Case 1 and Case 2, it is easy to verify that under the control law (4.17c) and (4.18)

$$
\begin{aligned}
M &\leq -\beta h\|r_f\| + h\|r_f\| \leq h\|r_f\| \\
&\leq (1 + \alpha_2)h \cdot \sigma_h \leq (1 + \alpha_2)\sigma(t) \\
&= \varepsilon(t) \qquad\qquad\qquad\qquad\qquad\qquad (4.27)
\end{aligned}
$$

Hence, $M \leq \varepsilon(t)$ holds for all $\|r_f\|$.

Consequently,

$$\dot{V} \leq -r_f^T K_f r_f + \varepsilon(t) \leq -2\gamma_1 V(t) + \varepsilon(t) \qquad (4.28)$$

70

where $\gamma_1 = \lambda_{\min}(K_f)$ and $\varepsilon(t)$ is as given in Equation (4.23). Solving the linear differential inequality (4.28) yields

$$V(t) \le V(0)e^{-2\gamma_1 t} + \int_0^t e^{-2\gamma_1(t-\tau)}\varepsilon(\tau)d\tau \tag{4.29}$$

Since $\varepsilon(t) \ge 0$ and let $\varepsilon_{\max} \triangleq (1/\gamma_1)\sup_{\tau \in [0,t]}[\varepsilon(t)]$, it is obtained that

$$V(t) \le V(0)e^{-2\gamma_1 t} + \varepsilon_{\max} \tag{4.30}$$

By definition of V and with $r_f(0) = 0$, it follows

$$\|r_f\|^2 \le \|r_f(0)\|^2 e^{-2\gamma_1 t} + \varepsilon_{\max} = \varepsilon_{\max} \tag{4.31}$$

Thus,

$$\|r_f\| \le \sqrt{\varepsilon_{\max}} \tag{4.32}$$

Subsequently, the establishment of the upper bound for $\|I_f\|$ is presented. Multiplying both sides of Equation (4.13) by $e^{K_1 t}$ and noting that $e_f(t) = \dot{I}_f(t)$, $e^{K_1 t} K_1 = K_1 e^{K_1 t}$, and $de^{K_1 t}/dt = K_1 e^{K_1 t}$, it follows

$$e^{K_1 t} r_f(t) = \frac{d}{dt}\left(e^{K_1 t} I_f(t)\right) \tag{4.33}$$

Integrating it over $[0, t]$, it yields that

$$I_f(t) = e^{-K_1 t} I_f(0) + e^{-K_1 t} \int_0^t e^{K_1 \tau} r_f(\tau)d\tau \tag{4.34}$$

Thus,

$$\|I_f\| \le \|I_f(0)\|e^{-\gamma_2 t} + (1 - e^{-\gamma_3 t})\sqrt{\varepsilon_{\max}} \tag{4.35}$$

where $\gamma_2 = \lambda_{\min}(K_1)$ and $\gamma_3 = \lambda_{\max}(K_1)$.

Finally, substituting Equations (4.32) and (4.35) into Equation (4.21) yields the expression for the upper bound on $\|e_f\|$, i.e.,

$$\begin{aligned}
\|e_f\| &\leq \gamma_3\|I_f(0)\|e^{-\gamma_2 t} + (1 + \gamma_3 - \gamma_3 e^{-\gamma_3 t})\sqrt{\varepsilon_{\max}} \\
&\leq \gamma_3\|I_f(0)\|e^{-\gamma_2 t} + (1 + \gamma_3)\sqrt{\varepsilon_{\max}}
\end{aligned} \tag{4.36}$$

Noting that $0 \leq \sigma(t) \leq \sigma_{\max}$, it is obtained that have

$$\sqrt{\varepsilon_{\max}} \leq \varrho, \quad \varrho \triangleq \sqrt{\frac{(1 + \alpha_2)}{\gamma_1}\sigma_{\max}} \tag{4.37}$$

From Equation (4.36) it can be concluded that given any $\varrho^* > (1 + \gamma_3)\varrho$, there exists T^* such that for any $t > T^*$, $\|e_f(t)\| \leq \varrho^*$. Therefore, e_f is uniformly ultimately bounded and exponentially converges to $(1 + \gamma_3)\varrho$. $\square$

4.5   Numerical Simulation

Numerical simulations are conducted to demonstrate the effectiveness of the proposed force control law.
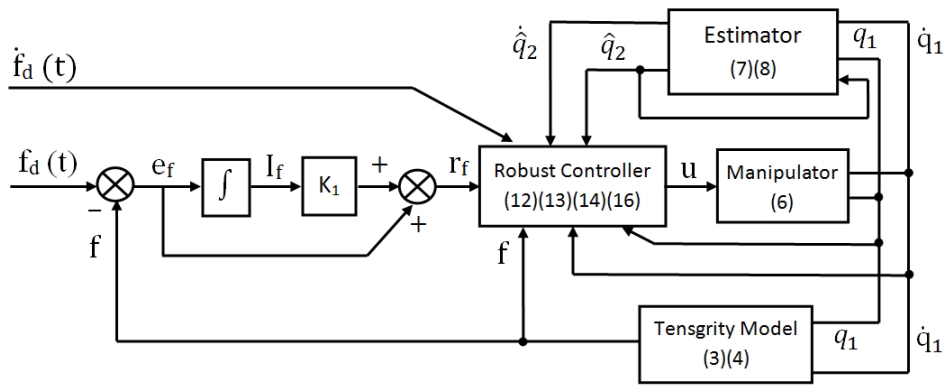
Figure 4.3: Schematics of proposed robust controller.

Figure 4.3 shows a schematic diagram of the control system. In the simulations,

two types of typical force trajectories are used: a step $f_{1d} = [20 \; 20 \; f_{1dZ}]^T$ (pN), and a sinusoid $f_{2d} = [0 \; 0 \; f_{2dZ}]^T$ (pN), where, $f_{1dZ} = -40$ and $f_{2dZ} = -25 - 15 * \sin \pi t / 4$, as shown in Figure 4.4. The initial states (i.e., q_{1r} and q_{2r}) of the tensegrity model in the absence of external force are presented in Appendix C. Furthermore, it is assumed that $\dot{q}_{fr} = \ddot{q}_{fr} = 0$.
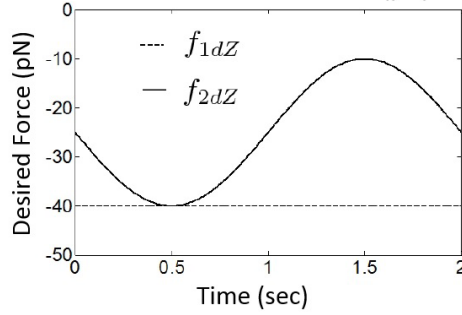
Figure 4.4: Trajectories of the two types of desired force used in the simulations.

The prestress P (as reviewed in Section 2.3.2), which characterizes the spherical prestressable configuration, is assumed to be 2. The other parameter values used in the simulations are listed in Table 4.1, with $K_1 = \mathrm{diag}(10)$, $K_f = \mathrm{diag}(2)$, and K_r as an identity matrix.

Table 4.1: Values of parameters used in simulation.

L (μm)	k (pN)	c (pN s/μm)	$\hat{k}$ (pN)	$\hat{c}$ (pN s/μm)
10	100	100	120	80

ζ	μ	α_1	α_2	σ
0.5	4ϖ	0.5	0.5	16×10^{-24}

In both simulations, Assumptions 4.1-4.3 have been found to be satisfied and the results are of satisfying agreement with analysis.

The simulation results are presented in Figure 4.5 and Figure 4.6. It can be seen that the force control law was effective in ensuring that the actual force tracked the desired force in both cases.
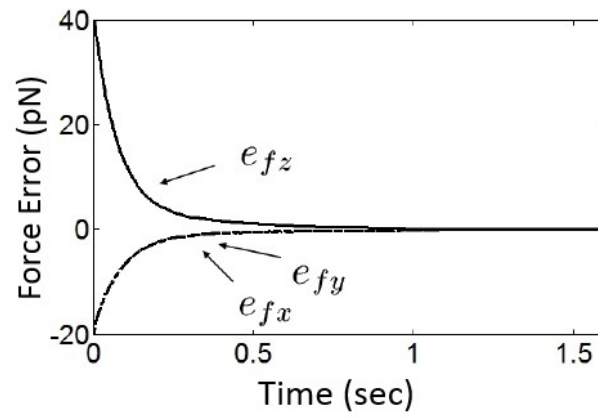
Figure 4.5: Force tracking error with respect to a step desired force.
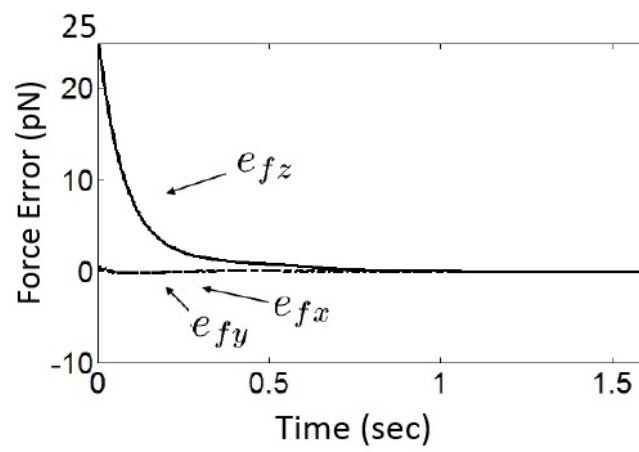
Figure 4.6: Force tracking error with respect to a sinusoidal desired force.

4.6   Conclusions

This chapter presents the development of a robust force control algorithm that enables accurate application of an external force on a dynamics model of biological cells. Such force control is achieved by utilizing a six-strut cellular tensegrity model constructed based on the structural approach. Leveraging on the more comprehensive description of the nonlinearity and dynamic coupling of internal structural elements provided by this tensegrity model, a novel robust control law that can effectively deal with model uncertainties and partial state measurability, is synthesized. The work reported in this chapter represents an initial step in analytical investigation of localized force-bearing interactions between a cellular tensegrity model and an external mechanical manipulator. The significance of this work is that such force-bearing interactions explicitly take into account the dynamics of the cytoskeleton in governing cellular mechanical response. Consequently, the approach and results presented in this work are directly relevant to the development of biomanipulation tools and techniques for mechanobiology. Another potential area where this proposed approach could be useful is microinjection. At the operational level, the key objective in a microinjection process is to apply a dynamical force on the surface of a cell in order to pierce the cell membrane. Optimizing this process requires sophisticated force control techniques in order to reduce cell deformation so as to avoid degrading its internal integrity. The approach reported can be utilized to meet this requirement.

Chapter 5

Force Control of a Cellular Tensegrity Model with Time-Varying Mechanical Properties

5.1 Introduction

In previous chapter, the six-strut tensegrity structure is discussed under the assumption that the struts are viewed as rigid bars of identical length L under compression whereas the tendons are viewed as identical viscoelastic Voigt elements - the viscoelastic Voigt elements are consisted of a linear elastic spring with constant stiffness and a linear viscous damper with constant damping ratio connected in parallel. This assumption defines the discussed cellular tensegrity a homogenous model with fixed mechanical property. This cellular tensegrity structure produces satisfying results in predicting some cellular behavior(i.g. steady-state elastic response, linear stiffening of cells and etc.). Nonetheless, to

further realize the potential of this model, the cellular tensegrity structure with varying mechanical properties is discussed in this chapter. This is motivated by the fact that living cells will tune the mechanical properties (sometimes significantly) in response to the exogenous forces. Such varying mechanical property under exogenous forces is also the key feature that distinguish living cells from passive materials. In this respect, a cellular tensegrity structure with varying mechanical properties will entitle the tensegrity structure more freedom to describe the mechanical behavior and thus be more realistic and effective.

In this chapter, the force control strategy for force-bearing cell manipulation described in Chapter 4 is further improved. With respect to the work presented in Chapter 4, the cellular tensegrity model is assumed to be heterogenous and with varying mechanical property, which renders the tensegrity model more capable in capturing the mechanical behavior of living cells under external forces. The variance of the mechanical properties is reflected on the time- of the tendons, which are assumed to be unknown. The modified tensegrity model complicates the modeling and results in differences in the control development and stability analysis with regard to the previous chapter.

5.2   Cellular Tensegrity Model and Task Setting

This section explains the heterogeneous cellular tensegrity model with varying stiffness which is a modified version of the model studied in previous chapter, and formulate the problem of robust force control associated with this model.

5.2.1 Cellular Tensegrity Model with Unknown Time-Varying Stiffness and Damping Coefficient

A heterogeneous tensegrity structure, where the stiffness of the tendons are nonuniform and time-varying whereas the damping ratio of the tendons are identical and time-varying throughout the structure, is considered in this chapter. More specifically, the stiffness of the tendons is assumed to be nonuniform among the five classes of tendons which are characterized in [47](the intermediate filaments (I) class, the saddle (S) tendons class, the top (T) tendons class, the diagonal (D) tendons class and the vertical (V) tendons class), while the stiffness of the tendons of the same class is uniform. The stiffness of the five classes of tendons are denoted as $k_I(t)$, $k_S(t)$, $k_T(t)$, $k_D(t)$ and $k_V(t)$, respectively. The damping ratio is denoted as $c(t)$. It is assumed that both stiffness and damping ratio are positive. Moreover, while the stiffness and damping ratio are unknown, the boundaries of stiffness and damping ratio are assumed to be known. Furthermore, considering the nature of the varying-stiffness and damping ratio as a result of the biological response of the cells under external force, it is expected that both the stiffness and damping ratio will approach some certain constants, respectively, after some time period when the force-induced biological response is fully expressed.

For the heterogeneous tensegrity model, the constitutive equation of ith tendon is

$$f_{ti} = k_i(t) \cdot (\frac{l_i}{l_{io}} - 1) + c(t) \cdot \dot{l}_i, \quad (i = 1, ..., 33) \tag{5.1}$$

where, k_i is the stiffness of ith tendon and $k_i \in \{k_I(t), k_S(t), k_T(t), k_D(t), k_V(t)\}$, depending on the class of the tendon; f_{ti} is the force within ith tendon when the tendon is sustaining deformation; l_i and l_{io} are the length and the initial length of ith tendon, respectively; $\dot{l}_i$ is the time derivative of l_i.

Similar to Chapter 4, it is considered that the external force $f = [f_x\ f_y\ f_z]^T \in \mathbb{R}^{3\times1}$ is applied on B_1D_1 at a point G as indicated in Figure 4.2. The subsequent analysis is readily applicable to other cases where f is applied on any one of the other struts.

With the vector of general coordinates $q_f = [q_1^T\ q_2^T]^T$ defined in Equation (4.3), the motion of equations of the cellular tensegrity model under the condition that the external force is applied on point G on strut B_1D_1 are given as:

$$A_f(q_f)T_f(q_f) + C_f(q_f)\dot{q}_f = \begin{bmatrix} f \\ 0 \end{bmatrix} \tag{5.2}$$

The general forms of A_f, T_f and C_f are presented in Appendix D.

It is noticed that $A_f(q_f)T_f(q_f)$ can be expressed as

$$A_f(q_f)T_f(q_f) = \begin{bmatrix} k_{vec}^T \cdot b_1 \\ \vdots \\ k_{vec}^T \cdot b_i \\ \vdots \\ k_{vec}^T \cdot b_{33} \end{bmatrix} \tag{5.3}$$

where $k_{vec} \in \mathbb{R}^{33\times1}$ and its jth element is $k_j (1 \leq j \leq 33)$(i.e., $k_{vec} \triangleq [k_1,...,k_j,...,k_{33}]^T$); $b_i \in \mathbb{R}^{33\times1}(1 \leq i \leq 33)$ and its jth element is $\frac{\partial l_j}{\partial q_{fi}} \cdot (l_j - l_{j0})(1 \leq j \leq 33)$.

Let

$$C_f = c(t) \cdot \begin{bmatrix} C_{11} & C_{12} \\ C_{21} & C_{22} \end{bmatrix}, \quad A_f T_f = \begin{bmatrix} M_1 \\ M_2 \end{bmatrix}$$

with $C_{11} \in \mathbb{R}^{3\times3}$, $C_{12} \in \mathbb{R}^{3\times21}$, $C_{21} \in \mathbb{R}^{21\times3}$, $C_{22} \in \mathbb{R}^{21\times21}$, $M_1 \in \mathbb{R}^{3\times1}$, and

$M_2 \in \mathbb{R}^{21 \times 1}$. Then (5.3) can be rewritten as

$$M_1(q_1, q_2) + c(t) \cdot C_{11}(q_1, q_2)\dot{q}_1 + c(t) \cdot C_{12}(q_1, q_2)\dot{q}_2 = f \qquad (5.4)$$

$$M_2(q_1, q_2) + c(t) \cdot C_{21}(q_1, q_2)\dot{q}_1 + c(t) \cdot C_{22}(q_1, q_2)\dot{q}_2 = 0 \qquad (5.5)$$

5.2.2 Force-bearing Interaction and System Uncertainties

Similar to Chapter 4, the external force f is considered being applied on the tensegrity structure by a manipulator whose dynamics is known and described (in the Cartesian task space) by

$$H_r(x)\ddot{x} + C_r(x, \dot{x})\dot{x} + g_r(x) = u - f \qquad (5.6)$$

where, $x, \dot{x}, \ddot{x} \in \mathbb{R}^3$ are the position, velocity, and acceleration of the links of the manipulator, respectively, $H_r(x) \in \mathbb{R}^{3 \times 3}$ is the inertia matrix; $C_r(x, \dot{x}) \in \mathbb{R}^{3 \times 3}$ represents the Centripetal-Coriolis effects, $g_r(x) \in \mathbb{R}^3$ represents conservative forces (e.g., gravity), and $u \in \mathbb{R}^3$ is the control input. Under the condition that the end-effector of manipulator remains in contact with the tensegrity structure G (thus taking $x = q_1$), Equation (5.6) becomes

$$H_r(q_1)\ddot{q}_1 + C_r(q_1, \dot{q}_1)\dot{q}_1 + g_r(q_1) = u - f \qquad (5.7)$$

Invoking (5.4) and (5.5), the contact force can be rewritten in the following form:

$$f = c(t) \cdot \Psi(q_1, q_2)\dot{q}_1 + \Phi(q_1, q_2, k) \qquad (5.8)$$

where, $\Psi(q_1, q_2) \triangleq C_{11} - C_{12}C_{22}^{-1}C_{21}$ and $\Phi(q_1, q_2, k) \triangleq M_1 - C_{12}C_{22}^{-1}M_2$, under the condition that C_{22} is nonsingular during the process when the tensegrity structure sustains the applied external force.

Noticing (5.3), the entries of $\Phi(q_1, q_2, k_{vec})$, $\phi_i(q_1, q_2, k_{vec})$ can be expressed as

$$\phi_i(q_1, q_2, k_{vec}) = k_{vec}^T \cdot \phi_i^*(q_1, q_2), \quad 1 \leq i \leq 3 \tag{5.9}$$

where $\phi_i^* \in \mathbb{R}^{33 \times 1}$ is independent of k_{vec}.

Subsequently, Φ can be expressed in the following form:

$$\Phi(q_1, q_2, k_{vec}) = K \cdot \Phi^*(q_1, q_2) \tag{5.10}$$

where,

$$K = \begin{bmatrix} k_{vec}^T & 0 & 0 \\ 0 & k_{vec}^T & 0 \\ 0 & 0 & k_{vec}^T \end{bmatrix}, \Phi^*(q_1, q_2) = \begin{bmatrix} \phi_1^*(q_1, q_2) \\ \phi_2^*(q_1, q_2) \\ \phi_3^*(q_1, q_2) \end{bmatrix}.$$

Further, the derivative of contact force in (5.8) is obtained as:

$$\dot{f} = c(t) \cdot \Psi(q_1, q_2)\ddot{q}_1 + c(t) \cdot \varpi_1 + K \cdot \varpi_2 + \Delta_1 \tag{5.11}$$

where, $\varpi_1(\dot{q}_1, \dot{q}_2, q_1, q_2) \triangleq \dot{\Psi}(q_1, q_2)\dot{q}_1$, $\varpi_2(\dot{q}_1, \dot{q}_2, q_1, q_2) \triangleq \dot{\Phi}^*(q_1, q_2)$ and $\Delta_1(\dot{q}_1, q_1, q_2, \dot{c}) \triangleq \dot{c}(t) \cdot \Psi\dot{q}_1 + \dot{K} \cdot \Phi^*$.

By introducing $c^*(t) \triangleq c^{-1}(t)$ and $K^*(t) \triangleq K \cdot c^{-1}(t)$, the above equation can be expressed as

$$c^*(t) \cdot \dot{f} = \Psi(q_1, q_2)\ddot{q}_1 + \varpi_1 + K^* \cdot \varpi_2 + \Delta_2 \tag{5.12}$$

where $\Delta_2(\dot{q}_1, q_1, q_2, c) \triangleq c^*(t) \cdot \Delta_1$.

Since $k_i \in \{k_I, k_S, k_T, k_D, k_V\}$, the set of independent unknown parameters of K can be denoted as $\theta_k \in \mathbb{R}^r (r \leq 5)$. Then, by noting that K is linear with

respect to θ_k, it yields

$$K^* \cdot \varpi_2 = Y(\varpi_2)\theta(t), \quad \theta(t) \triangleq c^{-1}(t) \cdot \theta_k(t) \qquad (5.13)$$

where Y is known.

5.2.3   Control Objective

Although the mechanical properties are time-varying, it is reasonable to assume that the bounds of the mechanical properties are known. Moreover, considering that the variance of the mechanical properties is caused by the force-induced biological response, it is reasonable to assume that the mechanical properties will become constant after some time period when the force-induced biological response is fully expressed. Therefore, the following assumptions are made:

Assumption 5.1: $c(t) \in \Omega_c \triangleq \{c(t) : \underline{c} \leq c(t) \leq \overline{c}\}$ and $\theta_k(t) \in \Omega_{\theta_k} \triangleq \{\theta_k(t) : \underline{\theta}_k \leq \theta_k(t) \leq \overline{\theta}_k\}$, where Ω_c and Ω_{θ_k} are known sets (i.e., $\underline{c}, \overline{c} \in \mathbb{R}$, $\underline{\theta}_k, \overline{\theta}_k \in \mathbb{R}^r$ are known positive bounding constant and vectors, respectively). Consequently, $\theta \in \Omega_\theta \triangleq \{\theta : \underline{\theta} \leq \theta \leq \overline{\theta}\}$, where $\underline{\theta} = \overline{c}^{-1} \cdot \underline{\theta}_k$ and $\overline{\theta} = \underline{c}^{-1} \cdot \overline{\theta}_k$.

Assumption 5.2: $\dot{c}^*|_{t>t_b} = 0$, $\dot{\theta}|_{t>t_b} = 0$, where $t_b > 0$.

The control objective is to design control law u for the three degree-of-freedom manipulator as described in (5.7) so that interaction force (between the end-effector and cellular tensegrity structure) as described in (5.8) follows the desired force trajectory f_d (generated from $\dot{f}_d$) in presence of the uncertainties due to unknown time-varying mechanical properties, which satisfy Assumption 5.1 and 5.2.

5.3 Control Development

In this section, an adaptive robust sliding-mode force controller motivated by [84] and [56] is developed. The robust control law is adopted to compensate the uncertainties of the time-varying stiffness and damping coefficient of the tendons of the tensegrity structure. The adaptive control is integrated due to Assumption 5.2 and regarded to be able to further enhance the control performance.

5.3.1 Synthesis of Control Law

To quantify the control objective, force error $e_f \in \mathbb{R}^3$ is defined

$$e_f \triangleq f - f_d \tag{5.14}$$

Similar to Chapter 4, a vector $r_f \in \mathbb{R}^3$ incorporated with an integral force feedback term is introduced

$$r_f = e_f + \Lambda_1 I_f \tag{5.15}$$

where $\Lambda_1 = \Lambda^T > 0$. matrix and I_f is defined as

$$I_f = -\Lambda_1^{-1} e_f(0) + \int_0^t e_f(\tau) d\tau \tag{5.16}$$

Obviously, $r_f(0) = 0$. Note that

$$\dot{r}_f = \dot{f} - \epsilon \tag{5.17}$$

with $\epsilon \triangleq \dot{f}_d - K_1 e_f$.

The error of the estimate of c^* and θ are denoted as

$$\tilde{c}^* = \hat{c}^* - c^*, \quad \tilde{\theta} = \hat{\theta} - \theta \tag{5.18}$$

In the sequel, $\lambda_{max}(A)$ and $\lambda_{min}(A)$ denote the maximum and minimum eigenvalues of a square matrix A, respectively. $\|B\|$ denotes the Euclidean norm of any vector B.

The following control law has been proposed:

$$u(q_1, \dot{q}_1, q_2, \dot{q}_2, f, \epsilon, r_f) = H_r(q_1)\Psi^{-1}(u_a + u_r) + f + C_r\dot{q}_1 + g_r \tag{5.19}$$

where

$$u_a(q_1, \dot{q}_1, q_2, \dot{q}_2, f, \epsilon, r_f, \hat{\theta}_k, \hat{c}^*) = -\Lambda_f r_f - \varpi_1 - Y\hat{\theta} + \hat{c}^* \cdot \epsilon \tag{5.20}$$

$$u_r(r_f, h, \alpha_1, \beta(t)) = -(1 + \alpha_1 h)h\frac{r_f}{\|r_f\| + \beta(t)} \tag{5.21}$$

with Λ_f being a s.p.d. matrix, α_1 any positive constant and $\beta(t)$ any bounded positive time-varying scalar (i.e., $0 \le \beta(t) \le \beta_{max}$), h any bounding function satisfying

$$h \ge \| -Y(\varpi_2)\tilde{\theta} + \tilde{c}^* \cdot \epsilon + \frac{1}{2}\dot{c}^* r_f + \Delta_2\| \tag{5.22}$$

u_r is a smooth robust control term proposed in [83] which satisfies the following property:

$$h\|r_f\| + r_f^T u_f \le \varepsilon(t), \quad \varepsilon(t) \triangleq \frac{\beta(t)}{4\alpha_1} \tag{5.23}$$

The adaptive update law of parameter estimates are given as follows.

$$\dot{\hat{c}}^* = -\text{proj}(\Gamma_c r_f^T \epsilon) \tag{5.24}$$

$$\dot{\hat{\theta}} = \text{proj}(\Gamma_\theta Y^T(\varpi_2)r_f) \tag{5.25}$$

where $\Gamma_c \in \mathbb{R}$ and $\Gamma_\theta \in \mathbb{R}^{r \times r}$ are designed positive adaptation gain and positive-definite constant diagonal adaptation gain matrix, respectively; proj($\cdot$) denotes a sufficiently smooth projection algorithm (cite) utilized to guarantee that $\hat{c}$ and $\hat{\theta}$ satisfy that

$$\hat{c} \in \Omega_c, \quad \hat{\theta} \in \Omega_\theta. \tag{5.26}$$

5.3.2 Stability analysis

Theorem 5.1: Consider the manipulator described by (5.7) interacts with the cellular tensegrity model described by (5.4) and (5.5). Provided that Assumption 5.1 and 5.2 are satisfied, the following statements hold when proposed control law (5.19) is applied: i) when $t \leq t_b$, e_f and I_f are bounded and exponentially converge to some balls with adjustable size; ii) when $t > t_b$, e_f exponentially converges to zero.

Proof: Invoking that $c^* > 0$, a Lyapunov function $V(t) \in \mathbb{R}$ is chosen as

$$V = \frac{1}{2}c^* r_f^T r_f \tag{5.27}$$

The derivative of V is:

$$
\begin{aligned}
\dot{V} &= r_f^T c^* \dot{r}_f + \frac{1}{2} r_f^T \dot{c}^* r_f \\
&= r_f^T c^* (\dot{f} - \epsilon) + \frac{1}{2} r_f^T \dot{c}^* r_f \\
&= r_f^T (c^* \cdot \dot{f} - c^* \cdot \epsilon) + \frac{1}{2} r_f^T \dot{c}^* r_f \\
&= r_f^T [\Psi \ddot{q}_1 + \varpi_1 + f(\varpi_2) + Y(\varpi_2)\theta + \Delta_2 \\
&\quad -c^* \cdot \epsilon + \frac{1}{2} \dot{c}^* r_f] \\
&= r_f^T [\Psi H_r^{-1}(u - f - C_r \dot{q}_1 - g_r + \varpi_1 + \\
&\quad Y(\varpi_2)\theta + \Delta_2 - c^* \cdot \epsilon + \frac{1}{2} \dot{c}^* r_f] \\
&= r_f^T [u_a + u_r + \varpi_1 + Y(\varpi_2)\theta + \Delta_2 \\
&\quad -c^* \cdot \epsilon + \frac{1}{2} \dot{c}^* r_f] \\
&= -r_f^T \Lambda_f r_f + r_f^T [-Y(\varpi_2)\tilde{\theta}_k + \tilde{c}^* \cdot \epsilon + \Delta_2 \\
&\quad + \frac{1}{2} \dot{c}^* r_f]
\end{aligned}
\tag{5.28}
$$

Invoking (5.23), it follows

$$
\begin{aligned}
\dot{V} &\leq -r_f^T \Lambda_f r_f + \varepsilon(t) \\
&\leq -\frac{2\gamma_1}{c^*} V + \frac{\beta_{max}}{4\alpha_1}
\end{aligned}
\tag{5.29}
$$

where $\gamma_1 = \lambda_{min}(\Lambda_f)$.

Since (5.28) is valid for $t \in [0, +\infty)$, it is valid for $t \in [0, t_b]$. Consequently, with similar analysis as in Chapter 4 (Equation (4.28)- (4.36)), it can be concluded that e_f, I_f exponentially approach some ball with adjustable size when $t \in [0, t_b]$. This concludes statement i).

Consider the case that $t \in [t_b, +\infty)$.

According to Assumption 5.2, $\Delta_2 = 0$ and $\dot{c}^* = 0$. It follows that

$$\dot{V}|_{t \geq t_b} = -r_f^T K_f r_f - \tilde{\theta}_k^T Y^T(\varpi_2) r_f + \tilde{c}^* \epsilon^T r_f \qquad (5.30)$$

Moreover, invoking (5.18), it is obtained

$$\dot{\tilde{c}}^*(t)|_{t \geq t_b} = \dot{\hat{c}}^*(t), \quad \dot{\tilde{\theta}}(t)|_{t > t_b} = \dot{\hat{\theta}}(t) \qquad (5.31)$$

Considering the parameter error $\hat{c}^*$ and $\hat{\theta}$, the augmented Lyapunov function candidate is chosen as

$$V_a = V + \frac{1}{2}\Gamma_c^{-1}\tilde{c}^{*2} + \frac{1}{2}\tilde{\theta}^T \Gamma_\theta^{-1}\tilde{\theta} \qquad (5.32)$$

From (5.28), $r_f \in L_\infty^3$ and hence $r_f(t_b)$ is bounded. Moreover, from (5.24) and (5.25), $\dot{\hat{c}}^* \in L_\infty$ and $\dot{\hat{\theta}} \in L_\infty^r$ and hence, $\hat{c}^*$ and $\hat{\theta}$ are bounded. These imply that $V_a(t_0)$ is bounded. Invoking (5.24), (5.25), (5.30) and (5.31), the time derivative of V_a for $t \in [t_b, \infty)$ is

$$
\begin{aligned}
\dot{V}_a|_{t \geq t_b} &= -r_f^T K_f r_f - \tilde{\theta}_k^T Y^T(\varpi_2) r_f + \tilde{c}^* \epsilon^T r_f \\
&\quad + \frac{1}{2}\Gamma_c^{-1}\tilde{c}^*\dot{\hat{c}}^* + \frac{1}{2}\tilde{\theta}\Gamma_\theta^{-1}\dot{\hat{\theta}} \\
&\leq -\frac{2\gamma_1}{c^*}r_f^T r_f \qquad (5.33)
\end{aligned}
$$

According to statement i), V_{t_b} is bounded. Therefore, (5.33) implies that $V_a \in L_\infty$.

From (5.29) and (5.33), it can be obtained that $r_f \in L_2 \cap L_\infty$. It is also easy to check that $\dot{r}_f$ is bounded. Hence, using Barbalat's lemma[85], (5.33) implies that r_f exponentially approaches zero.

From (5.15), the transfer function between r_f and e_f is

$$e_f = r_f - G_1 r_f \qquad (5.34)$$

where $G_1 = \text{diag}\{\frac{\lambda 11}{S+\lambda_{11}}, \frac{\lambda 12}{S+\lambda_{12}}, \frac{\lambda 13}{S+\lambda_{13}}\}$ with $\lambda_{1i}(i = 1, 2, 3)$ the ith diagonal element of Λ_1 (i.e., $\Lambda_1 = \text{diag}\{\lambda_{11}, \lambda_{12}, \lambda_{13}\}$). It is obvious that G_1 is stable and hence e_f exponentially approaches zero. This concludes statement ii). $\square$.

5.4   Numerical Simulation

Numerical simulations are conducted to demonstrate the effectiveness of the proposed force control law.
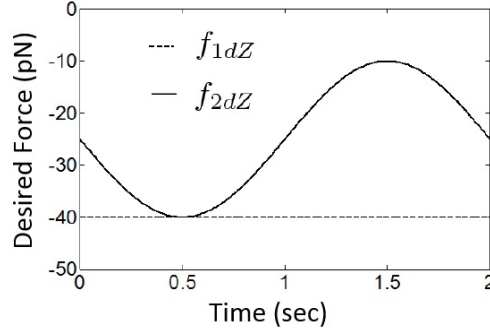
Figure 5.1: Trajectories of the two types of desired force used in the simulations.

In the simulations, the force is assumed to be exerted on point G of strut $B_1 D_1$ where $r = 0.75L$. Similar to Chapter 4, two types of typical force trajectories are used: a step $f_{1d} = [20\ 20\ f_{1dZ}]^T$ (pN), and a sinusoid $f_{2d} = [0\ 0\ f_{2dZ}]^T$ (pN), where, $f_{1dZ} = -40$ and $f_{2dZ} = -25 - 15 * \sin \pi t/4$, as shown in Figure 5.1. The length of the struts L is assumed to be $10\mu m$. The time-varying stiffness $k_I(t), k_S(t), k_T(t), k_D(t), k_V(t)$ and $c(t)$ are defined in the following way

:

$$k_I(t) = \begin{cases} 10 + 2.5 sin\frac{\pi}{12}t\text{(pN)} & 0 \le t < 6, \\ 12.5\text{(pN)} & t \ge 6. \end{cases}$$

$$k_S(t) = \begin{cases} 100 + 25 sin\frac{\pi}{12}t\text{(pN)} & 0 \le t < 6, \\ 125\text{(pN)} & t \ge 6. \end{cases}$$

$$k_T(t) = \begin{cases} 125 + 25 sin\frac{\pi}{16}t\text{(pN)} & 0 \le t < 8, \\ 150\text{(pN)} & t \ge 8. \end{cases}$$

$$k_D(t) = \begin{cases} 150 + 25 sin\frac{\pi}{20}t\text{(pN)} & 0 \le t < 10, \\ 175\text{(pN)} & t \ge 10. \end{cases}$$

$$k_V(t) = \begin{cases} 175 + 25 sin\frac{\pi}{24}t\text{(pN)} & 0 \le t < 12, \\ 200\text{(pN)} & t \ge 12. \end{cases}$$

$$c(t) = \begin{cases} 125 + 25 sin\frac{\pi}{24}t\text{(pN s/}\mu\text{ m)} & 0 \le t < 12, \\ 150\text{(pN s/}\mu\text{ m)} & t \ge 12. \end{cases}$$

In the simulation, the boundaries for each type of stiffness and their time derivative are assumed as following: $k_I \in [5, 15](pN)$, $k_S \in [50, 175]$, $k_T \in [75, 200]$, $k_D \in [100, 225]$, $k_V \in [125, 250]$, $\dot{k}_I \in [-5, 5]$, $\dot{k}_S \in [-50, 50]$, $\dot{k}_T \in [-50, 50]$, $\dot{k}_D \in [-50, 50]$, $\dot{k}_V \in [-50, 50]$; the boundaries of the damping coefficient and its derivative are assumed to be $\hat{c} \in [75, 200](i.e., \underline{c} = 75, \overline{c} = 200)$. θ_k is chosen as $[k_I, k_S, k_T, k_D, k_V]^T$. Subsequently, $\underline{\theta}_k$, $\overline{\theta}_k$, $\underline{\theta}$, $\overline{\theta}$ are set accordingly. The smooth projector which ensures that $\underline{\theta} \le \theta \le \overline{\theta}$ and $\underline{c} \le c \le \overline{c}$ is adopted from [86].

The initial states of the tensegrity model in the absence of external force considered in the simulation is assigned the same as Chapter 4, which is presented in Appendix C. The prestress P, which characterizes the spherical prestressable configuration, is assumed to be 2. The basis tensions are set at the same values

as Chapter 4.

The other control parameters are set as follows: $\Lambda_1 = \text{diag}(10)$, $\Lambda_f = \text{diag}(2)$, $\Gamma_c = 10$, $\Gamma_\theta = \text{diag}(10)$, and $\alpha = 0.25$.

The simulation results are presented in Figure 5.2 and Figure 5.3. It is indicated that the force control law was effective in ensuring that the actual force traced the desired force in both cases.
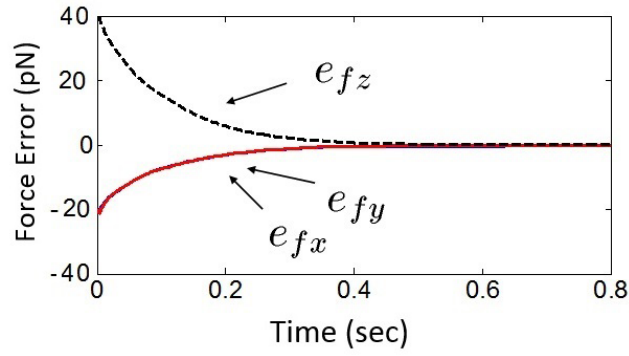
Figure 5.2: Force tracking error with respect to a step desired force.

5.5 Conclusions

This chapter presents the development of a force control algorithm to achieve manipulation of applied force on a cellular tensegrity model with time-varying mechanical properties(i.e., stiffness and damping coefficient). Compared with previous homogeneous tensegrity as discussed in Chapter 4, a heterogeneous tensegrity model in terms of the stiffness of the tendons is considered. As such, the proposed model is entitled more freedom in modeling the mechanical behavior of living cells. Moreover, the introduction of time-varying attribute of the mechanical properties of the six-strut cellular tensegrity structure, which aims at modeling the external force induced variance of cellular mechanical properties while cell is sustaining mechanical external force, further enhances

(a)

(b)
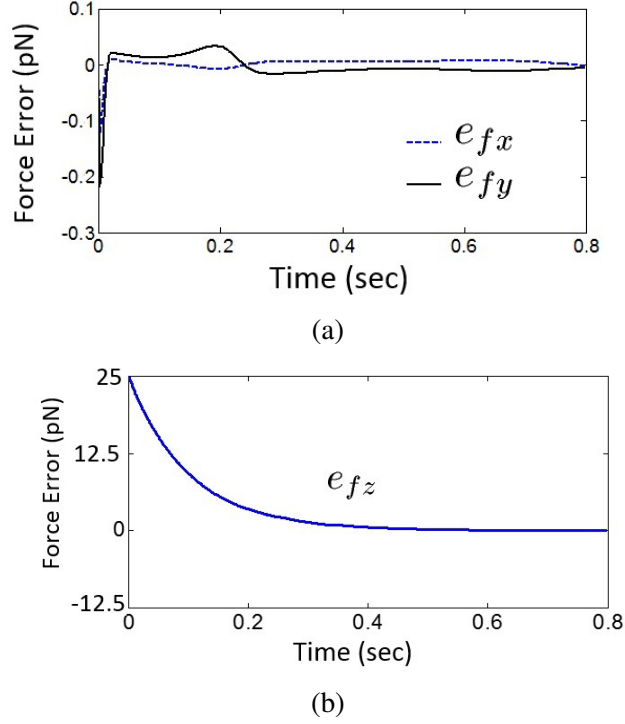
Figure 5.3: Force tracking error with respect to a sinusoidal desired force.

the proposed cellular tensegrity model. To the best of our knowledge, this proposed cellular tensegrity model with time-varying mechanical properties is the first mechanical model attempting to capture the "active" feature of living cells under external mechanical load.

The present study mainly concentrates on the development of force control algorithm based on the proposed cellular tensegrity model instead of parameter estimation of the proposed model. Nonetheless, the proposed algorithm only requires the boundaries of the stiffness and damping coefficient and their time derivative rather than the exact value. This renders the force control law robust, especially considering the individual difference of mechanical properties among the same class of cells. Furthermore, it combines adaptive control to further improve the performance of the controller in terms of reducing uncertainties considering that the mechanical properties will reach certain values when the biological response is fully expressed. Simulation results are presented to validate

the effectiveness of the proposed force control algorithm.

Chapter 6

Force Tracking Control in Biomanipulation Using Neural Networks

6.1 Introduction

NN-based estimation methods have been shown to be well suited for control systems with uncertain dynamic models. This merit renders the NN-based control desirable for the force control problem involving cellular tensegrity model and micro/nano manipulator as discussed in Chapter 4 and Chapter 5, since the interaction force model is a coupled and nonlinear function with uncertainty. This chapter presents the development of a NN-based approximation adaptive control law for the force control problem described in Chapter 4. Thanks to the nature of NN estimation, despite that the control development is based on the tensegrity model, the results should be directly applicable to the interaction force control problem between manipulator and viscoelastic materials, which represents a large class of force control problem in biomanipulation. In particular, to

93

avoid excessive contact force is given a special interest since it is undesirable in biomanipulation - it may damage the biological material/structure to handle and thus the failure of the operation.

6.2 Dynamic Model of a Manipulator in Contact with a Cellular Tensegrity Model

This section briefly reviews the homogeneous cellular tensegrity model as described in Chapter 4, and presents the dynamics of the manipulator used for applying the force.

6.2.1 Contact Force Model

As derived in Equation (4.11), the contact force model for the homogeneous cellular tensegrity model with constant mechanical properties is

$$f = \Psi(q_1, q_2, c)\, \dot{q}_1 + \Phi(q_1, q_2, k) \tag{6.1}$$

where, $q_1 \in \mathbb{R}^{3 \times 1}$ is the Cartesian coordinates of the point where the external force is applied; $q_2 \in \mathbb{R}^{21 \times 1}$ is the vector assembles the rest of the generalized coordinates; c and k are the unkown stiffness and damping ratio of the tendons, respectively.

Further, the derivative of contact force is (from Equation (4.12))

$$\dot{f} = \Psi(q_1, q_2, c)\ddot{q}_1 + \varpi(\dot{q}_1, q_1, q_2, c, k) \tag{6.2}$$

6.2.2 Dynamic Model of Manipulator

It is considered that the external force f being applied on the tensegrity structure by a manipulator whose dynamics is known and described (in the Cartesian space) by

$$H_r(x)\,\ddot{x} + C_r(x,\dot{x})\,\dot{x} + g_r(x) = u - f \qquad (6.3)$$

where, $x, \dot{x}, \ddot{x} \in \mathbb{R}^3$ are the position, velocity, and acceleration of the links of the manipulator, respectively, $H_r(x) \in \mathbb{R}^{3\times3}$ is the inertia matrix, $C_r(x,\dot{x}) \in \mathbb{R}^{3\times3}$ represents the Centripetal-Coriolis effects, $g_r(x) \in \mathbb{R}^3$ represents conservative forces (e.g., gravity) and $u \in \mathbb{R}^3$ is the control input.

The above manipulator dynamics model discussed in this work is under the following reasonable assumptions:

Assumption 6.1: The dynamics model of manipulator is exactly known, i.e., H_r, C_r, g_r are known. As discussed later, this assumption can be relaxed under the proposed control scheme.

Assumption 6.2: The task space inertial matrix $H_r(x)$ is symmetric positive definite and hence $H_r(x)$ is always invertible.

Assumption 6.3: The manipulator position and velocity, x and $\dot{x}$, are measurable.

The end-effector of the manipulator is considered to remain in contact with the tensegrity structure at the point G. Thus, by taking $x = q_1$, the dynamics of manipulator (6.3) becomes

$$H_r(q_1)\,\ddot{q}_1 + C_r(q_1,\dot{q}_1)\,\dot{q}_1 + g_r(q_1) = u - f \qquad (6.4)$$

6.2.3 Control Objective

The dynamic model for a three degree-of-freedom manipulator with the cellular tensegrity model is described by (6.1) and (6.4). Similar as in Chapter 4, it is considered that the mechanical property of the tensegrity model is not well known, i.e., only reasonable estimates of stiffness k and damping coefficient c are available. Another issue is state measurability. Since the external force is considered to be applied on the tensegrity structure by point contact (i.e., at the point G as illustrated in Figure 4.2), with Assumption 6.3, it is reasonable to expect that, for the state of the overall system, only q_1 and $\dot{q}_1$ are measurable with suitable instrumentation of the manipulation system.

The specific control objective is to design control law u for the three degree-of-freedom manipulator as described in (6.4) so that interaction force (between the end-effector and cellular tensegrity structure) as described in (6.1) follows the desired force trajectory f_d (generated from $\dot{f}_d$) in presence of uncertainties due to unknown mechanical properties (i.e., c and k are unknown) and partial state measurability (q_1 and $\dot{q}_1$ are the only measurable variables).

Considering that both q_2 and $\dot{q}_2$ are functions of variables q_1 and $\dot{q}_1$ due to the fact that c, k and q_f are constant, the contact force model falls under a class of general nonlinear viscoelastic model described by $f = w(q)\dot{q} + v(q)$ with q represent the general deformation of the model. Since we use NN to approximate Ψ (i.e., w) and ϖ (i.e., v), the proposed NN based controller is applicable for the force control problem where environment is soft compliant and the reaction force can be described as $f = w(q)\dot{q} + v(q)$.

6.3 Notations

$\|\cdot\|$ denotes Frobenius norm of matrices and the standard Euclidean norm of vectors, i.e., given a matrix A and a a vector B, the Frobenius norm and Euclidean norm are defined as $\|A\|^2 = tr(A^T A) = \sum_{i,j} a_{ij}^2$ and $\|B\|^2 = \sum_i B_i^2$. $\lambda_{max}(A)$ and $\lambda_{min}(A)$ denote the largest and smallest eigenvalues of a square matrix A, respectively.

6.4 Control Development

The nonlinear coupled contact force model (6.1) is much more complex than the linear spring model and other contact models, and thus the force control algorithm often discussed in the literature is not directly applicable. Moreover, the uncertainty of the mechanical property and partial state measurability(i.e., q_2 is not measurable) further complicates the control problem. Hence, a strategic combination of NN and adaptive control is utilized in the subsequent control development. In this section, the RBFNNs is firstly used to approximate the unknown dynamics in the contact force model. Subsequently, an adaptive control law based on the NN-based approximation is proposed and the stability analysis is presented.

The force tracking error $e \in \mathbb{R}^3$ is defined as:

$$e \triangleq f - f_d \qquad (6.5)$$

Invoking Equation (4.9) and (4.10) and the fact that q_{fr} is known constant, it is known that q_2 and $\dot{q}_2$ are functions of variables q_1 and $\dot{q}_1$. Consequently, considering that c and k are constant, $h_f(Z_f) \in \mathbb{R}^3$ and $h_g(Z_g) \in \mathbb{R}^{3\times3}$ can be

introduced in the following way to facilitate the control development:

$$h_g(Z_g) \triangleq \Psi(q_1, q_2, c) \tag{6.6}$$

$$h_f(Z_f) \triangleq \varpi(\dot{q}_1, q_1, q_2, c, k) \tag{6.7}$$

where $Z_f = Z_g = [\, q_1^T, \dot{q}_1^T \,]^T$. According to Assumption 6.3, Z_f and Z_g are measurable. Therefore, (6.2) can be rewritten as

$$\dot{f} = h_g(Z_g)\ddot{q}_1 + h_f(Z_f) \tag{6.8}$$

6.4.1   NN Function Estimation

RBFNNs is an efficient tool for modeling nonlinear functions on account of its excellent capability in function approximation. With the ideal weights $W_f^* \in \mathbb{R}^{L_1}$ and $W_g^* \in \mathbb{R}^{L_2 \times 3}$, and the basis function vector $S_f(Z_f) \in \mathbb{R}^{L_1}$ and the basis function matrix $S_g(Z_g) \in \mathbb{R}^{L_2 \times 3}$, $h_f(Z_f)$ and $h_g(Z_g)$ can be represented by RBFNNs as

$$h_f(Z_f) = W_f^{*T} S_f(Z_f) + \epsilon_f \tag{6.9}$$

$$h_g(Z_g) = W_g^{*T} S_g(Z_g) + \epsilon_g \tag{6.10}$$

where ϵ_f and ϵ_g are the approximation errors corresponding to the ideal weights. The approximation of $h_f(Z_f)$ and $h_g(Z_g)$ are respectively given as

$$\hat{h}_f(Z_f) = \hat{W}_f^T S_f(Z_f) \tag{6.11}$$

$$\hat{h}_g(Z_g) = \hat{W}_g^T S_g(Z_g) \tag{6.12}$$

where $\hat{W}_f \in \mathbb{R}^{L_1}$ and $\hat{W}_g \in \mathbb{R}^{L_2 \times 3}$ are the estimates of NN value matrices.

The RBFNNs estimation discussed in this work possess the following properties which are utilized in the subsequent development.

Property 1: The idea weights W^* are defined as the weights that minimize the norm of approximation error for all $Z \in \Omega_Z \subset R^L$ [52].

$$W^* \triangleq \arg \min_{\hat{W} \in \Omega_W} \left\{ \sup_{Z \in \Omega_Z} |h(Z) - \hat{W}^T S(Z)| \right\} \qquad (6.13)$$

where Ω_W is some suitable prefixed large compact set.

Property 2: The Gaussian RBFNN adopted in this work uses the Gaussian functions of the form

$$s_i(Z) = \exp \left[\frac{-(Z - a_i)^T (Z - a_i)}{b_i^2} \right], i = 1, 2, ..., L \qquad (6.14)$$

where a_i and b_i are the center of the receptive field and the width of the Gaussian function, respectively.

Property 3:[69] $\|S(Z)\|$ is bounded by known constant, i.e., $\|S_f(Z_f)\| \leq \zeta_f$, $\|S_g(Z_g)\| \leq \zeta_g$, with $\zeta_f > 0$ and $\zeta_g > 0$.

Property 4: The ideal weights are assumed to exist and bounded, i.e., $\|W_f^*\| \leq \bar{W}_f$, $\|W_g^*\| \leq \bar{W}_g$, with $\bar{W}_f > 0$ and $\bar{W}_g > 0$.

Property 5: The NN approximation errors corresponding to the idea weights are bounded over a compact set, i.e., $\|\epsilon_f\| \leq \bar{\epsilon}_f$, $\|\epsilon_g\| \leq \bar{\epsilon}_g$, with $\bar{\epsilon}_f > 0$ and $\bar{\epsilon}_g > 0$.

6.4.2 Synthesis of Control Law

6.4.2.1 Control Law Design

Define $\varrho \triangleq \ddot{q}_1$. Based on Assumption 6.1, the control law of the manipulator (6.4) is designed as

$$u(q_1, \dot{q}_1, \Phi(\varrho^*), f) = H_r(q_1)\Phi(\varrho^*) + C_r(q_1, \dot{q}_1)\dot{q}_1 + f \qquad (6.15)$$

where, $\varrho^* = [\varrho_1^* \ \varrho_2^* \ \varrho_3^*]^T$ denotes the nominal control law to be defined later; $\Phi(\varrho^*) = [\Phi(\varrho_1^*) \ \Phi(\varrho_2^*) \ \Phi(\varrho_3^*)]^T$ denotes the function which imposes magnitude and rate constraints on the nominal control law ϱ^*. The magnitude constraint is designed as

$$\Phi(\varrho_i) = \begin{cases} \varrho_{i \ max}, & \text{if} \quad \varrho_i > \varrho_{i \ max} \\ \varrho_i & \text{if} \quad \varrho_{imin} \leq \varrho_i \leq \varrho_{i \ max} \\ \varrho_{i \ min}, & \text{if} \quad \varrho_i < \varrho_{i \ min} \end{cases} \qquad (6.16)$$

where $\varrho_{i \ max}$ and $\varrho_{i \ min}$ are designed upper bound and lower bound, respectively. The bound of $\Phi(\varrho_*)$ is denoted as ϱ_m, i.e., $\|\Phi(\varrho^*)\| \leq \varrho_m$. The rate constraint is designed similarly. A first-order filter similar as in [68] can be used for the implementation of imposing the constraints on both magnitude and rate. The schematic of the configuration of the filter is provided in Figure 6.1.
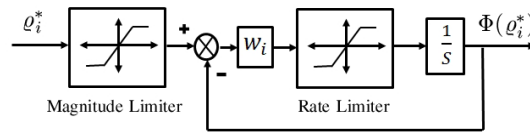

Figure 6.1: Magnitude and rate limiter, where w_i is the bandwidth parameters.

Substituting (6.15) into (6.4) and considering Assumption yield

$$\varrho = \Phi(\varrho^*) \text{ or } \ddot{q}_1 = \Phi(\varrho^*) \qquad (6.17)$$

Equation (6.17) indicates that ϱ^* is designed to be the desired acceleration of the end-effector, while $\Phi(\varrho^*)$ is the actual acceleration. The reasons of introducing $\Phi(\varrho^*)$ to impose magnitude bound and rate bound are to cope with the approximation error of h_g and discontinuity of ϱ^*, respectively. Nonetheless, the introduction of $\Phi(\varrho^*)$ renders the control problem more practical since that most of the real manipulator systems have input saturations in both magnitude and rate, and moreover, the nominal control law designed based on the NN approximation may not be implementable when the NN weights are not fine tuned. The bound of magnitude and rate can be properly chosen by considering both reflecting the actuator limitations of the manipulator and achieving desired control performance.

6.4.2.2 Auxiliary System Design

Define $\Delta\varrho \triangleq \Phi(\varrho^*) - \varrho^*$. To compensate for effects induced by the rate and magnitude constraints as defined by $\Phi(\varrho^*)$, an auxiliary system with state $\xi \in \mathbb{R}^3$ is introduced. Let $\xi(0)$ denote the initial condition of ξ. With ε_1 and ε_2 denoting two positive designed constants satisfying $\varepsilon_1 \geq \|\xi(0)\|$ and $\varepsilon_2 < \varepsilon_1$, the idea of the design of the auxiliary system is described as follows. If $\xi(0) < \varepsilon_1$, ξ is initially set to be driven by an designed function $\chi_1 \in \mathbb{R}^3$ (i.e., $\dot{\xi} = \chi_1$) until $\|\xi(t)\| = \varepsilon_1$. After which, ξ is set to be driven by function $\chi_2 \in \mathbb{R}^3$ (i.e., $\dot{\xi} = \chi_2$), which is designed to force $\|\xi\|$ to decrease from ε_1 to ε_2. Subsequently, ξ is set to be driven by χ_1 again. The process repeats in such a way that every time when $\|\xi\|$ increases to ε_1, ξ is set to be driven by χ_2, and when $\|\xi\|$ reduces to ε_2, ξ is set to be driven by χ_1. If $\xi(0) = \varepsilon_1$, ξ is driven by χ_2 first.

To facilitate the description of the auxiliary system, two sets of time sequences T_1 and T_2 are defined depending on $\|\xi(t)\|$, ε_1 and ε_2. If $\|\xi\| < \varepsilon_1$ holds for all t, then $T_1 = \emptyset$ and $T_2 = \emptyset$. If $\|\xi\| = \varepsilon_1$ occurs for some t, then $T_1 = \{t_{11}, t_{12}, ...\}$

101

is the set contains all the time instants when $\|\xi\| = \varepsilon_1$, where $t_{1i}(i = 1, 2, \ldots)$ denotes the time instant when $\|\xi\| = \varepsilon_1$ for the ith time, and $T_2 = \{t_{21}, t_{22}, \ldots\}$, where each element t_{2i} $(i = 1, 2, \ldots)$ uniquely corresponds to the element t_{1i} in T_1 in the following way: t_{2i} denotes the time instant when $\|\xi\| = \varepsilon_2$ occurs *for the first time after* t_{1i}. Notice that t_{1i} and t_{2i} exist in pair since $\|\xi\|$ only decreases when ξ is driven by χ_2 (i.e., $t_{1i} \le t \le t_{2i}$). The number of the elements of T_1 and T_2 is denoted as Q, which depends on both the system and the design of the auxiliary system. It is noted that Q can be 0 (i.e., $T_1 = T_2 = \emptyset$).

Define

$$
\Omega_t \triangleq \begin{cases} \emptyset & \text{if} \quad Q = 0 \\ \{t \mid t_{1i} \le t \le t_{2i}, i = 1, \ldots M\} & \text{if} \quad Q \ge 1 \end{cases} \tag{6.18}
$$

The auxiliary system is designed as:

$$
\dot{\xi}(t) = \begin{cases} \chi_1(\xi, h'_g, \varrho^*, \Phi(\varrho^*)) & \text{if} \quad t \notin \Omega_t \\ \chi_2(\xi, e, h'_g, \varrho^*, \Phi(\varrho^*)) & \text{if} \quad t \in \Omega_t. \end{cases} \tag{6.19}
$$

where

$$
\chi_1 = -K_1\xi + h'_g(Z_g)(\Phi(\varrho^*) - \varrho^*)
$$

$$
\chi_2 = -K_1\xi - \chi_{20}(e, h'_g, \varrho^*, \Phi(\varrho^*)) + h'_g(Z_g)(\Phi(\varrho^*) - \varrho^*)
$$

$$
\chi_{20}(e, h'_g, \varrho^*, \Phi(\varrho^*)) = \chi_{21}(e, h'_g, \varrho^*, \Phi(\varrho^*)) \, \xi/\|\xi\|^2
$$

$$
\chi_{21}(e, h'_g, \varrho^*, \Phi(\varrho^*)) = \frac{1}{2}\|e^T K_1\|^2 + |e^T h'_g \Delta \varrho| + |e^T \vartheta \Phi(\varrho^*)|
$$

$$
+ \frac{1}{2}\|e\|^2\|\Phi(\varrho^*)\|^2 + \frac{1}{2}\|h'_g \Delta \varrho\|^2
$$

with $K_1 \in \mathbb{R}^{3 \times 3}$ a positive definite matrix and $h'_g \in \mathbb{R}^{3 \times 3}$ a designed function

matrix satisfying

$$i. \quad h'_g \text{ is nonsingular} \tag{6.20}$$

$$ii. \quad \|\vartheta\| \leq \nu, \;\; \vartheta \triangleq \hat{W}_g^T S_g(Z_g) - h'_g \tag{6.21}$$

where ν is any bounded time-varying positive scalar, i.e., $0 \leq \nu \leq \nu_m$. h'_g is introduced to overcome the singularity problem of the estimated input coupling matrix $h_g(Z_g)$. Noting that h'_g is not required to be continuous, it can be simply designed as

$$h'_g = \begin{cases} \hat{h}_g & \text{if} \;\; \hat{h}_g \text{ is nonsingular} \\ \hat{h}_g + \Delta & \text{if} \;\; \hat{h}_g \text{ is singular} \end{cases}$$

where Δ is any scalar matrix to render $\hat{h}_g + \Delta$ nonsingular. Moreover, Δ satisfying $\|\Delta\| \leq \nu$ can be different for each singular $\hat{h}_g$.

Remark 6.1: If $\hat{h}_g$ is assumed or guaranteed by some projection algorithms to be invertible, h'_g can be simply chosen as $\hat{h}_g$, i.e., $\vartheta = 0$. If invertibility of $\hat{h}_g$ cannot be guaranteed, h'_g can be designed as $\hat{h}_g + \tau_h I_n$ with τ_h being a constant larger than the spectral radius of $\hat{h}_g$ as proposed in [79]. The merit of introducing h'_g is to introduce more freedom in designing the control, since any h'_g satisfying (6.20) and (6.21) can be chosen even though it is preferable to choose it close to $\hat{h}_g$. □

Remark 6.2: Let $V_\xi = \frac{1}{2}\xi^T \xi$. Provided $K_1 - \frac{1}{2}I_n > 0$, it is easy to deduce from (6.19) that

$$\dot{V}_\xi \leq -(K_1 - \frac{1}{2}I_n)\xi^T \xi \quad \text{for} \quad t \in [t_{1i}, t_{2i}] \tag{6.22}$$

Equation (6.22) indicates that $\|\xi\|$ decreases when $t \in [t_{1i}, t_{2i}]$. In the case of no input saturation (i.e., $\Delta\varrho = 0$), ξ will remain at zero if $\xi(0) = 0$. If $\xi(0) \neq 0$, ξ will converge exponentially to zero and remain at zero afterwards. □

6.4.2.3 Design of ϱ^* and NN Weights Update Laws

The designed control input ϱ^* is given by

$$\varrho^* = h_g'^{-1}(Z_g)\varrho_0^* \tag{6.23}$$

$$\varrho_0^* = \begin{cases} -\hat{W}_f^T S_f(Z_f) - K_1 e + \dot{f}_d & \text{if } t \notin \Omega_t \\ -\hat{W}_f^T S_f(Z_f) - K_1(e - \xi) + \dot{f}_d & \text{if } t \in \Omega_t \end{cases}$$

Note that ϱ^* may not be continuous. This is acceptable since the introduction of $\Phi(\varrho^*)$.

Define $e_1 \triangleq e - \xi$. The adaptive control law for $\hat{W}_f$ and $\hat{W}_g$ are designed as

$$\dot{\hat{W}}_f = \begin{cases} \Lambda_f(S_f(Z_f)e_1^T - \beta_f \hat{W}_f) & \text{if } t \notin \Omega_t \\ \Lambda_f(S_f(Z_f)e^T - \beta_f \hat{W}_f) & \text{if } t \in \Omega_t \end{cases} \tag{6.24}$$

$$\dot{\hat{W}}_g = \begin{cases} \Lambda_g(S_g(Z_g)\Phi(u)e_1^T - \beta_g \hat{W}_g) & \text{if } t \notin \Omega_t \\ \Lambda_g(S_g(Z_g)\Phi(u)e^T - \beta_g \hat{W}_g) & \text{if } t \in \Omega_t \end{cases} \tag{6.25}$$

where $\Lambda_f = \Lambda_f^T > 0$, $\Lambda_g = \Lambda_g^T > 0$, $\beta_f > 0$, $\beta_g > 0$.

6.4.3 Stability Analysis

The control law (i.e., (6.23)) and the adaptive control laws (i.e., (6.24) and (6.25)) for $t \in \Omega_t$ resemble the control techniques proposed in [79] and [69], while those for $t \notin \Omega_t$ are motivated by the control scheme proposed in [76][68]. With the proposed switching structure, the auxiliary system for $t \in [t_{1i},\ t_{2i}]$ will have an initial condition with relatively large norm (i.e., ε_1), which is desirable in [79] and [69]. Moreover, when the norm of the auxiliary signal decreases to a small constant (i.e., ε_2), input saturation need not disappear. The integra-

tion of the direct learning-control scheme proposed in [76] serves to protect the learning capability under input saturation. By properly selecting the design parameters (ε_1, ε_2 and $\xi(0)$), the proposed switching scheme is able to preserve the advantages of both control strategies. The performance of the system under the proposed control scheme is summarized in the following theorem.

Theorem 6.1: Consider the manipulator described by (6.4) satisfying Assumptions 6.1-6.3 interacts with the cellular tensegrity model described by (6.1). Provided bounded initial conditions, under the control law (6.15)(6.23) and parameter update laws (6.24)(6.25), there exist control parameters $K_1 = K_1^T > 0$, $\Lambda_f = \Lambda_f^T > 0$, $\Lambda_g = \Lambda_g^T > 0$, $\beta_f > 0$ and $\beta_g > 0$ such that the following statements hold: i) A bound of the transient tracking error can be established as indicated in (6.48); ii) During each time period when $t \in \Omega_t$ (i.e., $t_{1i} \leq t \leq t_{2i}$), tracking error e converges asymptotically to a compact set as indicated in (6.50); iii) During each time period when $t \notin \Omega_t$, modified tracking error e_1 converges asymptotically to a compact set as indicated in (6.59).

Proof: To establish the bound of the transient tracking error, we consider the following Lyapunov candidate

$$V_1^* = \frac{1}{2}e^T e + \frac{1}{2}\xi^T \xi \tag{6.26}$$

Define $\tilde{W}_f \triangleq \hat{W}_f - W_f^*$ and $\tilde{W}_g \triangleq \hat{W}_g - W_g^*$. By utilizing(6.2)-(6.12) in sequence, the time derivative of V_1^* can be expressed as

$$
\begin{aligned}
\dot{V}_1^* &= e^T(\dot{f} - \dot{f}_d) + \xi^T \dot{\xi} \\
&= e^T \hat{W}_f^T S_f(Z_f) + e^T h_g'(Z_g)\Phi(\varrho^*) - e^T \tilde{W}_f^T S_f(Z_f) \\
&\quad - e^T \tilde{W}_g^T S_g(Z_g)\Phi(\varrho^*) + e^T \epsilon_f + e^T \epsilon_g \Phi(\varrho^*) - e^T \dot{f}_d \\
&\quad + e^T \vartheta \Phi(\varrho^*) + \xi^T \dot{\xi}
\end{aligned} \tag{6.27}
$$

The rest of the proof for statement i) is presented by considering the two cases of $\dot{\xi}$ as follows.

Case 1: $\dot{\xi} = \chi_1$. Substituting (6.19) (6.23) into (6.27) yields

$$\dot{V}_1^* = -e^T K_1 e - \xi^T K_1 \xi + e^T \epsilon_f + e^T \epsilon_g \Phi(\varrho^*) + e^T \vartheta \Phi(\varrho^*)$$
$$e^T h'_g \Delta\varrho + \xi^T h'_g \Delta\varrho - e^T \tilde{W}_f^T S_f(Z_f) - e^T \tilde{W}_g^T S_g(Z_g) \qquad (6.28)$$

From Equations (6.16) and (6.21), it follows that

$$e^T \epsilon_g \Phi(\varrho^*) \ \leq \ \frac{1}{2\sigma_0}\|e\|^2 + \frac{\sigma_0 \varrho_m^2}{2}\|\epsilon_g\|^2 \qquad (6.29)$$

$$e^T \epsilon_f \ \leq \ \frac{1}{2\sigma_1}\|e\|^2 + \frac{\sigma_1}{2}\|\epsilon_f\|^2 \qquad (6.30)$$

$$e^T \vartheta \Phi(\varrho^*) \ \leq \ \frac{1}{2\sigma_2}\|e\|^2 + \frac{\sigma_2 \varrho_m^2 \nu_m^2}{2} \qquad (6.31)$$

$$e^T h'_g (\Phi(\varrho^*) - \varrho^*) \ \leq \ \frac{1}{2}\|e\|^2 + \frac{1}{2}\|h'_g \Delta\varrho\|^2 \qquad (6.32)$$

$$\xi^T h'_g (\Phi(\varrho^*) - \varrho^*) \ \leq \ \frac{1}{2}\|\xi\|^2 + \frac{1}{2}\|h'_g \Delta\varrho\|^2 \qquad (6.33)$$

where, σ_0, σ_1 and σ_2 are designed positive constants.

With above inequalities, $\dot{V}_1^*$ can be upper bounded as

$$\dot{V}_1^* \ \leq \ -e^T K_{11} e - \xi^T K_{12} \xi + \frac{\sigma_1}{2}\|\epsilon_f\|^2 + \frac{\sigma_0 \varrho_m^2}{2}\|\epsilon_g\|^2$$
$$+\frac{\sigma_2 \varrho_m^2 \nu_m^2}{2} + \|h'_g \Delta\varrho\|^2 - e^T \tilde{W}_f^T S_f(Z_f) - e^T \tilde{W}_g^T S_g(Z_g) \quad (6.34)$$

where $K_{11} = K_1 - (\frac{1}{2\sigma_0} + \frac{1}{2\sigma_1} + \frac{1}{2\sigma_2} + \frac{1}{2})I_n$ and $K_{12} = K_1 - \frac{1}{2}I_n$.

Considering the NN-weight error signals $\tilde{W}_f$ and $\tilde{W}_g$, an augmented Lyapunov function candidate is chosen as

$$V_1 = V_1^* + \frac{1}{2}\mathrm{tr}(\tilde{W}_f^T \Lambda_f^{-1} \tilde{W}_f) + \frac{1}{2}\mathrm{tr}(\tilde{W}_g^T \Lambda_g^{-1} \tilde{W}_g) \qquad (6.35)$$

Substituting (6.24) (6.25) into (6.35) and noting the facts

$$-\text{tr}(\tilde{W}_f^T \hat{W}_f) = -\frac{\|\tilde{W}_f\|^2}{2} - \frac{\|\hat{W}_f\|^2}{2} + \frac{\|W_f^*\|^2}{2} \tag{6.36}$$

$$-\text{tr}(\tilde{W}_g^T \hat{W}_g) = -\frac{\|\tilde{W}_g\|^2}{2} - \frac{\|\hat{W}_g\|^2}{2} + \frac{\|W_g^*\|^2}{2} \tag{6.37}$$

the upper bound of $\dot{V}_1$ can be rewritten as

$$\begin{aligned}
\dot{V}_1 \quad \leq \quad & -e^T K_{11} e - \xi^T K_{12} \xi + \frac{\sigma_1}{2} \|\epsilon_f\|^2 + \frac{\sigma_0 \varrho_m^2}{2} \|\epsilon_g\|^2 \\
& + \frac{\sigma_2 \varrho_m^2 \nu_m^2}{2} + \|h_g' \Delta \varrho\|^2 - \xi^T \tilde{W}_f^T S_f(Z_f) \\
& - \xi^T \tilde{W}_g^T S_g(Z_g) - \frac{\beta_f \|\tilde{W}_f\|^2}{2} - \frac{\beta_g \|\tilde{W}_g\|^2}{2} \\
& \frac{\beta_f \|W_f^*\|^2}{2} + \frac{\beta_g \|W_g^*\|^2}{2} - \frac{\beta_f \|\hat{W}_f\|^2}{2} - \frac{\beta_g \|\hat{W}_g\|^2}{2}
\end{aligned} \tag{6.38}$$

Noting $\|S_f(Z_f)\| \leq \zeta_f$ and $\|S_g(Z_g)\| \leq \zeta_g$, it follows

$$-\xi^T \tilde{W}_f^T S_f(Z_f) \leq \frac{1}{2\sigma_3} \|\xi\|^2 + \frac{\sigma_3 \zeta_f}{2} \|\tilde{W}_f\|^2 \tag{6.39}$$

$$-\xi^T \tilde{W}_g^T S_g(Z_g) \leq \frac{1}{2\sigma_4} \|\xi\|^2 + \frac{\sigma_4 \zeta_g}{2} \|\tilde{W}_g\|^2 \tag{6.40}$$

where σ_3 and σ_4 are any designed positive constants.

With above inequalities, (6.38) can be rewritten as

$$\begin{aligned}
\dot{V}_1 \quad \leq \quad & -e^T K_{11} e - \xi^T K_{13} \xi - k_f \|\tilde{W}_f\|^2 - k_g \|\tilde{W}_g\|^2 \\
& + \frac{\sigma_1}{2} \|\epsilon_f\|^2 + \frac{\sigma_0 \varrho_m^2}{2} \|\epsilon_g\|^2 + \frac{\sigma_2 \varrho_m^2 \nu_m^2}{2} + \frac{\beta_f \|W_f^*\|^2}{2} \\
& \frac{\beta_g \|W_g^*\|^2}{2} + \|h_g' \Delta \varrho\|^2 \\
\leq \quad & -\lambda_{11} V_1 + c_{11} + \|h_g' \Delta \varrho\|^2
\end{aligned} \tag{6.41}$$

where $K_{13} = K_1 - (\frac{1}{2} + \frac{1}{2\sigma_3} + \frac{1}{2\sigma_4}) I_n$, $k_f = \frac{1}{2}(\beta_f - \sigma_3 \zeta_f)$, $k_g = \frac{1}{2}(\beta_g - \sigma_4 \zeta_g)$,

$\lambda_{11} \triangleq \min\{2\lambda_{min}(K_{11}), 2\lambda_{min}(K_{13}), \frac{k_f}{\lambda_{max}(\Lambda_f^{-1})}, \frac{k_g}{\lambda_{max}(\Lambda_g^{-1})}\}, c_{11} \triangleq \frac{1}{2}(\sigma_1\|\epsilon_f\|^2 + \sigma_0\varrho_m^2\|\epsilon_g\|^2 + \sigma_2\varrho_m^2\nu_m^2 + \beta_f\|W_f^*\|^2 + \beta_g\|W_g^*\|^2)$.

Case 2: $\dot{\xi} = \chi_2$. Substituting (6.19) into (6.27) yields

$$
\begin{aligned}
\dot{V}_1^* &= e^T\hat{W}_f^T S_f(Z_f) + e^T h_g'(Z_g)\Phi(\varrho^*) + e^T\vartheta\Phi(\varrho^*) + e^T\epsilon_f \\
&\quad -e^T\tilde{W}_f^T S_f(Z_f) - e^T\tilde{W}_g^T S_g(Z_g)\Phi(\varrho^*) + e^T\epsilon_g\Phi(\varrho^*) \\
&\quad -\xi^T(K_1 - \frac{1}{2}I_n)\xi - \frac{1}{2}\|e^T K_1\|^2 - |e^T h_g'\Delta\varrho| \\
&\quad -|e^T\vartheta\Phi(\varrho^*)| - \frac{1}{2}\|e\|^2\|\Phi(\varrho^*)\|^2 - \frac{1}{2}\|h_g'\Delta\varrho\|^2 \\
&\quad -\frac{1}{2}\|\xi\|^2 + \xi^T h_g'(Z_g)(\varrho^* - \Phi(\varrho^*)) - e^T\dot{f}_d \quad (6.42)
\end{aligned}
$$

Considering (6.23)(6.27) (6.30) and the following facts:

$$
e^T K_1\xi \leq \frac{1}{2}\|e^T K_1\|^2 + \frac{1}{2}\|\xi\|^2 \quad (6.43)
$$

$$
e^T\epsilon_g\Phi(\varrho^*) \leq \frac{1}{2}\|\epsilon_g\|^2 + \frac{1}{2}\|e\|^2\|\Phi(\varrho^*)\|^2 \quad (6.44)
$$

$\dot{V}_1^*$ can be upper bounded as

$$
\begin{aligned}
\dot{V}_1^* &\leq -e^T K_{14}e - \xi^T K_{15}\xi - e^T\tilde{W}_f^T S_f(Z_f) \\
&\quad -e^T\tilde{W}_g^T S_g(Z_g)\Phi(\varrho^*) + \frac{\sigma_1}{2}\|\epsilon_f\|^2 + \frac{1}{2}\|\epsilon_g\|^2 \quad (6.45)
\end{aligned}
$$

where $K_{14} = K_1 - \frac{1}{2\sigma_1}I_n$ and $K_{15} = K_1 - I_n$.

Substituting (6.24) (6.25)(6.36)(6.37) and (6.45) into the augmented Lyapunov

function (6.35), $\dot{V}_1$ is upper bounded as

$$
\begin{aligned}
\dot{V}_1 \quad \leq \quad & -e^T K_{14} e - \xi^T K_{15} \xi - \frac{\beta_f \|\tilde{W}_f\|^2}{2} - \frac{\beta_g \|\tilde{W}_g\|^2}{2} \\
& + \frac{\beta_f \|W_f^*\|^2}{2} + \frac{\beta_g \|W_g^*\|^2}{2} + \frac{\sigma_1}{2} \|\epsilon_f\|^2 + \frac{1}{2} \|\epsilon_g\|^2 \\
& - \frac{\beta_f \|\hat{W}_f\|^2}{2} - \frac{\beta_g \|\hat{W}_g\|^2}{2} \\
\leq \quad & -\lambda_{12} V_1 + c_{12} \quad\quad\quad\quad\quad\quad\quad\quad\quad\quad (6.46)
\end{aligned}
$$

where $\lambda_{12} = \min \left\{ 2\lambda_{min}(K_{14}), 2\lambda_{min}(K_{15}), \frac{\beta_f}{\lambda_{max}(\Lambda_f^{-1})}, \frac{\beta_g}{\lambda_{max}(\Lambda_g^{-1})} \right\}$ and $c_{12} = \frac{1}{2}(\sigma_1 \|\epsilon_f\|^2 + \|\epsilon_g\|^2 + \beta_f \|W_f^*\|^2 + \beta_g \|W_g^*\|^2)$.

For $t \in [0, +\infty]$, to ensure $\lambda_{11}, \lambda_{12}, c_{11}, c_{12} > 0$, the sufficient gain conditions are: $K_1 - (\frac{1}{2} + \frac{1}{2\sigma_0} + \frac{1}{2\sigma_1} + \frac{1}{2\sigma_2} + \frac{1}{2\sigma_3} + \frac{1}{2\sigma_4}) > 0$, $\beta_f - \sigma_3 \zeta_f > 0$, $\beta_g - \sigma_4 \zeta_g > 0$. σ_0 is chosen such that $\frac{\sigma_0 \varrho_m^2}{2} \geq 1$. Noting $\lambda_{11} \leq \lambda_{12}$ and $c_{11} \geq c_{12}$, it is obtained that

$$
\dot{V}_1 \leq -\lambda_{11} V_1 + c_{11} + \|h_g' \Delta \varrho\|^2 \quad \text{for} \quad t \in [0, +\infty] \quad\quad (6.47)
$$

According to Lemma 1.2 in [52], (6.47) indicates that a transient bound of e can be established as

$$
\|e(t)\| \leq \sqrt{2(V_1(0) + \frac{c_{11}}{\lambda_{11}} + \frac{1}{\lambda_{11}} \sup_{\tau \in [0,t]} [\|h_g' \Delta \varrho(\tau)\|^2])} \quad\quad (6.48)
$$

where $V_1(0) = (1/2)e^T(0)e(0) + (1/2)\xi^T(0)\xi(0) + (1/2)\tilde{W}_f^T(0)\Lambda_f^{-1}\tilde{W}_f(0) + (1/2)\tilde{W}_g^T(0)\Lambda_g^{-1}\tilde{W}_g(0)$. This concludes the proof of statement i).

Note that the analysis for case 2 applies for $t \in [t_{1i}, t_{2i}]$, i.e.,

$$
\dot{V}_1 \leq -\lambda_{12} V_1 + c_{12} \quad \text{for} \quad t \in [t_{1i}, t_{2i}] \qu\quad\quad (6.49)
$$

(6.49) indicates that tracking error e exponentially converges to a compact set

and the transient error bound is given by

$$\|e\| \leq \sqrt{2(V_1(t_{1i}) + c_{12}/\lambda_{12})} \tag{6.50}$$

Noting that $\lambda_{12} \geq \lambda_{11}$ and $c_{12} \leq c_{11}$, if the time period $[t_{1i}, \ t_{2i}]$ is long enough, it is possible that a good tracking performance is achieved. This concludes the proof of statement ii).

The control performance for $t \notin \Omega_t$ is further discussed by considering the following Lyapunov function

$$V_2^* = \frac{1}{2}e_1^T e_1 \tag{6.51}$$

Without loss of generality, we assume that $M \geq 2$ and $\xi(0) < \varepsilon_1$. In this case, noting (6.5)-(6.10), the time derivative of V_2^* for $t \in [0, \ t_{11}]$ can be expressed as

$$\begin{aligned}
\dot{V}_2^* &= e_1^T(\dot{e} - \dot{\xi}) \\
&= e_1^T \hat{W}_f^T S_f(Z_f) + e_1^T h_g'(Z_g)\Phi(\varrho^*) - e_1^T \tilde{W}_f^T S_f(Z_f) \\
&\quad - e_1^T \tilde{W}_g^T S_g(Z_g)\Phi(\varrho^*) + e_1^T \epsilon_f + e_1^T \epsilon_g \Phi(\varrho^*) - e_1^T \dot{f}_d \\
&\quad + e_1^T \vartheta \Phi(\varrho^*) - e_1^T \dot{\xi} \tag{6.52}
\end{aligned}$$

From Equations (6.16) and (6.21), it follows that

$$e_1^T \epsilon_f \leq \frac{1}{2\sigma_1}\|e_1\|^2 + \frac{\sigma_1}{2}\|\epsilon_f\|^2 \tag{6.53}$$

$$e_1^T \epsilon_g \Phi(\varrho^*) \leq \frac{\varrho_m^2}{2}\|\epsilon_g\|^2 + \frac{1}{2}\|e_1\|^2 \tag{6.54}$$

$$e_1^T \vartheta \Phi(\varrho^*) \leq \frac{\sigma_2 \varrho_m^2 \nu_m^2}{2} + \frac{1}{2\sigma_2}\|e_1\|^2 \tag{6.55}$$

With above inequalities, $\dot{V}_2^*$ can be upper bounded as

$$\dot{V}_2^* \leq -e_1^T K_{16} e_1 - e_1^T \tilde{W}_f^T S_f(Z_f) - e_1^T \tilde{W}_g^T S_g(Z_g) \Phi(\varrho^*)$$
$$+ \frac{\sigma_2 \varrho_m^2 \nu_m^2}{2} + \frac{\sigma_1}{2} \|\epsilon_f\|^2 + \frac{\varrho_m^2}{2} \|\epsilon_g\|^2 \qquad (6.56)$$

where $K_{16} = K_1 - (\frac{1}{2\sigma_1} + \frac{1}{2\sigma_2} + \frac{1}{2}) I_n > 0$.

Considering the NN-weight error signals $\tilde{W}_f$ and $\tilde{W}_g$, an augmented Lyapunov function candidate is chosen as

$$V_2 = V_2^* + \frac{1}{2} \text{tr}(\tilde{W}_f^T \Lambda_f^{-1} \tilde{W}_f) + \frac{1}{2} \text{tr}(\tilde{W}_g^T \Lambda_g^{-1} \tilde{W}_g) \qquad (6.57)$$

Substituting (6.24) (6.25)(6.36)(6.37) (6.56) into (6.57) yields

$$\dot{V}_2 \leq -\lambda_2 V_2 + c_2 \qquad (6.58)$$

where $\lambda_2 = \min \left\{ 2\lambda_{min}(K_{16}), \frac{\beta_f}{\lambda_{max}(\Lambda_f^{-1})}, \frac{\beta_g}{\lambda_{max}(\Lambda_g^{-1})} \right\}$ and $c_2 = \frac{1}{2}(\sigma_2 \varrho_m^2 \nu_m^2 + \sigma_1 \|\epsilon_f\|^2 + u_m^2 \|\epsilon_g\|^2 + \beta_f \|W_f^*\|^2)$.

Provided bounded initial condition, (6.58) indicates

$$\|e_1\| \leq \sqrt{2(V_2(0) + c_2/\lambda_2)} \qquad (6.59)$$

Furthermore, noticing that the analysis is conducted under the condition that $\|\xi\| < \varepsilon_1$, we obtain

$$\|e\| \leq \|e_1\| + \|\xi\| < \sqrt{2(V_2(0) + c_2/\lambda_2)} + \varepsilon_1 \qquad (6.60)$$

The analysis for $t \in [t_{2i}, \ t_{1(i+1)}] \cup [t_{2Q}, \ +\infty](i = 1, ..., Q - 1)$ is similar as above. Moreover, if Q is assumed to satisfy $Q \leq d < +\infty$ where d is any positive integer, an explicit bound of tracking error e during $t \in [t_{2i}, \ t_{1(i+1)}]$ can

be found by repeating the above analysis. This concludes the proof of statement iii). □

Remark 6.3: If the artificial bounds of control input magnitude and rate are chosen to be large or the desired force f_d is chosen to be small, there is possibility that $\Phi(\varrho^*) - \varrho^* = \Delta\varrho = 0$ for all t. In this case, $\xi(t) = 0$ for $t \in [0, +\infty]$ if the initial condition is chosen as $\xi(0) = 0$. Hence, $e(t) = e_1(t)$ and $\lim_{t \to \infty} \|e\| = \lim_{t \to \infty} \|e_1\|$. Furthermore, if $\Delta\varrho$ does not remain zero while $\lim_{t \to \infty} \|\Delta\varrho\| = 0$, it can be deduced that $\lim_{t \to \infty} \xi(t) = 0$. This implies that $\lim_{t \to \infty} \|e\| = \lim_{t \to \infty} \|e_1\|$. It is worth pointing out that no assumption of a square integrable minimum approximation as in [68] is made and thus the analysis and results are different from therein. □

Remark 6.4: Proper selection of $\xi(0)$, ε_1 and ε_2 may further improve the control performance in the presence of input saturations. For NN-based adaptive controllers, input saturation may only occur in the initial stage of control when the NN weights have not been well tuned. As such, if choosing $\xi(0) = \varepsilon_1$ (i.e., $t_{11} = 0$) with suitable ε_1 and ε_2, it is possible that input saturation disappears before t_{21} and does not occur afterwards. In this case, as indicated in Equation (6.46), the tracking error converges exponentially to a compact set. Moreover, during the entire process (i.e., $t \in [0, +\infty]$), the tracking performance is guaranteed despite the uncertainties and input saturation. It is worth pointing out that requiring $\|\xi(0)\| \leq \varepsilon_1$ is not necessary. In fact, $\|\xi(0)\| > \varepsilon_1$ can be chosen and it can be treated in the same way as $\|\xi(0)\| = \varepsilon_1$. Notice that in this case t_{11} is defined as 0 instead of the time instant when $\|\xi\| = \varepsilon_1$ for the first time. □

Remark 6.5: Although (6.17) is obtained based on the assumption that the dynamics of manipulator is exactly known, the uncertainties of the manipulator dynamics can be compensated by the uncertainties of the contact force model

112

and therefore assumption 1 can be relaxed. □

6.5 Numerical Simulation

To demonstrate the effectiveness of the proposed force control law, numerical simulations have been conducted. It is considered that applied force is exerted on point G of $B_1 D_1$ where $r = 0.75L$. The mechanical properties of the cellular tensegrity model are assumed as follows: $L = 10\mu m$, $k = 100pN$, $c = 100pN\,s/\mu m$. The prestress P is assumed to be 2. The basis tensions T_0 at reference solution are set the same values as in Chapter 4. The desired force trajectory is defined as $f_d = [f_{dx}\ f_{dy}\ f_{dz}]^T$ (as shown in Figure 6.2) with

$$f_{dx} = f_{dy} = 10pN \tag{6.61}$$

$$f_{dz} = -20 + 5\sin(\pi t)pN \tag{6.62}$$
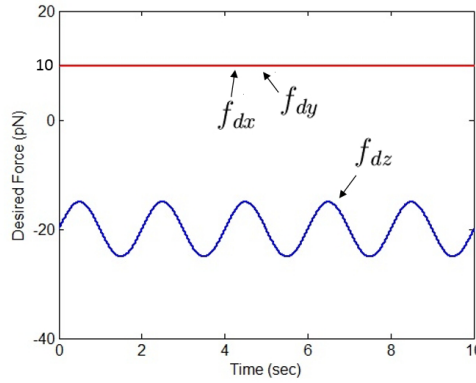
Figure 6.2: Desired force trajectory

In the simulation, the design parameters are chosen as $\nu = 0.05$, $K_1 = \text{diag}\{20\}$, $\Gamma_f = \Gamma_g = \text{diag}\{0.25\}$, $\beta_f = \beta_g = 2$, $\varepsilon_1 = 0.1$, $\varepsilon_2 = 0.01$ and $\xi(0) = 0$. The parameters for Φ are designed as $\varrho_{i\ max} = 0.3$, $\varrho_{i\ min} = -0.3$, $\dot{\Phi}(\varrho_{i\ max}) = 3$, $\dot{\Phi}(\varrho_{i\ min}) = -3$ and $\omega_i = 20(i = 1, 2, 3)$. One hundred nodes are employed for

estimating h_f and h_g, i.e., $L_1 = L_2 = 200$.
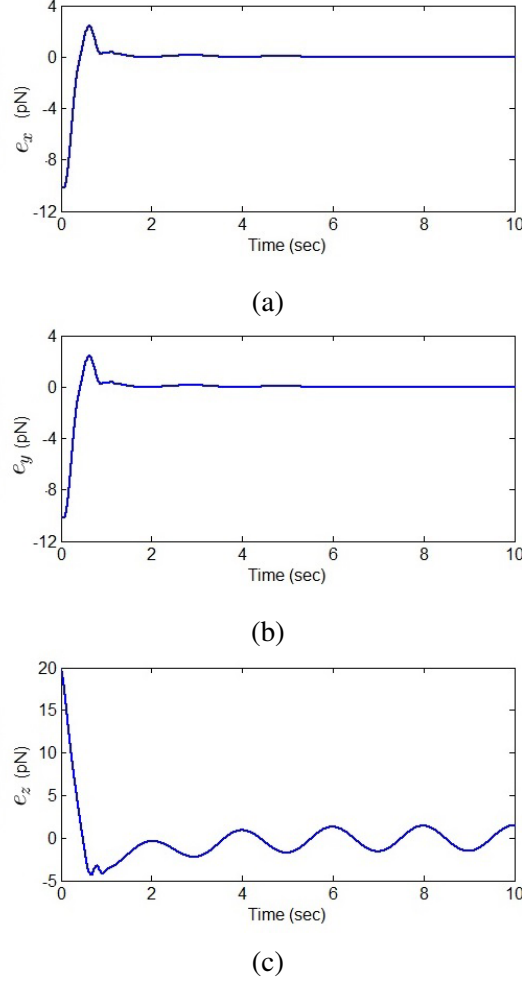
Figure 6.3: Force tracking error: (a) e_x. (b) e_y. (c) e_z.

The tracking error $e = [e_x \; e_y \; e_z]^T$, as shown in Figure 6.3 , demonstrates that the contact force follows the desired force trajectory with a small error in despite of the system uncertainties. Figure 6.4 and Figure 6.5 show the trajectory of $\Phi(\varrho^*)$ and $\dot{\Phi}(\varrho^*)$, respectively. It is noticed that the saturation in both $\Phi(\varrho^*)$ and $\dot{\Phi}(\varrho^*)$ occur in the transient phase of the control process. The auxiliary system signal ξ is shown in terms of its norm in Figure 6.6. It can be concluded that ξ works as designed. These simulation results demonstrate that the control objective is achieved with satisfactory tracking performance observed. It is worth pointing out that in simulations the bound on the rate will also affect when and how the

input saturation in magnitude occurs. For instance, if the bound on the rate is chosen sufficiently small, there is a possibility that saturation in magnitude does not occur at all. Therefore, with different sets of bounds on input magnitude and rate, the control performance will vary.

(a)

(b)

(c)
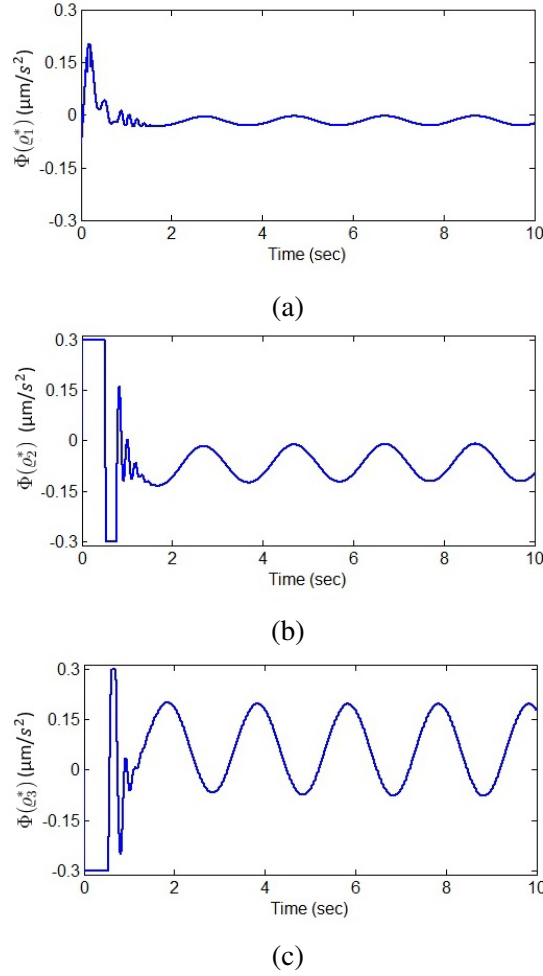
Figure 6.4: (a) $\Phi(\varrho_1^*)$. (b) $\Phi(\varrho_2^*)$. (c) $\Phi(\varrho_3^*)$.

6.6   Conclusions

This chapter presents the development of an adaptive NN based force control algorithm for achieving foce tracking in biomanipulation tasks based on a well ac-
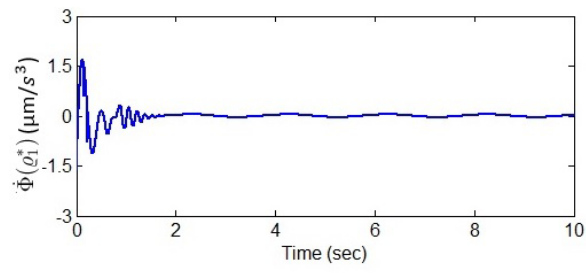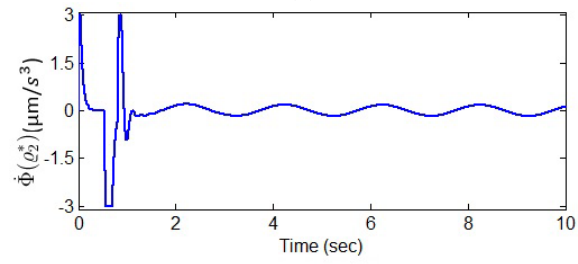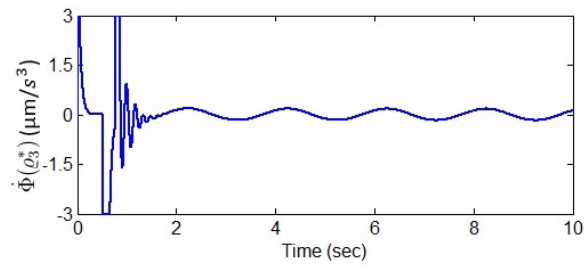
Figure 6.5: (a) $\dot{\Phi}(\varrho_1^*)$. (b) $\dot{\Phi}(\varrho_2^*)$. (c) $\dot{\Phi}(\varrho_1^*)$.

cepted cellular tensegrity model constructed using structural method. Although the controller is discussed within the context of cellular tensegrity, the proposed controller is not limited to the tensegrity model but can be applied for the control of interaction force between robot and the nonlinear viscoelastic environment which is often encountered in biomanipulation.
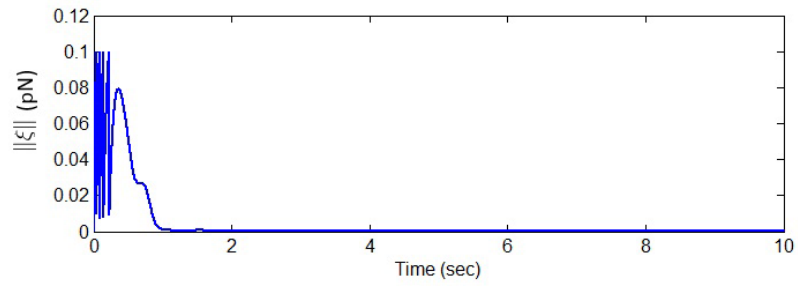
Figure 6.6: Norm of ξ

Chapter 7

Conclusions

7.1 Summary

The overall objective of this work involves the improvement and optimisation of biomanipulation systems. Two main issues which are critical to further enhancing the capability of fully automated biomanipulation systems have been explored. The first issue was to design an optimal speed trajectory for microinjection process, which is a common biomanipulation task, in order to minimize the damage induced by injection process. The second issue was to design control algorithms for general automated biomanipulation systems to enable accurate force control on living cells or other similar biological materials/structures. In particular, the cellular tensegrity model from structure approach was employed for the force control development.

In Chapter 3, the problem of optimizing the microinjection speed of zebrafish embryos in terms of minimizing the deformation sustained by the embryo during the indentation process was investigated. A systematic approach was proposed for solving this problem by synthesizing an optimal speed trajectory for the

micropipette. Numerical simulations and extensive experiments were conducted to demonstrate the effectiveness of the proposed approach.

Chapter 4 to Chapter 6 are dedicated to the development of force control based on a well-accepted tensegrity model under different task settings. In chapter 4, a homogenous tensegrity model and a robust force control algorithm was proposed as the first step to control a cellular tensegrity model in presence of model uncertainties and partial measurability. In Chapter 5, a heterogenous tensegrity model with time-varying mechanical properties was proposed. This heterogenous model was shown to be more capable in describing the mechanical behavior of biological materials/structures. The time-varying mechanical properties were introduced to simulate the variance of mechanical properties of biological materials/structures caused by external force induced biological responses. A robust adaptive control was developed through backstepping design to handle the uncertainties due to the time-varying feature. In Chapter 6, based on the same homogeneous tensegrity model as in Chapter 4, a novel adaptive NN-based controller was proposed based on the six-strut cellular tensegrity structure. Thanks to the nature of NN-based estimation, the proposed force controller is readily applicable for the control problem concerning manipulator interacting with soft compliant material which exhibits viscoelasticity. In particular, a special control technique which aimed at improving the NN-based adaptive controller was developed and this technique is applicable for tracking control of MIMO systems with input constraints on both magnitude and rate. For all the proposed controllers under different task settings, simulations were conducted to validate their effectiveness.

7.2 Contribution

The contribution of this thesis is summarized as follows:

119

1. *Speed optimization in biomanipulation*

   The formulation of the speed optimization problem and the proposed solution represent a meaningful initial step in the development of sophisticated approaches for improving the performance of automated microinjection. To the best of our knowledge, this is the pioneering work devoted to reducing the detrimental physical effects induced by micropipette through an analytical approach rather than empirical approach. Based on the proposed two-arm Maxwell-Weichert model and its associated assumptions, minimizing the deformation of cell in the injection process is explicitly targeted. Results from numerical simulation and experiments presented clearly demonstrate the effectiveness of the proposed solution. A broader implication of this line of research is that, although the analysis reported in this section uses zebrafish embryo as a specific environment upon which force is applied, the method employed in the analysis can be readily extended to deal with the general problem of optimizing the localized force-bearing interaction between a manipulator and a viscoelastic environment in micro/macro-manipulation.

2. *Cellular tensegrity model based force control technique in biomanipulation*

   The reported cellular tensegrity model based force control is the first attempt to examine the interaction process between end-effector and living cells through a mechanical model derived from the structural approach. A key feature of cellular tensegrity model is that it considers cytoskeleton as the central role in governing cellular mechanical response rather than deems the living cell as a viscous fluid comprised by a membrane. Leveraging on the more comprehensive description of the nonlinearity and dynamic coupling of internal structural elements provided by this

tensegrity model, both homogeneous and heterogeneous cellular tensegrity models are discussed with the objective of achieving delicate force control in biomanipulation. The force control techniques proposed based on these models can be used to fully realize the potential of the many advanced micro/nano engineering platforms in terms of enabling accurate control of mechanical stimuli, which will greatly facilitate the mechanobiology study on how cells are influenced by external mechanical stimuli. Another contribution of this work is that the results can be utilized to improve the automatic manipulation of cells such as automated microinjection process. With the proposed force control algorithm, the reliability and dexterity of the automated biomanipulation systems for manipulating cells can be enhanced. Moreover, the proposed control techniques in Chapter 4 and Chapter 5 can be readily extended to a general class of MIMO systems. Furthermore, the proposed auxiliary system in Chapter 6 can be applied for a class of uncertain nonlinear MIMO systems to guarantee the control performance in the presence of input saturation in both magnitude and rate.

7.3 Future Work

For the study of speed optimization in microinjection process, some potential areas for further investigation may include:

- In the Maxwell-Wiechert model developed, the depth of indentation is the only variable used to describe the deformation of the embryos whilst other variables which also contribute to the deformation are all neglected. Further study is needed to develop more sophisticated models that integrate various other factors that affect the microinjection process should be studied for the selection of optimal speed in order to obtain a more

comprehensive solution.

- In the numerical solution, the form of the speed trajectory is predefined to be polynomials. Although it may be argued that such a practice is common in the manipulator trajectory-planning literature and that it is possible to approximate a continuous function by using a suitable polynomial, the question of whether there exist other forms of speed trajectory suitable for the same purpose remains to be further explored.

- The optimization problem formulated assumes that the optimal speed will be implemented (on an actual automated microinjection system) exactly as designed. This assumption is not realistic since tracking error always exists in such a dynamical system. To address this problem, an improved optimization formulation should take this speed tracking error into account, by considering the capability of the hardware and software components used in the automated microinjection system.

For the study of cellular tensegrity model base force control for biomanipulation purpose, considering that the research in this area is still at an less developed stage, the following aspects are recommended for future research.

- To consider the uncertainties of manipulators in the development of force controller. Uncertainties of manipulators are often encountered in force control problems and it may significantly affect the performance of the proposed force controller which are based on the assumption that the dynamics of the manipulators are exactly known.

- To integrate mechanical contribution from other cellular components(e.g. cytoplasm and nucleus) with the objective of constituting a more complete model for force control. The incorporation of these components could strengthen the tensegrity model since their impact on mechanical response may be significant under large deformation

122

Bibliography

[1] J.-C. Wang and B. Thampatty, "An introductory review of cell mechanobiology," *Biomechanics and Modeling in Mechanobiology*, vol. 5, pp. 1–16, 2006.

[2] H. Ladjal, J.-L. Hanus, and A. Ferreira, "Interactive cell injection simulation based on 3d biomechanical tensegrity model," in *Proceedings of IEEE/RSJ International Conference on Intelligent Robots and Systems*, Piscataway, NJ, USA, 2008, pp. 2296 – 2302.

[3] P. Kallio and J. Kuncova, "Capillary pressure microinjection of living adherent cells: challenges in automation," *Journal of Micromechatronics*, vol. 3, no. 3-4, pp. 189 – 220, 2006.

[4] Y. Sun and B. J. Nelson, "Biological cell injection using an autonomous microrobotic system," *International Journal of Robotics Research*, vol. 21, no. 10-11, pp. 861–868, 2002.

[5] Z. Lu, P. Chen, J. Nam, R. Ge, and W. Lin, "A micromanipulation system with dynamic force-feedback for automatic batch microinjection," *Journal of Micromechanics and Microengineering*, vol. 17, no. 2, pp. 314–321, 2007.

[6] W. Wang, X. Liu, and Y. Sun, "High-throughput automated injection of

individual biological cells," *IEEE Transactions on Automation Science and Engineering*, vol. 6, no. 2, pp. 209–219, 2009.

[7] H. Huang, D. Sun, J. Mills, and S. H. Cheng, "Robotic cell injection system with position and force control: Toward automatic batch biomanipulation," *IEEE Transactions on Robotics*, vol. 25, no. 3, pp. 727–737, 2009.

[8] Y. Sun, B. Nelson, P. Potasek, and E. Enikov, "A bulk microfabricated multi-axis capacitive cellular force sensor using transverse comb drives," *Journal of Micromechanics and Microengineering*, vol. 12, no. 6, p. 832, 2002.

[9] H. Huang, D. Sun, J. Mills, and S. Cheng, "Automatic suspended cell injection under vision and force control biomanipulation," in *IEEE International Conference on Robotics and Biomimetics*, 2007, pp. 71–76.

[10] Y. Xie, D. Sun, H. Tse, C. Liu, and S. Cheng, "Force sensing and manipulation strategy in robot-assisted microinjection on zebrafish embryos," *IEEE/ASME Transactions on Mechatronics*, vol. 16, no. 6, pp. 1002–1010, 2011.

[11] X. Liu, K. Kim, Y. Zhang, and Y. Sun, "Nanonewton force sensing and control in microrobotic cell manipulation," *The International Journal of Robotics Research*, vol. 28, pp. 1065–1076, 2009.

[12] F. Arai, K. Morishima, T. Kasugai, and T. Fukuda, "Biomicromanipulation (new direction for operation improvement)," in *Proceedings of the IEEE/RSJ International Conference on Intelligent Robots and Systems*, vol. 3, 1997, pp. 1300–1305.

[13] H. uang, D. Sun, J. K. Mills, W. J. Li, and S. H. Cheng, "Visual-based impedance control of out-of-plane cell injection systems," *IEEE Transac-*

tions on Automation Science and Engineering, vol. 6, no. 3, pp. 565–571, 2007.

[14] J. P. Desai, A. Pillarisetti, and A. D. Brooks, "Engineering approaches to iomanipulation," *Annual Review of Biomedical Engineering*, vol. 9, pp. 35 – 53, 2007.

[15] M. Westerfield, *The zebrafish book: guide for the laboratory use of zebrafish (Danio rerio)*, 4th ed. Eugene, OR: University of Oregon Press, 2000.

[16] M. Ammi and A. Ferreira, "Biological cell injection visual and haptic interface," *Advanced Robotics*, vol. 20, no. 3, pp. 283 – 304, 2006.

[17] A. Pillarisetti, M. Pekarev, A. D. Brooks, and J. P. Desai, "Evaluating the effect of force feedback in cell injection," *IEEE Transactions on Automation Science and Engineering*, vol. 4, no. 3, pp. 322 – 331, 2007.

[18] W. Wang, X. Liu, D. Gelinas, B. Ciruna, and Y. Sun, "A fully automated robotic system for microinjection of zebrafish embryos," *PLoS ONE*, vol. 2, no. 9, p. e862, 2007.

[19] C. Elbuken, M. Khamesee, and M. Yavuz, "Design and implementation of a micromanipulation system using a magnetically levitated mems robot," *IEEE/ASME Transactions on Mechatronics*, vol. 14, no. 4, pp. 434 –445, 2009.

[20] D. Ingber, "Mechanobiology and diseases of mechanotransduction," *Annals of Medicine*, vol. 35, pp. 564–577, 2003.

[21] D.-H. Kim, K. W. Pak, J. Park, A. Levchenko, and Y. Sun, "Microengineered platforms for cell mechanobiology," *Annual Review of Biomedical Engineering*, vol. 11, pp. 203–233, 2009.

[22] R. Skelton, R. Adhikari, J.-P. Pinaud, W. Chan, and J. Helton, "An introduction to the mechanics of tensegrity structures," in *Proceedings of the 40th IEEE Conference on Decision and Control*, vol. 5, 2001, pp. 4254–4259.

[23] R. E. Skelton, J. P. Pinaud, and D. Mingori, "Dynamics of the shell class of tensegrity structures," *Journal of the Franklin Institute*, vol. 338, no. 2-3, pp. 255 – 320, 2001.

[24] C. Sultan and R. T. Skelton, "Force and torque smart tensegrity sensor," in *SPIE 5th Symposium on Smart Structures and Materials*, vol. 3323, 1998, pp. 357–368.

[25] P. Kallio, T. Ritala, M. Lukkari, and S. Kuikka, "Injection guidance system for cellular microinjections," *International Journal of Robotics Research*, vol. 26, no. 11-12, pp. 1303 – 13, 2007.

[26] K. Kim, X. Liu, Y. Zhang, and Y. Sun, "Nanonewton force-controlled manipulation of biological cells using a monolithic mems microgripper with two-axis force feedback," *Journal of Micromechanics and Microengineering*, vol. 18, no. 5, p. 055013, 2008.

[27] Y. Xie, "Study on robot-assisted microinjections on zebrafish embryos: Micro force measurement and control," *PhD thesis*, 2010.

[28] U. Wejinya, Y. Shen, N. Xi, and F. Salem, "Force measurement of embryonic system using in situ pvdf piezoelectric sensor," in *IEEE International Midwest Symposium on Circuits and Systems*, vol. 1, 2006, pp. 108–112.

[29] Z. Lu, P. C. Y. Chen, and W. Lin, "Force sensing and control in micromanipulation," *IEEE Transactions on Systems, Man, and Cybernetics, Part C: Applications and Reviews*, vol. 36, no. 6, pp. 713–724, 2006.

[30] D. Cappelleri, G. Piazza, and V. Kumar, "Two-dimensional, vision-based

μn force sensor for microrobotics," in *IEEE International Conference on Robotics and Automation*, 2009, pp. 1016–1021.

[31] G. Zeng and A. Hemami, "An overview of robot force control," *Robotica*, vol. 15, pp. 473–482, 1997.

[32] S. Chiaverini, B. Siciliano, and L. Villani, "A survey of robot interaction control schemes with experimental comparison," *IEEE/ASME Transactions on Mechatronics*, vol. 4, no. 3, pp. 273–285, 1999.

[33] M. Raibert and C. J.J., "Hybrid position/force control of mnipulators," *Journal of Dynamical systems, Measurement, and Control*, vol. 103, no. 2, 1981.

[34] N. Hogan, "Impedance control: an approach to manipulation: Part i, ii, iii," *Journal of Dynamical systems, Measurement, and Control*, vol. 107, pp. 1–16, 1985.

[35] B. Siciliano and L. Viilani, *Robot Force Control.* Dordrecht: Kluwer Academic Publisher, 2000.

[36] H. Seraji and R. Colbaugh, *Force Tracking in Impedance Control*, vol. 16, pp. 97–117, 1997.

[37] R. Carelli, R. Kelly, and R. Ortega, *Adaptive force control of robot manipulators*, vol. 44, pp. 792–802, 1990.

[38] J. Nam, P. Chen, Z. Lu, H. Luo, R. Ge, and W. Lin, "Force control for mechanotransduction of impedance variation in cellular organisms," *Journal ofMicromechanics and Microengineering*, vol. 20, 2010.

[39] Y. Xie, D. Sun, C. Liu, H. Y. Tse, and S. H. Cheng, "A force control approach to a robot-assisted cell microinjection system," *The International Journal of Robotics Research*, vol. 29, pp. 1222–1232, 2010.

[40] C. Lim, E. Zhou, and S. Quek, "Mechanical models for living cells - a review," *Journal of Biomechanics*, vol. 39, no. 2, pp. 195 – 216, 2006.

[41] D. Stamenovic and D. E. Ingber, "Models of cytoskeletal mechanics of adherent cells," *Biomechanics and Modeling in Mechanobiology*, vol. 1, no. 1, pp. 95–108, 2002.

[42] D. E. Ingber, "Cellular tensegrity: defining new rules of biological design that govern the cytoskeleton," *Journal of Cell Science*, vol. 104, pp. 613 – 627, 1993.

[43] ——, "Tensegrity: the architectural basis of cellular mechanotransduction," *Annual Review of Physiology*, vol. 59, pp. 575–599, 1997.

[44] ——, "Tensegrity-based mechanosensing from macro to micro," *Progress in biophysics and molecular biology*, vol. 97, pp. 163–179, 1997.

[45] N. Wang, K. Naruse, D. Stamenovic, J. J. Fredberg, S. M. Mijailovich, I. M. Tolic-Nrrelykke, T. Polte, R. Mannix, and D. E. Ingber, "Proceedings of mechanical behavior in living cells consistent with the tensegrity model," in *Proceedings of National Academy of Sciences*, vol. 98, no. 14, 2001, pp. 7765–7770.

[46] P. Canadas, S. Wendling-Mansuy, and D. Isabey, "Frequency response of a viscoelastic tensegrity model: structural rearrangement contribution to cell dynamics," *Transactions of the ASME. Journal of Biomechanical Engineering*, vol. 128, no. 4, pp. 487 – 495, 2006.

[47] C. Sultan, D. Stamenovic, and D. Ingber, "A computational tensegrity model predicts dynamic rheological behaviors in living cells," *Annals of Biomedical Engineering*, vol. 32, no. 4, pp. 520 – 530, 2004.

[48] D. Stamenovic, J. J. Fredberg, N. Wang, J. P. Butler, and D. E. Ingber, "A

quantitative model of cellular elasticity based on tensegrity," *Journal of Biomechanical Engineering*, vol. 122, pp. 39–43, 2000.

[49] C. Sultan, M. Corless, and R. E. Skelton, "The prestressability problem of tensegrity structures. some analytical solutions," *International Journal of Solids Structure*, vol. 38, pp. 5223–5252, 2001.

[50] J. G. McGarry and P. J. Prendergast, "A three-dimensional finite element model of an adherent eukaryotic cell," *Eur Cell Mater*, vol. 7, pp. 27 – 33, 2004.

[51] J. Bursa and V. Fuis, "Finite element simulation of mechanical tests of individual cells," in *Proceedings of International Federation for Medical and Biological Engineering (IFMBE)*, vol. 25, no. 10, 2009, pp. 16 – 19.

[52] S. S. Ge and C. Wang, "Adaptive neural control of uncertain mimo nonlinear systems," *IEEE Transactions on Neural Network*, vol. 15, no. 3, pp. 674–692, 2004.

[53] H. Elmali and N. Olgac, "Robust output tracking control of nonlinear mimo systems via sliding mode technique," *Automatica*, vol. 28, no. 1, pp. 145–151, 1992.

[54] Y.-C. Chang, "Robust tracking control for nonlinear mimo systems via fuzzy approaches," *Automatica*, vol. 36, no. 10, pp. 1535 – 1545, 2000.

[55] S. Ge, C.-C. Hang, and T. Zhang, "Stable adaptive control for nonlinear multivariable systems with a triangular control structure," *IEEE Transactions on Automatic Control*, vol. 45, no. 6, pp. 1221–1225, 2000.

[56] B. Yao and M. Tomizuka, "Adaptive robust control of mimo nonlinear systems in semi-strict feedback forms," *Automatica*, vol. 37, no. 9, pp. 1305 – 1321, 2001.

[57] W. M. Haddad, T. Hayakawa, and V. Chellaboina, "Robust adaptive control for nonlinear uncertain systems," *Automatica*, vol. 39, no. 3, pp. 551 – 556, 2003.

[58] R. R. Costa, L. Hsu, A. K. Imai, and P. Kokotovic, "Lyapunov-based adaptive control of mimo systems," *Automatica*, vol. 39, no. 7, pp. 1251–1257, 2003.

[59] S. S. Ge, "Advanced control techniques of robotic manipulators," in *Proceedings of the American Control Conference*, vol. 4, June 1998, pp. 2185–2199.

[60] C. Kwan and F. L. Lewis, "Robust backstepping control of nonlinear systems using neural networks," *IEEE Transactions on Systems, Man and Cybernetics, Part A: Systems and Humans*, vol. 30, no. 6, pp. 753–766, 2000.

[61] S. S. Ge, G. Y. Li, J. Zhang, and T. Lee, "Direct adaptive control for a class of mimo nonlinear systems using neural networks," *IEEE Transactions on Automatic Control*, vol. 49, no. 11, pp. 2001–2006, 2004.

[62] T. Hayakawa, M. M. Haddad, N. Hovakimyan, and V. Chellaboina, "Neural network adaptive control for nonlinear nonnegative dynamical systems," *IEEE Transactions on Neural Networks*, vol. 16, no. 2, pp. 399–413, 2008.

[63] T. Zhang, S. S. Ge, and C. C. Hang, "Adaptive neural network control for strict-feedback nonlinear systems using backstepping design," *Automatica*, vol. 36, no. 12, pp. 1835–1846, 2000.

[64] S. Ge, J. Zhang, and T. H. Lee, "Adaptive neural network control for a class of mimo nonlinear systems with disturbances in discrete-time,"

IEEE Transactions on Systems, Man, and Cybernetics, Part B: Cybernetics, vol. 34, no. 4, pp. 1630–1645, 2004.

[65] S. S. Ge, C. C. Hang, T. H. Lee, and T. Zhang, *Stable Adaptive Neural Network Control*.   Norwell MA: Kluwer,, 2000.

[66] S. Ge and K. Tee, "Approximation-based control of nonlinear mimo time-delay systems," *Automatica*, vol. 43, no. 1, pp. 31 – 43, 2007.

[67] J. Zhang, S. Ge, and T. H. Lee, "Output feedback control of a class of discrete mimo nonlinear systems with triangular form inputs," *IEEE Transactions on Neural Networks*, vol. 16, no. 6, pp. 1491 – 503, 2005.

[68] R. Yuan, J. Yi, W. Yu, and G. Fan, "Adaptive controller design for uncertain nonlinear systems with input magnitude and rate limitations," in *Proceedings of American Control Conference*, June 2011, pp. 3536–3541.

[69] M. Chen, S. S. Ge, and B. Voon Ee How, "Robust adaptive neural network control for a class of uncertain mimo nonlinear systems with input nonlinearities," *IEEE Transactions on Neural Networks*, vol. 21, no. 5, pp. 796–812, 2010.

[70] F. L. Lewis, S. Jagannathan, and A. Yesildirek, *The zebrafish book: guide for the laboratory use of zebrafish (Danio rerio)*.   New York: Taylor & Fracis, 1999.

[71] Y.-S. Zhong, "Globally stable adaptive system design for minimum phase siso plants with input saturation," *Automatica*, vol. 41, no. 9, pp. 1539 – 1547, 2005.

[72] L. Sonneveldt, Q. P. Chu, and J. A. Mulder, "Nonlinear Flight Control Design Using Constrained Adaptive Backstepping," *Journal of Guidance, Control, and Dynamics*, vol. 30, no. 2, pp. 322–336, 2007.

[73] W. Gao and R. R. Selmic, "Neural network control of a class of nonlinear systems with actuator saturation," *IEEE Transactions on Neural Networks*, vol. 17, no. 1, pp. 147–156, 2006.

[74] Q. Hu, G. Ma, and L. Xie, "Robust and adaptive variable structure output feedback control of uncertain systems with input nonlinearity," *Automatica*, vol. 44, no. 2, pp. 552 – 559, 2008.

[75] X. Tang, G. Tao, and S. M. Joshi, "Adaptive actuator failure compensation for nonlinear mimo systems with an aircraft control application," *Automatica*, vol. 43, no. 11, pp. 1869–1883, 2007.

[76] M. Polycarpou, J. Farrell, and M. Sharma, "On-line approximation control of uncertain nonlinear systems: issues with control input saturation," in *Proceedings of the 2003 American Control Conference*, vol. 1, 2003, pp. 543–548.

[77] J. Farrell, M. Polycarpou, and M. Sharma, "Adaptive backstepping with magnitude, rate, and bandwidth constraints: aircraft longitude control," in *Proceedings of American Control Conference*, vol. 5, 2003, pp. 3898–3904.

[78] ——, "On-line approximation based control of uncertain nonlinear systems with magnitude, rate and bandwidth constraints on the states and actuators," in *Proceedings of American Control Conference*, vol. 3, June 2004, pp. 2557–2562.

[79] M. Chen, S. S. Ge, and B. Ren, "Adaptive tracking control of uncertain mimo nonlinear systems with input constraints," *Automatica*, vol. 47, no. 3, pp. 452 – 465, 2011.

[80] Z. Lu, C. Y. P. Chen, H. Luo, J. Nam, R. Ge, and W. Lin, "Models of max-

imum stress and strain of zebrafish embryos under indentation," *Journal of Biomechanics*, vol. 42, no. 5, pp. 620 – 625, 2009.

[81] D. Roylance, "Engineering viscoelasticity," http://web.mit.edu/course /3/3.11/www/modules/visco.pdf, 2001.

[82] B. Yao and M. Tomizuka, "Adaptive robust motion and force tracking control of robot manipulators in contact with stiff surfaces," *ASME Journal of Dynamic Systems, Measurement, and Control*, vol. 120, pp. 232–240, 1998.

[83] ——, "Smooth robust adaptive sliding mode control of manipulators with guaranteed transient performance," *ASME Journal of Dynamic Systems, Measurement, and Control*, vol. 118, pp. 764–775, 1998.

[84] ——, "Adaptive robust control of siso nonlinear systems in a semi-strict feedback form," *Automatica*, vol. 33, no. 5, pp. 893–900, 1997.

[85] J. Slotine and W. Li, *Applied Nonlinear Control*. Englewood Cliffs, New Jersey: Prentice Hall, 1991.

[86] Z. Cai, M. S. De Queiroz, and D. M. Dawson, "A sufficiently smooth projection operator," *IEEE Transactions on Automatic Control*, vol. 51, no. 1, pp. 135–139, 2006.

Appendix A

In this appendix, the specific forms of the matrix of the equations of motion in Equation (2.4) are presented.

The element of the equilibrium matrix $A(q)$, A_{ij} is:

$$A_{ij} = \frac{\partial l_j}{\partial q_j} \qquad i = 1, \ldots 24, \; j = 1, \ldots 33 \tag{A.1}$$

where l_j is the length of the jth working tendon.

The element of the tensions matrix $T(q)$, T_j is:

$$T_j = k_j(l_j - l_{0j}) \qquad j = 1, \ldots 33 \tag{A.2}$$

where k_j is the stiffness of the jth working tendon; l_{0j} is the initial length of the jth working tendon.

The expression of damping matrix $C(q)$ is:

$$C(q) = \sum_{j=1}^{33} c_j C_j(q) \tag{A.3}$$

where c_j is the damping ratio of the jth working tendon and $C_j(q)$ is defined by the geometric properties of the tensegrity structure.

The expression of the disturbance matrix $H(q)$ is:

$$H(q) = \text{diag}\{H_1, \ldots, H_7\} \qquad (A.4)$$

where

$$H_{i=1,2,3} = \begin{bmatrix} \dfrac{\cos\alpha_{i1}\cos\delta_{i1}}{2} & \dfrac{\sin\alpha_{i1}\cos\delta_{i1}}{2} & \sin\alpha_{i1}\cos\delta_{i1} \\ -\dfrac{\sin\alpha_{11}\sin\delta_{i1}}{2} & \dfrac{\cos\alpha_{i1}\sin\delta_{i1}}{2} & 0 \end{bmatrix} \qquad (A.5)$$

$$H_{i=4,5,6,7} = \text{diag}\{1,1,1,0,0\} \qquad (A.6)$$

Appendix B

In this appendix the general forms of A_f, T_f and C_f of the homogeneous six-strut cellular tensegrity structure with constant stiffness k and damping ratio c, are presented.

A_f is the equilibrium matrix with respect to q_f whose entries are:

$$A_{fij} = \frac{\partial l_j}{\partial q_{fi}} \quad (i = 1, ...24, \; j = 1, ...33) \tag{B.1}$$

where l_j is the length of jth tendon.

T_f indicates the tensions in the tendons whose entries are:

$$T_{fj} = k(\frac{l_j}{l_{j0}} - 1) \tag{B.2}$$

where l_{j0} is the initial length of jth tendon.

C_f is the damping matrix with respect to q_f and it is given as:

$$C_f(q_f) = \sum_{j=1}^{33} c \cdot C_{fj}(q_f) \tag{B.3}$$

where C_{fj} are matrices which depend on the geometric properties of the structure.

Appendix C

In this appendix, the initial state of q_f are presented.

q_{1r} and q_{2r} are given as

$$q_{1r} = [\, X_{10}\ Y_{10}\ Z_{10}\,]^T \tag{C.1}$$

$$q_{2r} = [\, \delta\ \alpha\ \delta\ \alpha + 240\ \delta\ \alpha + 120\ \delta\ \alpha\ X_{20}\ Y_{20}\ Z_{20}\ \delta \tag{C.2}$$

$$\alpha + 240\ X_{30}\ Y_{30}\ Z_{30}\ \delta\ \alpha + 120\ X_0\ Y_0\ Z_0\,]^T \tag{C.3}$$

where $\alpha = 60°$, $\delta = 54°$, $L = 10$ and

$$X_{10} = L\frac{\sqrt{6}}{8} - (L - r)\sin\delta\cos\alpha,$$

$$Y_{10} = L\frac{\sqrt{2}}{8} - (L - r)\sin\delta\sin\alpha,$$

$$X_{20} = \frac{L}{4}\sin\delta\cos\alpha - L\frac{\sqrt{3}}{4}\sin\delta\sin\alpha,$$

$$Y_{20} = -L\frac{\sqrt{2}}{4} + \frac{L}{4}\sin\delta\sin\alpha + L\frac{\sqrt{3}}{4}\sin\delta\cos\alpha,$$

$$X_{30} = -L\frac{\sqrt{6}}{8} + \frac{L}{4}\sin\delta\cos\alpha + L\frac{\sqrt{3}}{4}\sin\delta\sin\alpha,$$

$$Y_{30} = L\frac{\sqrt{2}}{8} + \frac{L}{4}\sin\delta\sin\alpha - L\frac{\sqrt{3}}{4}\sin\delta\cos\alpha,$$

$$Z_{10} = (L + r)\cos\delta - h,$$

$$Z_{20} = Z_{30} = \frac{3}{2}L\cos\delta - h,$$

$$X_0 = Y_0 = 0, \quad Z_0 = L\cos\delta - \frac{h}{2},$$

$$h = \frac{L}{\cos\delta}\left[\cos 2\delta + \frac{\sqrt{2}}{2}\sin\delta\cos(\alpha - 30°)\right].$$

Appendix D

In this appendix the general forms of A_f, T_f and C_f of the heterogeneous six-strut cellular tensegrity structure with time-varying stiffness and damping ratio are presented.

A_f is the equilibrium matrix with respect to q_f whose entries are:

$$A_{fij} = \frac{\partial l_j}{\partial q_{fi}} \quad (i = 1, ...24, \ j = 1, ...33) \tag{D.1}$$

where l_j is the length of jth tendon.

T_f indicates the tensions in the tendons whose entries are:

$$T_{fj} = k_j(t) \cdot (\frac{l_j}{l_{j0}} - 1) \tag{D.2}$$

where, l_{j0} is the initial length of jth tendon.

C_f is the damping matrix with respect to q_f and it is given as:

$$C_f(q_f) = \sum_{j=1}^{33} c(t) \cdot C_{fj}(q_f) \tag{D.3}$$

where C_{fj} are matrices which depend on the geometric properties of the structure.